東海大学大学院平成 28 年度博士論文

Study on Effect of Substrate Biasing on Crystalline Growth and Insulator-Metal Transition Properties of Vanadium Dioxide Films on Sapphire Substrates

（基板バイアス印加法によるサファイア基板上への二酸化バナジウム薄膜の結晶成長と絶縁体−金属転移特性に関する研究）

指導教員　　沖村邦雄　教授

東海大学大学院　総合理工学研究科
総合理工学専攻

NURUL HANIS BINTI AZHAN

Abstract

Vanadium dioxide (VO_2) thin films with an insulator-metal transition (IMT) near room temperature of 68ºC have been researched as candidate for technological applications such as electronic switching devices, storage devices, and temperature sensing devices. However, from a practical point of view, transition temperature (T_t) of 68ºC is still too high. Metal doping and epitaxial mismatch stress control have been reported to be effective in lowering the T_t. However, considering these methods, where significant degradation in the transition properties and limit in film thickness were observed, new method of controlling the T_t is needed. In this work, rf substrate biasing was studied as a method to control in-plane *a*-axis of monoclinic phase (a_M-axis) of the VO_2 thin films on Al_2O_3 (001) substrates, thus control the T_t of the VO_2 thin films.

Rf magnetron sputtering apparatus equipped with rf substrate biasing set-up was utilized for deposition. As substrate biasing was applied through a blocking capacitor that installed in the matching circuit, negative dc self-bias voltage ($-V_{dc}$) was established at the substrate and was introduced as a method to increase the ion irradiation energy during the deposition. The deposition was performed by varying the substrate biasing power from 0 to 40 W. By maintaining all other deposition conditions including O_2 flow rate constant, comprehensive studies on the rf substrate biasing effect on the VO_2 films were performed.

Rf substrate biasing was observed to succeed in modifying the T_t towards lower temperature, while maintaining of almost two-order of magnitude transition in resistance changes, and also the hysteresis loops, indicating the intrinsic IMT properties of VO_2 films. Consequently, a significant improvement on the TCR value was achieved, where high TCR value of about -3.5 %ºC^{-1} was obtained in the film deposited at a biasing power of 30 and 40 W. In respect to that modification of the T_t, significant in-plane tensile and compressive stress was observed, as the lengthening and shortening of the in-plane a_M-axis length and V–V atoms distance in the VO_2 films depending on the ion irradiation energy of 140 eV (10 W), and 200, 230, 300 eV (20, 30, and 40 W). These observations proposed that the T_t modifications in VO_2 films due to the high energy ion irradiation during the sputtering are reasonably possible. Also, as the VO_2 films were deposited by high-energy ion irradiation, the introduction of oxygen vacancies is undeniable. Cooperation between compression of the a_M-axis and high oxygen vacancies concentrations revealed to be responsible for introducing the T_t modifications in films deposited larger than 30 W (> 230 eV).

Systematic control of the T_t with large T_t shift is achieved in the present work of substrate bias sputtering, where no changes in the deposition conditions needed are proposed to be advantageous for widening the applicability of the VO_2 films. Also, the growth of the μm-sized crystalline grains of VO_2 films on Al_2O_3 (001) substrates under particular substrate biasing conditions is expected to improve the transition properties and open new vistas of the VO_2 films.

Table of Contents

List of Figures

List of Tables

Chapter 1

Forward

Chapter 1 Forward

1.1 Introduction

Transition metal oxides (TMOs) has been claims to be one of the most interesting classes of solids, exhibiting varieties of properties, structures, and applications. TMOs possess unusual and useful electronic, optical and magnetic properties. Their properties are determined by their unique nature of outer *d*-electrons. Vanadium dioxide (VO_2) with a single electron in 3*d*-orbitals ($3d^1$) is introduced as a strongly correlated TMOs that exhibits an insulator-metal transition (IMT) and is accompanied by a structural phase transition (SPT) from a low-temperature monoclinic phase to a high-temperature rutile-tetragonal phase at near to room temperature approximately of 68°C.

For more than half centuries since the first observation of the transition in VO_2, continuous works considering its potential for various applications have been carried out. Considering its transition that could also be triggered by applying current and voltage, VO_2 is studied for applications of switching and memory devices.[1–3] Besides, significant resistance changes with the increasing in temperature have pointed VO_2 to be one of the most potential infrared radiation detecting materials for microbolometer sensors.[4–6] Recently, VO_2 with excellent thermochromic properties is also proposed for new generation smart windows.[7,8] In addition, VO_2 has also been studied for applications of memristors.[2,9,10] Memristors or resistors with memory belong to a general class of memory devices, named memristive systems, where materials with switchable and retainable resistance like VO_2 are the main key attributes for this application. However, despite the promising properties of high magnitude changes in electrical and optical characteristics, VO_2 poses challenges not to only considering its fundamental physics but also involving its fabrication issues. As one could realize, those proposed applications utilize the VO_2's main feature of the transition across the temperature; considering this matter, the critical temperature so-called transition temperature (T_t) is an important issue that concerned.

For years, a number of works have been devoted to control the transition temperature (T_t). Impurity doping with elements such as molybdenum (Mo), tungsten (W), and niobium (Nb) are acknowledged to be a successful method to control the T_t, significantly.[11–15] It has been reported that doping VO_2 with either higher or lower state cations such as Nb^{5+} or Al^{2+}, the T_t can be modified towards either lower or higher temperature, correspondingly. However, this method is undesirable for VO_2 because of the simultaneous degradation in the transition properties. Alternatively, modification of the T_t to almost room temperature with sharp transition properties have been demonstrated by controlling stress along *c*-axis of the high-temperature rutile-

tetragonal phase (c_R-axis), by growing the VO_2 films on TiO_2 (001) substrates. Unfortunately, this T_t modification only works for films thinner than its critical thickness.[16–19] Regardless of the film thickness limitation, this work suggesting that the T_t of the VO_2 thin film is closely related to the c_R-axis and by restraining the stress along the c_R-axis, modifications of the T_t is convincingly possible.

In this chapter, an overview of VO_2, including crystalline structure, electronic behavior, and, fabrication techniques will be reviewed. A brief outline regarding works on the modifications of the T_t in VO_2 thin films will be given. Later, problem statements and the objective of the present work will firstly be introduced. Finally, a roadmap for the rest of the dissertation will be proposed.

1.2 Vanadium Dioxide, VO_2: A Review

Vanadium dioxide (VO_2) is well known to exhibit insulator-metal transition (IMT), accompanied by a structural phase transition (SPT) from a low-temperature monoclinic structure to a high-temperature rutile-tetragonal structure at a temperature of around 68°C. A general overview of VO_2 and vanadium oxides (VO_x) system will be given in section 1.2.1. Later, crystalline structures and lattice parameters of VO_2 will be delivered in section 1.2.2. Details on its band structures will be given in section 1.2.3. Later, a brief review of the synthesis processes commonly employed for VO_2 will be delivered in section 1.2.4.

1.2.1 System of Vanadium Oxides

Transition metal oxides (TMOs) are studied for their unique and useful electronic, chemical, and optical properties. One of the most potential TMOs studied for various applications is vanadium oxides (VO_x). VO_x has attracted much attention due to their occurrence of IMT at various temperatures. Between them, VO_2 is the most actively studied phase due to the occurrence of the IMT near to room temperature. Kosuge proposed the systematic phase diagram of this VO_x system in 1967.[20] Figure 1-1 shows the phase diagram of the V_2O_3-V_2O_5 system, where *x*- and *y*-axes correspond to a number of oxygen (x) in VO_x and growth temperature, respectively. From this diagram, one can expect that the stoichiometry in VO_2 could easily deviate even with slight changes in the amount of oxygen.

As an oxidation of vanadium occurs in a relatively small amount of oxygen, vanadium forms Magnéli phases (V_nO_{2n-1}), such as V_2O_3 and V_4O_7. Magnéli phases known to behave as a metal at room temperature. Among them, V_2O_3 is reported to be the most stable phase, where the IMT occurs at a low temperature of 160 K (-113ºC).[21,22] In contrast, Wadsley phases (V_nO_{2n+1}), such as V_6O_{13} and V_2O_5 grow as the oxidation occurs with a large amount of oxygen. V_6O_{13} is a mixed-valence oxide experiencing a semiconductor-semiconductor transition at a low temperature of 150 K (-123ºC).[23] V_2O_5 is a semiconductor at room temperature with a wide band gap of 2 eV and reported to undergo a semiconductor-metal phase transition at high temperature near 530 K (257ºC).[24] From the phase diagram, one can observe that the growth of V_nO_{2n-1} and VO_2 are stable until the high temperature of around 1200ºC (at pressure of 1 atm). In different, the growth of V_nO_{2n+1} is observed only to be stable at temperature lower than 650ºC. As the temperature reached around 650ºC, liquid phase exists with another solid phase; V_6O_{13} + liquid and VO_2 + liquid. The existence of liquid phase in VO_X system is in a good agreement to the low melting point of V_6O_{13} and V_2O_5 of 667 and 670ºC, respectively.[25]

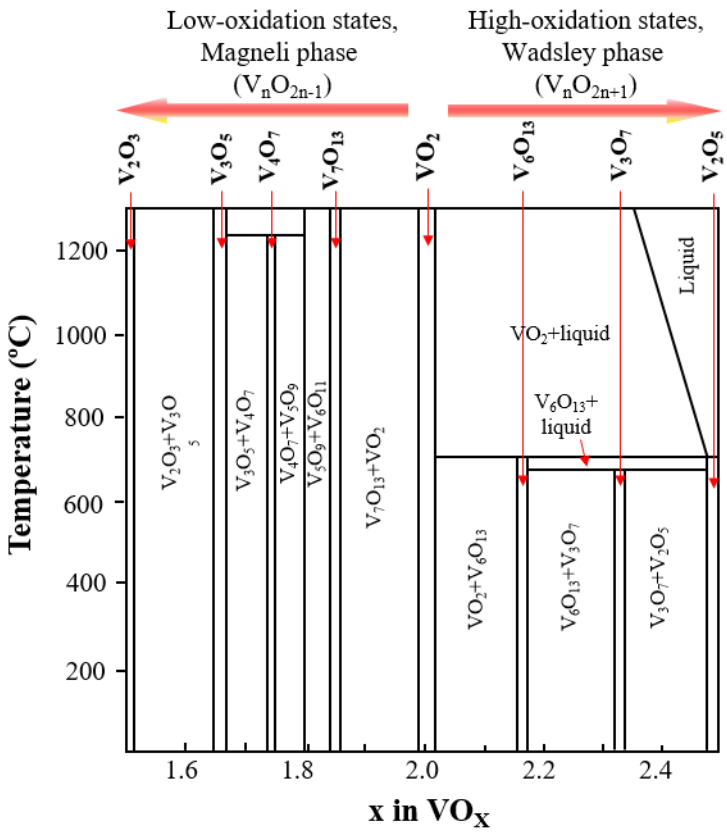

Fig. 1-1 Phase diagram of V_2O_3-V_2O_5.[20,26]

The changes of stoichiometry in vanadium oxides occur as a single valence of the oxidation states from V^{2+} to V^{5+}, in the form of VO (V^{2+}), V_2O_3 (V^{3+}), VO_2 (V^{4+}), and V_2O_5 (V^{5+}). However, mixed valence oxides of Wadsley and Magnéli phases that contain two oxidation states, such as V_6O_{13} with V^{4+} and V^{5+} and V_4O_7 with V^{3+} and V^{4+} were also observed in the phase diagram, caused complicated correlation oxidation states of the VO_X system. Theoretically, VO_2 grows as a single valence state of V^{4+}. However, due to the formation of vacancy (oxygen or vanadium) defects, the growth of mixed-valence VO_2 (consists of V^{5+}, V^{4+}, V^{3+}, and V^{2+}) was frequently reported.[27–29] As the number of vacancies exceeds a certain value, the vacancies tend to correlate and form crystallographic shear planes, and subsequently eliminated by the reorganization of V–O coordination, which then finally resulting in the growth of related stoichiometries oxides, V_nO_{2n-1} or V_nO_{2n+1}.[30]

1.2.2 Crystalline Structures of VO_2

Andersson reported on the details of the VO_2 structural properties for both structures at low- and high-temperature, including the relations between them in 1956.[31] Refinement of these structures was later proposed by Longo and Kierkegaard in 1970.[32] Their report gave a substantial improvement in the atomic parameters but did not change the general picture of the structures suggested before.

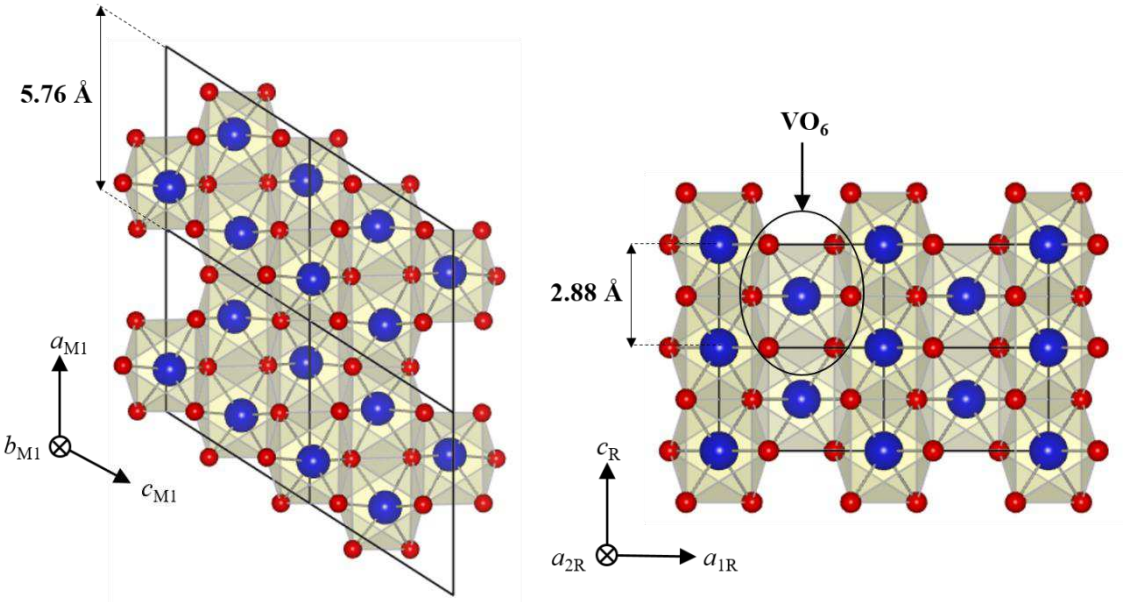

Fig. 1-2 2D images of VO_2 (a) low-temperature M1 phase and (b) high-temperature R phase.

Figure 1-2 shows the two-dimensional images of the (a) low-temperature monoclinic (M1) phase and (b) high-temperature rutile-tetragonal (R) phase. As mentioned before, accompanying the IMT, as temperature increases to the vicinity of 68°C, SPT occurs from the low-symmetry monoclinic phase (M1, space group $P2_1/c$ (No. 14)) to the high-symmetry rutile-tetragonal phase (R, space group $P4_2/mnm$). Atomic positions of the M1 structure were given by one V position and two O positions that all have a 4*e* letter in Wyckoff positions. Unique axis is *b*-axis, coordinates are given as V (0.242, 0.975, 0.025), O1 (0.1, 0.21, 0.2), and O2 (0.39, 0.69, 0.29), respectively. As for the R phase, the atomic positions are given by V (0, 0, 0) and O (0.305, 0.305, 0) positions with Wyckoff positions of 2*a* and 4*f*.

Apparently, as the temperature increases, an arrangement of the vanadium (V) atoms along the *a*-axis of the distorted M1 phase (a_M-axis) forming a pair (V–V atoms), thus results in the occurrence of SPT to rather stable R phase. In the high-temperature R phase, V atoms occupy bcc positions with larger oxygen (O) atoms reside in octahedral positions around the V atoms to form

a hexagonal close-packed lattice usually known as MO_6 structure (VO_6, shown in Fig. 1-2 (b)). In the R phase, V atoms are located at an equal distance along the *c*-axis (c_R-axis). Based on the context of metal to insulator transition from high- to low-temperature, R lattice distorts by shift and displacement of the V atoms at the corners along the c_R-axis alternately to opposite directions. Thus, two different distances between vanadium atoms of 2.62 Å and 3.16 Å instead of 2.85 Å (c_R-axis) are formed, which lead to a doubling of the cell along the c_R-axis (correspond to a_M-axis). Accordingly, as the SPT occurs, the unit-cell size doubled in VO_2 (M1) phase compared to that of R phase. The relation between the lattice of VO_2 (M1) and VO_2 (R) phases are shown as below:

$$a_{M1} = 2c_R, \quad b_{M1} = a_R, \quad c_{M1} = a_R - c_R \quad \dots (1\text{-}1)$$

In the low-temperature region, besides the M1 phase, VO_2 is known to exist in some other phases, including M2 phase, A phase, and B phase. It was frequently reported that during the SPT from insulating M1 to the metallic R phase, another metastable monoclinic of M2 phase appeared, in which half of the V atoms paired but did not twist, while the other half twist, but remain equidistant along the c_R-axis, resulting in the zigzag chain.[33–35] The growth of M2 phase is proposed to be induced by either stress or doping. By manipulating those two factors, VO_2 (M2) is reported to be stabilized at room temperature.[36,37] Besides, active research on the metastable VO_2 (B) has been carried out, in which the VO_2 (B)'s characteristic layered structure is attracting much attention for a new potential cathode material in secondary lithium ion batteries.[38,39] In the other hand, compared to others, the study on the VO_2 (A) falls a step behind due to its difficulties in the synthesis that has lead to ambiguous characteristics of this phase.[40,41] Lattice parameters of the high- and low-temperature VO_2 crystals are listed as in Table 1-1.

Table 1-1 Lattice parameters of high-temperature VO_2 (R) and low-temperature VO_2 (M1), (M2), (A), and (B).

Phase	Space group	Lattice type	*a*-axis length (Å)	*b*-axis length (Å)	*c*-axis length (Å)	β (°)
R	$P4_2/mnm$	rutile	4.555	-	2.856	-
M1	$P2_1/c$	monoclinic	5.753	4.526	5.383	122.6
M2	C2/m	monoclinic	9.066	5.797	4.525	91.88
A	P4/ncc	tetragonal	8.44	8.44	7.666	-
B	C2/m	monoclinic	12.042	3.689	6.431	106.96

1.2.3 Band Structures of VO_2

Vanadium, V (electron number 23) with an electronic configuration of $3d^3$ $4s^2$ has five electrons in the outer shell. In the formation of VO_2, vanadium's outer shell electrons filled up the oxygen's $2p$ orbit, resulting in the formation of the positive ion of V^{4+} and negative ion of O^{2-}. Band structure of VO_2 is discussed based on its characteristic V $3d$ orbitals of the V ions. According to the theory of point group, the V $3d$ orbitals are built by triple generated t_{2g} (x^2-y^2, yz, and xz) and double generated e_g ($3z^2$-r^2 and xy) at low- and high- energy states. This energy level is decided by the interaction with the neighboring oxygens (O $2p$) orbitals. The low energy states of t_{2g} further splits into a_{1g} (d_{II}) and e^{π}_g (π^*) with the weakly hybridized (by O $2p$ orbitals) d_{II} states lie in the lowest (in term of energy). The d_{II} states are directed along the c_R-axis, with a strong σ-bonding of the V–V atoms along this direction.

In the insulating M1 phase, the strong dimerization and tilting of the V–V pairs along a_M-axis are resulting in the splitting of the d_{II} states to two states of bonding (d_{II}) and anti-bonding (d_{II}^*). This separation results in the opening of a gap in the band structure at low temperature. Accordingly, displacement of the V atoms also resulting in significant raising of the energy level of the π^* above the Fermi level (E_F). These two characteristics behavior of the t_{2g} orbitals give the band structure of the insulating M1 phase to be as shown in Fig. 1-3 (a).

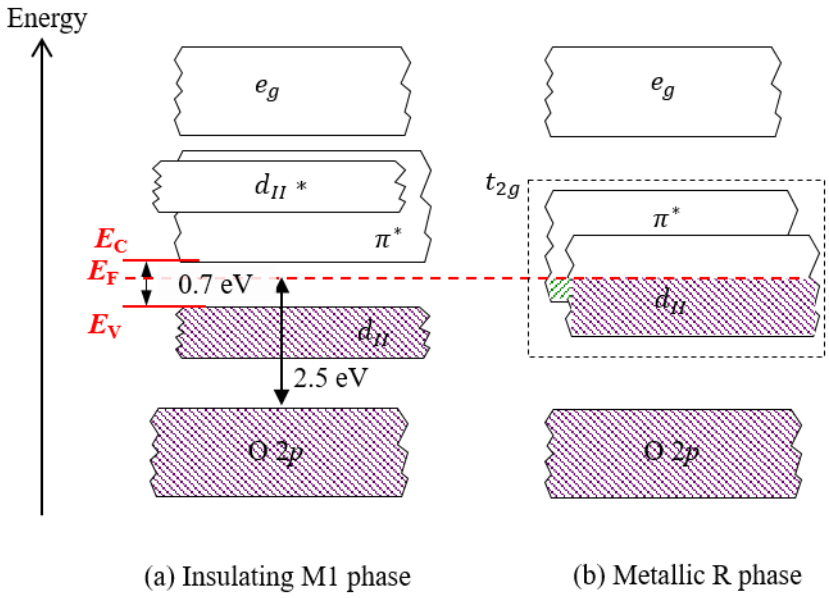

Fig. 1-3 Band structures of low-temperature insulator and high-temperature metallic phases.

Figure 1-3 shows the V 3*d* – O 2*p* band splitting of VO_2 (a) for insulating M1 phase and (b) for metallic R phase. From Fig. 1-3 (a), at a low temperature, one can observe the narrow gap opening of around 0.7 eV with the E_F lies about 2.5 eV above the top of the O 2*p* band. This electronic band structure was explained in details by Goodenough in 1971.[42] He proposed that the transition in VO_2 occurs involving the unit cell doubling and the pairing of the V atoms. The single electron of $3d^1$ occupies the d_{II} bonding combination, thus resulting in a Peierls-like band gap. However, some other researchers, including Zylbersztejn and Mott,[43] Sommers and Doniach,[44] and Rice *et al.*[45] strongly suggested that the Coulomb repulsion plays a major role in opening the gap in M1 phase, agreeing on the physics of VO_2 that belong to the Mott-Hubbard interactions.

In 2002, Eyert performed electronic structure calculations based on density functional theory within the local density approximation (DFT-LDA) to support Goodenough's qualitative description regarding the molecular orbitals.[46] However, this calculation failed to reproduce the band gap opening of the insulator VO_2. Later in 2005, Biermann *et al.* reported on the consistent description of both metallic and insulator behavior of VO_2 by performing calculations by cluster dynamical mean field theory, with the conjunction of the density functional scheme (LDA+CDMFT).[47] They suggested that the transition in VO_2 belongs to both Mott-Hubbard interactions (band gap opening due to the electron-electron interaction) and Peierls transition (band gap opening due to the doubling of unit cell), where the formation of dynamical V–V singlet pairs due to strong Coulomb correlations is necessary to trigger the opening of a Peierls gap. These results are widely accepted by most of the researchers while discussing the transition properties in VO_2. However, a tug-war in determining the driving mechanism of this transition in VO_2 is still in continuity, as can be seen from recent works of Kim *et al.* and Chen *et al.*.[48,49]

1.2.4 Synthesis of VO_2

The transition of VO_2 was first reported in 1959 on the bulk single crystals, which were grown by H. J. Guggenheim using a hydrothermal method.[50] In the later work performed by Verleur *et al.* in 1968,[51] the VO_2 single crystals were also grown by H. J. Guggenheim, where nitrogen gas was passed over melted V_2O_5. V_2O_5 was slowly decomposed, thus later recrystallized as VO_2. Large transition near to four- or five-order magnitude changes in resistance was obtained on the bulk VO_2 single crystal. However, after several runs, bulk single crystals tend to crack and IMT properties are no longer obtainable.

Due to that matter, thin films VO_2 are much advantageous. As addition to that, for most applications, materials in the form of thin films are the most concerned. Several numbers of methods are utilized with the aim to synthesize a high-performance VO_2 thin films, including a reactive evaporation and a sol-gel method.[52,53] However, in order to obtain high-performance films with rather large area, following three methods have several advantages.

1) Chemical vapor deposition (CVD)

CVD is a widely used material processing technology for depositing high-quality and high-performance films. In the simplest incarnation, CVD involves flowing a precursor gas or gasses into a chamber that containing heated substrates. Chemical reactions that occur resulting in the deposition of a thin film on the substrate. In the case of VO_2, metal-organic chemical vapor deposition (MOCVD) was frequently performed, where metal-organic precursors, such as vanadium triethoxide oxide [VO $(OC_2H_5)_3$] and β-diketonate complex vanadyl acetylacetonate [$VO(acac)_2$] were often used.[54,55] Besides, organometallic chemical vapor deposition (OMCVD) could also be performed, where organometallic precursors, such as vanadyl tri (isobutoxide), $VO(O\text{-}i\text{-}Bu)_3$, is often used as a starting compound.[56]

2) Pulsed laser deposition (PLD)

PLD is one type of physical vapor deposition (PVD) technique that has been proved as an excellent method especially in depositing oxide thin films. In PLD, a high power pulsed laser beam will be focused on a target with the desired composition inside the vacuum chamber. Material vaporized from the target then deposited on substrates as thin films. Recent years, PLD became the most popular technique for VO_2 thin films and VO_2 nanoparticle fabrications, due to its ability in producing high-quality thinner films with film thickness of several tens nm.[57–59] PLD was utilized by Muraoka and Hiroi to deposit VO_2 films with a thickness of 10 to 15 nm on TiO_2 single crystalline substrates.[16] Stoichiometric VO_2 thin films on TiO_2 substrates enabled studies

on the epitaxial VO_2 films, where significant transition temperature modifications was observed.

3) Reactive sputtering deposition

Sputtering is a technique used to deposit thin films onto a substrate, where gaseous plasma is created, thus accelerating ions from the plasma to the target. The arriving ions erode the target *via* energy transfer. The ejected target ions are reacted with the inserted gas (e.g., oxygen) then deposited on substrates as thin films.

Reactive sputtering method was introduced to successfully fabricate high-quality VO_2 thin films.[60,61] Kusano *et al.* and Hoffman's group succeeded in fabricating VO_2 thin films with the transition of nearly four orders of magnitude in resistivity by dc magnetron reactive the sputtering and rf magnetron reactive the sputtering method.[62,63] Sputtering is also introduced as one of the most promising techniques for large-area uniform coatings with high packing density and strong adhesion films. Considering that, a lot of works on sputtering deposition have been conducted, including changing the metallic vanadium target to vanadium oxides targets, such as V_2O_3 and V_2O_5.[64] Also, in comparison to other physical vapor deposition, reactivating magnetron sputtering is rather much advantageous by considering the low-temperature deposition at around 300 to 400ºC.[62,65] Even so, considering the crucial oxygen composition in VO_2, fabrication of the stoichiometric VO_2 thin films are yet much more difficult.

1.3 Works on Modifying the Transition Temperature of VO_2

VO_2 has attracted much attention due to the electrical conductivity changes by three or four orders of magnitude during its IMT that occurs at little above the room temperature. As was introduced in section 1.1, utilizing VO_2's characteristics feature of IMT and SPT at temperature near towards room temperature, VO_2 is studied for various applications, including smart windows, bolometers, and memristors. Transition temperature (T_t) of 68ºC is considered to be low in comparison to other TMOs, yet in the application's point of view, this temperature is still somewhat high. Due to the factors, modifying the T_t of VO_2 became an important task for the VO_2-based applications realization. However, for years, this challenging task remains unsettled due to narrow growth conditions of VO_2 and its rather complicated physics features. In this section, overview on the T_t modifications of VO_2 will be given.

Morin reported his first observation of the insulator-metal transition (IMT) of bulk VO_2 in 1959.[50] He reported the reversible transition properties in electrical conductivity from 10^2 to 10^{-1} $\Omega^{-1}cm^{-1}$ with a transition temperature (T_t) in the vicinity of 69°C and 60°C for heating and cooling runs. Verleur *et al.* in 1968 reported IMT with four orders of magnitude change in resistivity (10^0 to 10^{-3} Ωcm) for VO_2 thin films deposited by reactive sputtering with a film thickness of 100 nm.[51] They also reported an abrupt change from an almost transparent state with the transmission of 0.7 to a low limiting transmission of 0.09 near the T_t of 68°C, suggesting the occurrence of the IMT in both electrical and optical properties of VO_2. This observation is an important discovery suggesting good transition behavior can also be obtained even in the VO_2 thin films.

Considering the excellent transition properties of VO_2, VO_2 films are frequently deposited on Al_2O_3 (001) substrates. However, in the case of VO_2 films on Al_2O_3 (001) substrates, in comparison to the T_t reported for the bulk, rather higher T_t was observed. [66,67] The shift of the T_t to rather higher temperature in VO_2 films on Al_2O_3 (001) substrates was explained considering the thermal expansion coefficient of VO_2 along the c_R-axis that is larger than that of Al_2O_3. The difference of the thermal expansion coefficient between VO_2 films and substrates is reported to be also responsible for modifying the T_t. Sakai *et al.* reported the effect of the thermal expansion coefficient difference on the T_t of VO_2 films on several substrates, including Al_2O_3 and Pt.[66]

In 2002, Muraoka and Hiroi demonstrated an extensive modification of T_t over a wide temperature range by controlling the epitaxial mismatch stress along the c_R-axis by growing VO_2 on TiO_2 (001) and (110) substrates. VO_2 films on TiO_2 (001) and (110) substrates, with compressed and elongated c_R-axis, were observed to have a modification on the T_t to rather low

and high temperatures, respectively.[16] However, this method which is triggered by the epitaxial mismatch stress only works for films thinner than a critical thickness. As the film thickness increases to be thicker than its critical thickness, T_t has been reported to return close to 68ºC (same as in the bulk). [17,68] Despite the film thickness issue, their work suggests that the T_t of the VO_2 thin film is closely related to the strain along the c_R-axis, where by restraining the stress along the c_R-axis, modification of the T_t would be convincingly possible. The same concept of utilizing the epitaxial stress later introduced for the T_t modification in VO_2 films on MgF_2 (001) substrates.[69]

The modification of the T_t was also been reported to be possible by utilizing the impurity doping method. By applying this method, stoichiometric VO_2 is predictably no longer exist due to the substitution of V ions with other metal's ions (M), thus introduce $V_{1-x}M_xO_2$. Impurity doping method is widely used due to its rather broader applicability, where both shifts towards lower and higher temperatures are possible by selecting the dopant materials and ratios. The T_t increases for lower state cations M doping of Cr^{3+},[33,70] Fe^{3+},[71] and Ti^{4+},[72,73] while decreases the T_t for higher state cations M doping of Nb^{5+},[70,74] Mo^{6+},[15,75] and W^{6+}.[76,77] By substituting V^{4+} ions with W^{6+} ions, the formations of W^{6+}–V^{3+} and V^{4+}–V^{3+} in W-doped VO_2 films were expected to stabilize the metallic behavior, thus lowering the T_t value.[78,79] In terms of a simple electron counting, substitution of a Nb^{5+} ion gives one electron, and a Mo^{6+} or a W^{6+} ion adds two electrons. In these works of substitution, excess electrons would be formed and responsible for reducing the T_t in VO_2. Regardless of this controllability of the T_t, nonstoichiometric VO_2 of doped-VO_2 films ($V_{1-x}M_xO_2$) is experiencing degradation in the magnitude of resistance change. Apart from that, disappearance of hysteresis during IMT in $V_{1-x}M_xO_2$ films is also a matter needs to be reconsidered.

From the above explanations, one can understand the importance of modifying the T_t of VO_2 films. Due to this matter, several significant modified T_t values reported in past years were summarized in Fig. 1-4. Figure 1-4 shows the T_t values observed in two most effective methods for the process of controlling the T_t, utilizing the epitaxial-stress controlling method [16,69] and doping method [15,80,81].

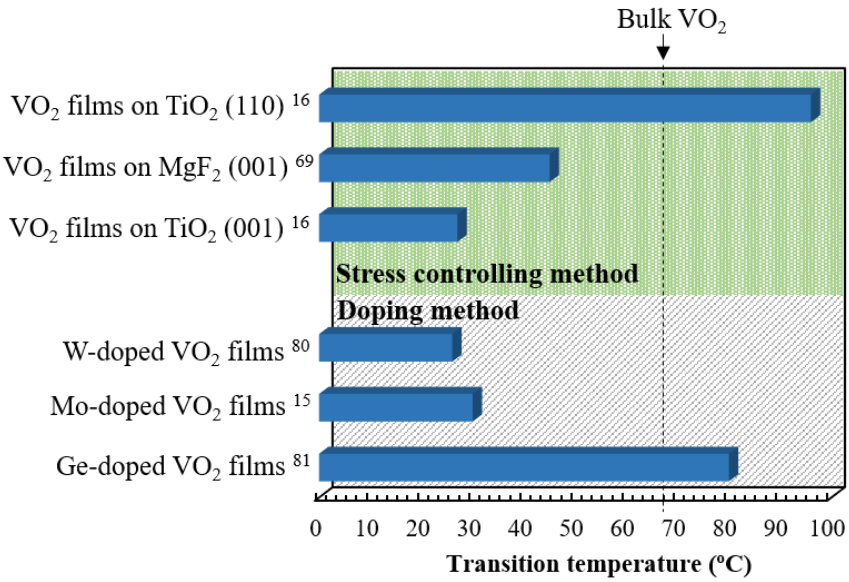

Fig. 1-4 Modified T_t values reported by stress-control and doping methods.

1.4 Problem Statement and Research Objective

VO_2 has attracted much attention due to the electrical conductivity changes by three or four orders of magnitude during its IMT. However, high transition temperature (T_t) of 68ºC has indeed laminating the further applications of this material. Although, several works towards lowering the T_t actively been performed for years, VO_2 thin films with large-magnitude of resistance changes with the T_t near room temperature still did not successfully fabricated. Furthermore, VO_2 characteristics that easily deviated with a slight change in deposition conditions make it more difficult for this material. Nonetheless, modifying the T_t is an important key to enlarge the application of this material.

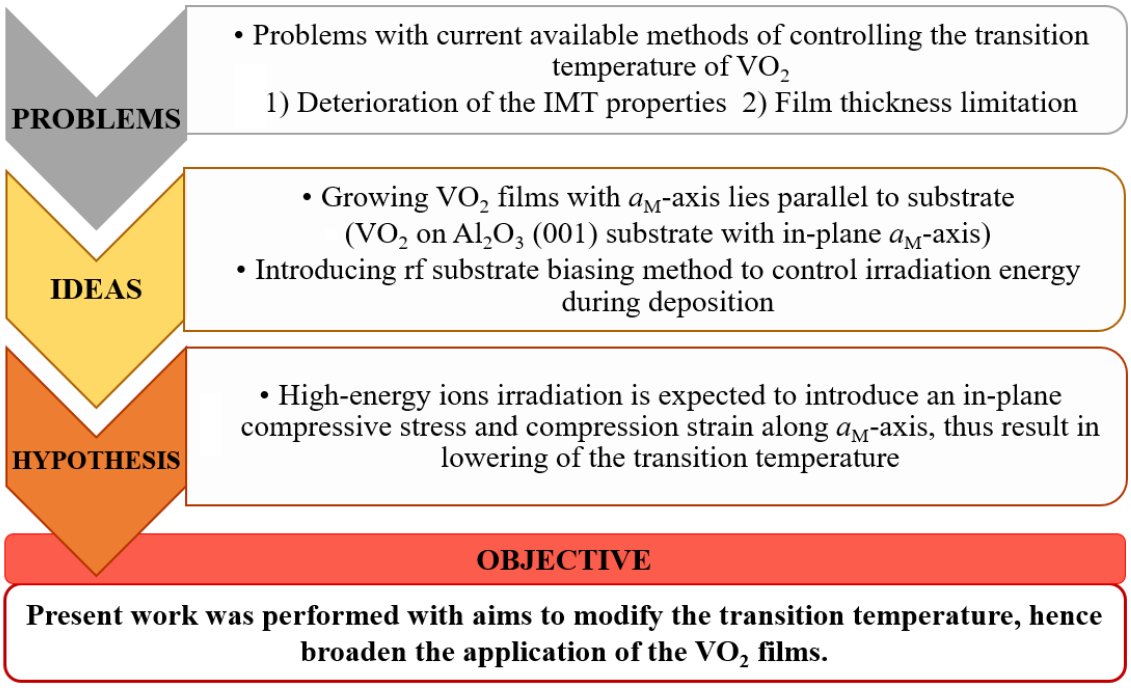

Fig. 1-5 Flowchart on problems, ideas, and hypothesis of the present work.

Considering the importance of controlling the T_t, present work is been carried out with the aim to modify the T_t, hence broaden the application of the VO_2 films. In the present work, a substrate biasing method is been introduced to study the possibility of lowering the T_t in VO_2 films, where T_t has been reported to be controlled significantly by controlling the stress along the c_R- (a_M) axis. In order to control the stress along the a_M-axis, which thus allowing the controlling of the T_t in VO_2 films, in this work, oriented VO_2 films grown on Al_2O_3 (001) substrates with the a_M-axis lies parallel to the substrate (in-plane axis) was introduced. Modification of the in-plane a_M-axis expected to be achieved by controlling ion irradiation during sputtering. Substrate biasing

was introduced as a method to control the energy of the ion incident to the substrate during the reactive sputtering deposition. In this work, the effect of the high-energy ion incident to the substrate during the deposition on the crystalline and transition properties of VO_2 thin films will be given. These ideas, hypothesis, and the main objective of the present work are summarized in Fig. 1-5.

1.5 Organization of Dissertation

This dissertation is divided into five chapters. As described in this chapter 1, the introduction of this work, including motivation and objective are briefly described. As a part of literature studies, a review on VO_2 was given in brief. The rest of this dissertation is organized as follows.

Chapter 2 This chapter deals with the growth of VO_2 films on Al_2O_3 (001) substrates by the rf substrate biasing deposition method. Reactive sputtering with the rf substrate biasing method would be introduce firstly, and significant increasing of ion irradiation energy during the biased sputtering will also be given. In this chapter, crystalline properties of VO_2 films deposited by the substrate biasing method are introduced. Significant modifications in the surface morphologies and film thickness as the results of the increasing energetic ion irradiation will be presented. Large modifications of IMT, SPT, and infrared (IR) transmittance properties of those films deposited by reactive sputtering with substrate biasing are presented. In significant with the T_t modifications, early Fermi level shifting in VO_2 films deposited under high-energy ion irradiation will be delivered. Finally, high value of the temperature coefficient of resistance (TCR) and activation energy (E_a) of films deposited at high-energy ion irradiation will be presented.

Chapter 3 In this chapter, mechanisms of the transition temperature (T_t) modifications in the VO_2 films triggered by the substrate biasing are discussed. The compression of the in-plane a_M-axis length was observed, in agreement with the strong in-plane compressive stress in the VO_2 films deposited at high energy ion irradiation will be introduced. Also, significant shortening of V–V atoms distance will later be illustrated. High-energy ion irradiation during substrate biasing sputtering is also expected to show oxygen vacancies. In this chapter, effects of oxygen vacancies on the IMT properties will also be delivered. From these results, mechanisms behind the modifications of the T_t will be discussed by considering the a_M-axis and oxygen vacancies, accordingly. Finally, consideration of the modifications of the T_t in films thicker than 100 nm will be given.

Chapter 4 This chapter discusses the characteristic growth phenomenon of VO_2 films with micro-sized grains at an adequate low substrate biasing power of around 10 W. The growth mechanism of the characteristic micro-sized VO_2 grains will be proposed. In this chapter, micro-sized domains structure, and their crystalline behavior are explained. Later, effects of the micro-sized grains growth on the IMT and SPT will be discussed.

Chapter 5 In this final chapter, concluding the remarks of this work, in which the rf substrate biasing method is introduced to control the IMT properties of VO_2 films, will be given. Finally, future works will be explained.

Chapter 2

Growth and Transition Properties of VO_2 films on Al_2O_3 (001) Substrates Deposited by Reactive Sputtering with Substrate Biasing

Chapter 2 Growth and Transition Properties of VO_2 films on Al_2O_3 (001) Substrates Deposited by Reactive Sputtering with Substrate Biasing

2.1 Introduction

Oriented VO_2 films grow on Al_2O_3 (001) substrates is widely used considering the stoichiometric VO_2 films growth with excellent IMT properties that can be obtained by owing to their lattice matching. The crystal growth orientation of VO_2 film on Al_2O_3 (001) substrate is illustrated in Fig. 2-1.

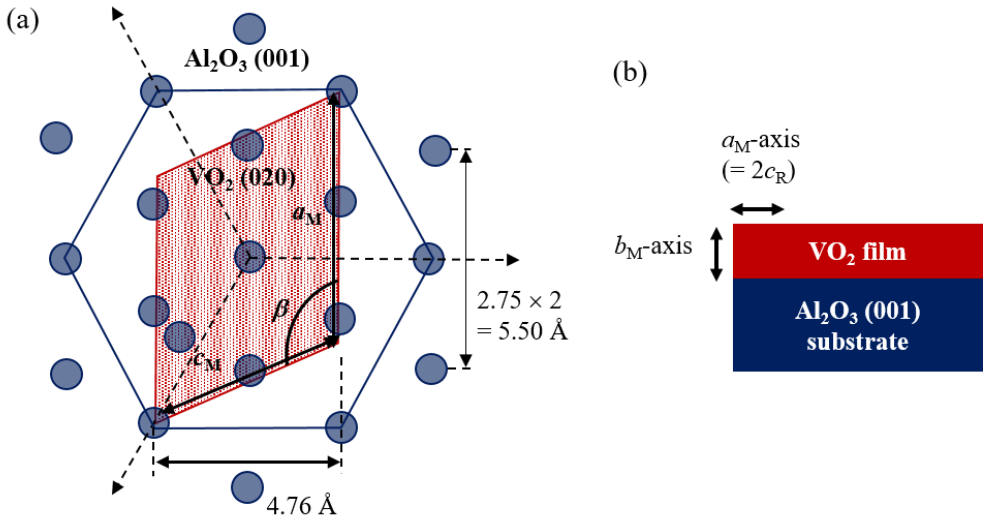

Fig. 2-1 (a) Schematic growth orientation and (b) two-dimensional diagram of VO_2 on Al_2O_3 (001).

Figure 2-1 (a) shows a schematic orientation of the monoclinic VO_2 (020) plane on the Al_2O_3 (001) plane, where interatomic distances of 5.50 Å and 4.76 Å on the Al_2O_3 (001) surface correspond to the a_M and c_M sin β (bulk value of 5.75 Å and 4.53 Å), respectively. The in-plane lattice mismatch calculation (in the unit of %) of this VO_2 films on Al_2O_3 (001) substrates for both a_M and c_M sinβ are shown as below.

Misfit along a_M, $M_{a_M} = \frac{d_s - d_f}{d_f} \times 100\ \% = \frac{5.75\ (\text{Å}) - 5.50\ (\text{Å})}{5.50\ (\text{Å})} \times 100\ \% = 4.5\ \%$

Misfit along c_M sinβ, $M_{c_M\, sin\beta} = \frac{d_s - d_f}{d_f} \times 100\ \% = \frac{4.53\ (\text{Å}) - 4.76\ (\text{Å})}{4.76\ (\text{Å})} \times 100\ \% = -4.8\ \%$

From the above calculations, one can understand that small lattice mismatch along a_M and $c_M \sin\beta$ of 4.5 % and -4.8%, which thus allow an epitaxial growth of VO_2 films on Al_2O_3 (001) substrates. For further discussion, the growth of VO_2 films on Al_2O_3 (001) substrates, a two-dimensional diagram as shown in Fig. 2-1 (b) is frequently taken for consideration.

In this work, main reason of selecting Al_2O_3 (001) as a substrate is the growth orientation of the in-plane a_M-axis (shown in Fig. 2-1 (b)), where the a_M-axis is the main feature to determine the VO_2 characteristics (i.e., T_t, V–V atoms distance), which is essential to this study. As introduced before, the large thermal expansion coefficient of VO_2 compared to that of Al_2O_3 is responsible for tensile stress (elongation) in the in-plane a_M-axis of VO_2 films, thus resulting in rather higher T_t.[67] Figure 2-2 shows the resistivity *vs.* temperature characteristics (ρ-T characteristics) of VO_2 film deposited on Al_2O_3 (001) substrate deposited by the rf magnetron reactive sputtering with a substrate temperature (T_S) of 400ºC and oxygen flow-rate of 1.0 sccm. A sharp transition in resistivity of 10^4 orders was observed, and as expected, rather higher T_t of 75ºC was observed.

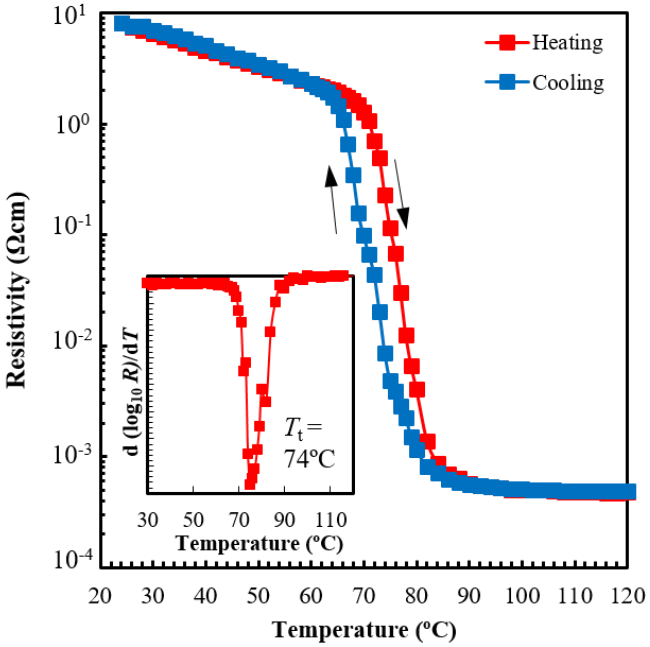

Fig. 2-2 ρ-T characteristic of VO_2 film on Al_2O_3 (001) substrate deposited by rf magnetron sputtering. Inset shows the d ($\log_{10}R$)/dT curve for the heating run.

Controlling the energy of ions incident to the substrate during deposition is reported to be effective in improving crystalline properties of the grown thin films.[82,83] Inductively coupled plasma (ICP) and substrate biasing methods are efficient in increasing and controlling the ion energy during sputtering deposition. During ICP, where SUS coil is inserted between the two

electrodes, ion energy increases as a plasma potential increases.[84] Md. Suruz Mian and K. Okimura studied the effect of the increasement of ion energy during the ICP sputtering and reported to succeed in depositing VO_2 films on metal electrodes at a relatively low temperature of 250ºC.[84,85] However, in the present work, the substrate biasing method is much more desirable considering the possibility of impurities co-operation during the ICP sputtering. To date, the substrate biasing is frequently applied in the deposition of metallic films, such as TiN and Mo.[86,87] In this work, high-frequency substrate biasing of 13.56 MHz was introduced as an insulating substrate is mainly utilized.

In this chapter, the rf magnetron reactive sputtering with the rf substrate biasing method and VO_2 films characterization methods will be introduced in sections 2.2.1 and 2.2.2. The growth of the VO_2 films on Al_2O_3 (001) substrates deposited by the reactive sputtering with substrate biasing will be firstly introduced in section 2.3.1. In this section, the effects of rf substrate biasing on the crystalline properties of VO_2 thin films will be delivered. Accordingly, the increasing of the ion irradiation during sputtering will modify the grain morphologies. Thus, morphologies of the sputtered VO_2 films, including the film thickness will be discussed in section 2.3.2. Changes in IMT and an early occurrence of SPT in VO_2 films deposited by rf substrate biasing will be given in the later sections of 2.3.3 and 2.3.4. In section 2.3.5, infrared (IR) transmittance properties will be given signifying the T_t modifications in optical properties of the sputtered VO_2 films. In corresponding to the occurrence of SPT, valence band shift in films deposited with the biasing power of 20 and 40 W, with improved crystalline properties and the lowest T_t will be presented in section 2.3.6. Significant increase in the values of the TCR and activation energy (E_a) will then be given in section 2.3.7. Finally, in section 2.4, the conclusions on the effects of substrate biasing on the growth and transition properties of VO_2 films will be delivered.

2.2 Experimental Methods

2.2.1 Rf Magnetron Reactive Sputtering with Rf Substrate Biasing

A metallic vanadium V target (Ø100 mm, purity of 99.9%) is placed in a vacuum chamber with an electrode spacing of 55 mm. A metallic vanadium V plate (50 mm × 50 mm × 0.2 mm, purity of 99.5 %) was placed on the heater to enable biasing on the substrate and to prevent impurities. Rf power with a frequency of 13.56 MHz was applied to both the target and the substrate, and was coupled *via* a pi-type matching circuit. This system provides power matching between the rf power source, cable, and the plasma to around 50 Ω (impedance of the power supply). In each circuit, a blocking capacitor was installed to block a direct current from the rf power sources, thus enabling the occurrence of negative self-bias voltage ($-V_{dc}$) at both the target and the substrate. Figure 2-3 presents a schematic diagram of the sputtering apparatus equipped with the rf substrate biasing set-up.

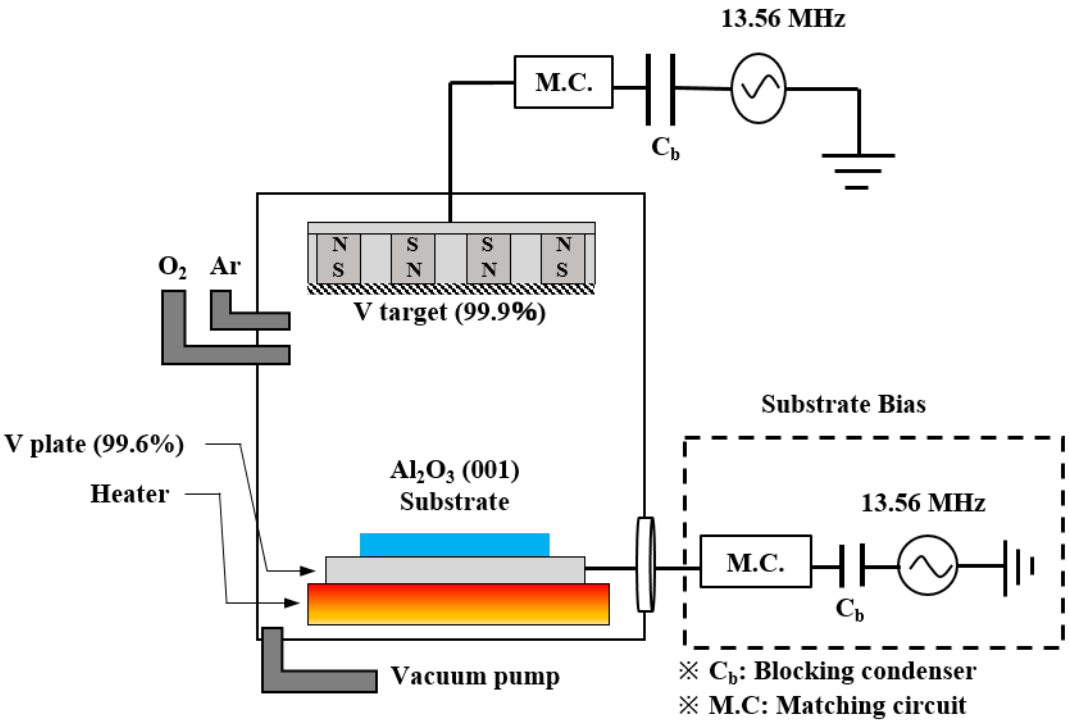

Fig. 2-3 Schematic diagram of rf magnetron sputtering with the rf substrate biasing.

As mentioned earlier, the rf substrate biasing power is known to be an efficient method for controlling the ion irradiation energy during sputtering. Considering the changes of the ion irradiation energy (E_{ion}), it is essential to analyze the ion energy distribution (IED) in the present work. However, it is difficult to measure the IED by using the conventional IED analysis

measurement, where an energy analyzer is installed at the center of the substrate. Due to this matter, in the present work, E_{ion} has been discussed by considering the bias voltage waveforms.

Figures 2-4 (a) and 2-4 (b) present the $-V_{dc}$ measurement set-up and the changes of the bias voltage waveforms in a function of time, measured by oscilloscope during the rf substrate biasing sputtering deposition. As shown in Fig. 2-4 (a), in order to allow the $-V_{dc}$ measurement to be performed, an electrical circuit with a series resistance of 100 kΩ and 1 MΩ was introduced. In Fig. 2-4 (b), the voltage signal for which the substrate was electrically grounded (bias of 0 W) is also included. As one can observe, the potential on the electrode (substrate) is modulated at the frequency of the rf substrate biasing power of 13.56 MHz. It is well known that the ion energy distribution function (IEDF) is bimodal with one peak at a low energy and another at a high energy. This variation is expected to be due to the ions transverse and transit times in the plasma sheath, respectively.[88] Accordingly, positive peak of the cycle (V_{p+}) and negative peak of the cycle (V_{p-}) in the bias voltage waveforms give information on the low- and high-energy peaks of the IEDF. The decreasing of the V_{p-} and with the increasing substrate biasing power in Fig. 2-4 (b) proposed significant acceleration of the E_{ion} during the reactive sputtering with substrate biasing.

From Fig. 2-4 (b), the average substrate voltage or self-bias voltage (V_{dc}) is negative in all cases, hence results in the ions acceleration toward the substrate. During deposition, a positive space charge layer known as plasma sheath is developed between the bulk plasma and the substrate due to the different thermal velocity between electrons and ions that is rather much heavier. When the gas pressure is low, ions pass through the plasma sheath without collision. Long mean free path results in the so-called collisionless plasma, where ions are accelerated over the full sheath, thus give a relation of the ion energy (E_{ion}) (in unit of eV) at the substrate during sputtering as

$$E_{ion} = e \cdot V_{sheath} = e \cdot (V_{plasma} - V_{sub}) \ldots (2\text{-}1)$$

where e is the electron charge, V_{sheath} is the voltage across the plasma sheath, V_{plasma} is the plasma potential, and V_{sub} is the substrate potential. V_{sub} is considered to take the value of the dc self-bias voltage (V_{dc}) and has a value of which the net flux of ions and electrons to the substrate is zero within one rf cycle. This consideration is possible, considering the ions only respond to the average dc bias voltage during the high-frequency power supplied of 13.56 MHz.

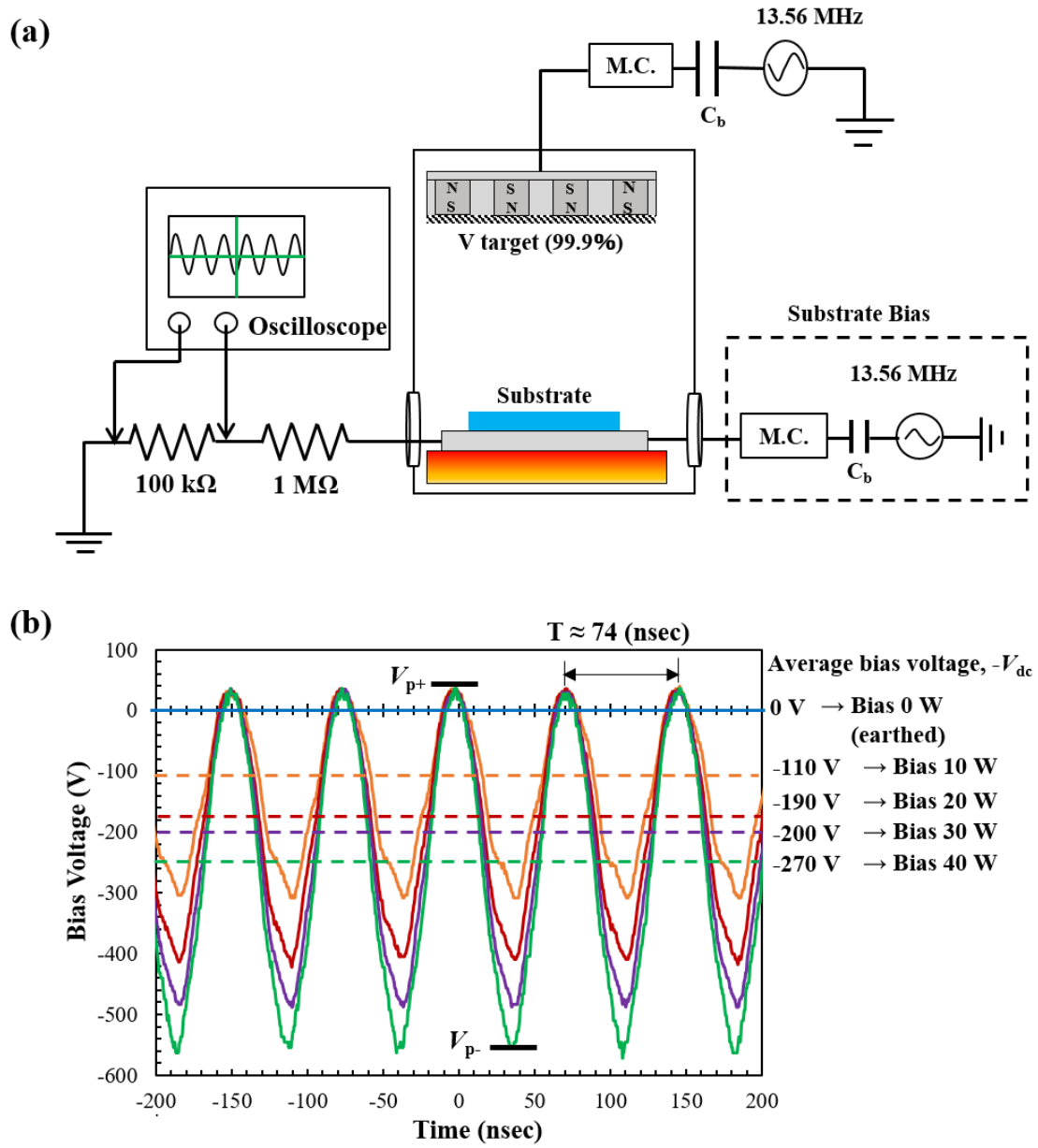

Fig. 2-4 (a) Dc self-bias voltage ($-V_{dc}$) measurement set-up. (b) Bias voltage waveforms in a function of time for the substrate biasing power of 0, 10, 20, 30, and 40 W.

Profijt *et al.* in their work on the substrate-biasing during plasma-assisted atomic layer deposition (ALD) revealed that the average ion energy measured from the IED measurement remains approximately equal to equation (2-1), indicating that the V_{plasma} remains constant despite the increasing of V_{sub} (hereafter known as V_{dc}) with the increasing of substrate biasing power.[89] In agreement with the reported results, in the present work, Langmuir probe measurement was carried out to measure the V_{plasma}, and an identical result was obtained, where no significant changes in the V_{plasma} were observed with the increasing substrate biasing power at around 30 V.

One should note that, Langmuir probe measurement was performed at distance of 20 mm from the substrate.

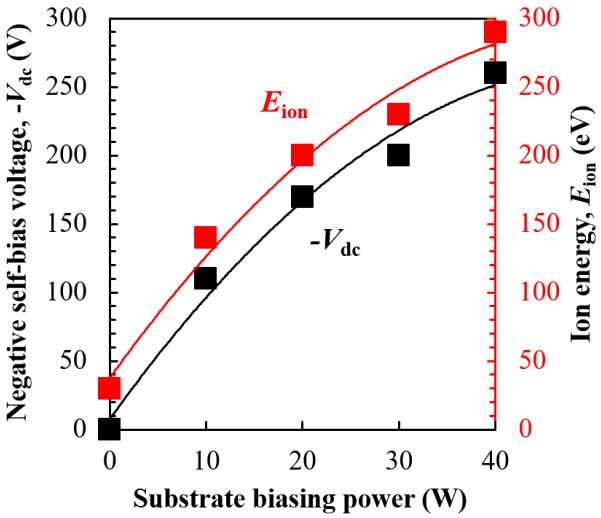

Fig. 2-5 The increasing of negative dc self-bias voltage (-V_{dc}) (in black) and ion energy (E_{ion}) (in red) with the increasing of substrate biasing power.

Figure 2-5 shows the increasing of the negative dc self-bias voltage (-V_{dc}) and ion energy (E_{ion}) with the increasing of substrate biasing power. From this result, one can understand that in this reactive sputtering with substrate biasing, the ion energy was increased by increasing the rf substrate biasing power. The -V_{dc} accelerates ions from the plasma to the substrate, thus enables the control of the ion irradiation during the deposition. As the substrate biasing power increased from 0 to 10, 20, 30, and 40 W, -V_{dc} increased from 0 to 110, 170, 200, and 270 V, thus increased the E_{ion} from 30 to around 140, 200, 230, and 300 eV, correspondingly.

These high values of -V_{dc} achieved in this work were due to the small V plate area in comparison to the wall chamber, where -V_{dc} values depend on the ratio of areas between wall chamber and V plate (corresponding to anode and cathode) of the deposition system. This relation is given by the equation as below:

$$(S_A/S_K)^n, \text{ n}\sim4 \ldots \text{(2-2)}$$

where S_A is the anode (chamber wall) area and S_K is the cathode (V plate) area, respectively. Due to this relation, in this work, the constant size of V plate (50 × 50 mm^2) was used to avoid inconsistency of the -V_{dc} value. In this work, VO_2 thin films were deposited on double side polished Al_2O_3 (001) (10 × 10 mm^2) substrates by rf magnetron reactive sputtering equipped with the rf substrate biasing set-up. The substrate was ultrasonically cleaned in acetone for 3 min and rinsed in pure water before being placed in the sputtering chamber. The substrate was placed at

the same position of Ø30 mm from the center to avoid difference due to magnetron effect.

In order to discuss the effect of substrate biasing on the growth of the VO_2 films, all the deposition conditions were set constant. The depositions were performed in 0.5 Pa mixture ambient of O_2 and Ar gasses, where O_2 and Ar flow rates were at 2.5 and 38 sccm, respectively. Substrate temperature (T_S), target rf power, and deposition time were constant at 400°C, 200 W, and 40 minutes. In order to systematically study the effect of this method, the depositions were performed at four different substrate biasing power of 0, 10, 20, 30, and 40 W. One should note that, 0 W deposition was conducted while the substrate was grounded.

2.2.2 Films Characterization

VO_2 crystalline growth of the deposited films was analyzed by X-ray diffractometry (XRD, X'Pert MRD Philips Co.) using Cu Kα radiation (wavelength of 1.5418 Å), where 2θ-θ scans measurements were mainly performed. The epitaxy of the sputtered VO_2 films was analyzed by performing omega scans and in-plane phi scans, and by taking pole figure of high-resolution XRD measurements. Field emission scanning electron microscopy (FE-SEM) measurements were performed to study the effect of ion energy on the morphologies and also the film thickness.

IMT properties of film resistance *versus* temperature characteristics (*R–T* characteristics) were measured by a two-point probe method using tungsten carbide tips, where the distance between the two tips was constant at 1.0 mm. A Peltier heater stage was introduced for controlling the sample temperature, in which the temperature was swept over 20–100°C at a rate of 4 °C/min. *R–T* characteristics were converted to resistivity against temperature curves (ρ-*T* characteristics) by taking resistivity value at room temperature measured by a four-point probe method into account. In respect to the IMT properties, transition temperature for both heating and cooling ($T_{\text{IMT-H}}$ and $T_{\text{IMT-C}}$) were defined as the peak temperature of the $\mathrm{d}(\log_{10}R)/\mathrm{d}T$ curve for heating and cooling runs. As a reminder, in the present work, transition temperature (T_t) will be discussed in corresponding to the IMT's transition temperature for the heating runs. Temperature-dependent infrared (IR) transmittance properties were measured by a homemade measuring set-up, utilizing a light-emitting diode (LED) with a wavelength of 1.45 μm was used as a laser light and a photodiode was used to convert a light signal into a current.

Temperature-dependent micro-Raman measurements were carried out to study the SPT. Measurements were performed by using a reflex device (Renishaw, inVia) and a temperature controller (Linkam, THMS 600). An argon-ion laser with 514.5 nm in wavelength and 0.5 mW in power was used as the excitation light source. Transition phase ratio was deduced by taking VO_2 peaks area of the M1 phase and R phase into the account and thus allow the SPT's transition temperature (T_{SPT}) to be obtained. T_{SPT} was calculated from the derivative curve of $\mathrm{d}(\log_{10}$ M1 ratio$)/\mathrm{d}T$ *vs*. temperature. Valence band structures near the Fermi level (E_F) was observed by performing temperature-dependent ultraviolet photoelectron spectroscopy (UPS) measurements. Emission of He II with a photon energy of 40.8 eV (VG-Scienta, VUV5000+5040) was used as a light source, and low energy resolution of 0.03 eV was achieved by using a hemispherical electron analyzer (VG-Scienta, SES-100). Before the measurements, films were directed to argon ion sputtering to expose a clean surface of each film to the UV light. The absolute value of binding energy was calibrated by the Fermi edge of evaporated Au films.

2.3 Results and Discussion

2.3.1 Crystalline Properties Characterization of X-Ray Diffraction (XRD) Patterns for VO_2 Films Deposited by Reactive Sputtering with Substrate Biasing

VO_2 films were deposited on Al_2O_3 (001) substrates by varying the substrate biasing power from 0 to 40 W. In this section, crystalline properties of films deposited with the substrate biasing power of 0, 10, 20, 30, and 40 W will be discussed.

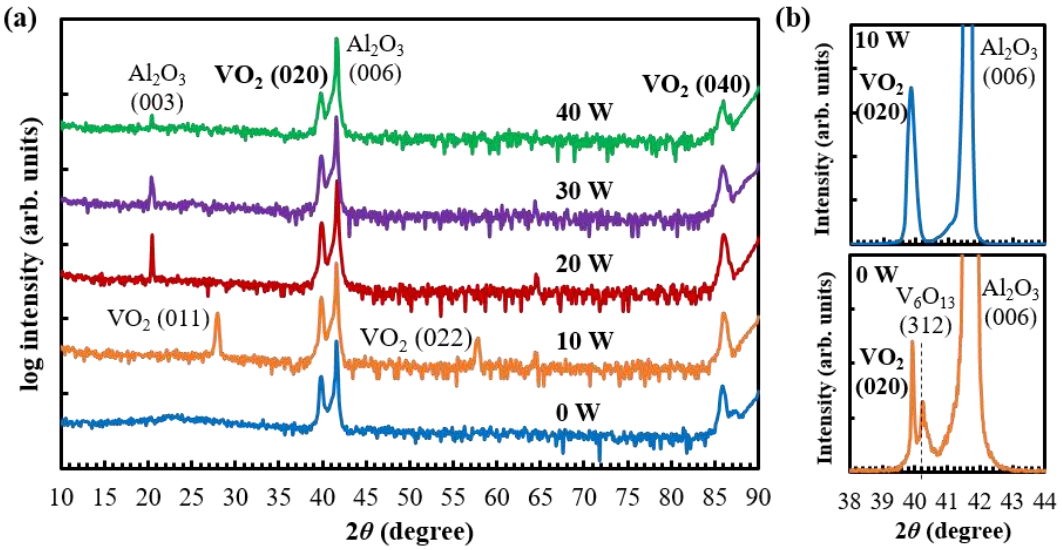

Fig. 2-6 (a) XRD 2θ-θ scan profiles for VO_2 films deposited with substrate biasing power from 0 to 40 W. (b) Enlarged XRD pattern for films of 0 and 10 W between a 2θ range of 38º and 44º.

Figure 2-6 (a) shows the XRD 2θ-θ scan profiles of VO_2 films on Al_2O_3 (001) substrates deposited with substrate biasing power of 0, 10, 20, 30, and 40 W. In each film, peak appeared at $2\theta = 41.69°$ corresponds to the substrate's peak of Al_2O_3 (006) plane. Also, another substrate peak diffraction of (003) plane was also observed at around $2\theta = 20.49°$. The growth of VO_2 films on Al_2O_3 (001) substrates were confirmed by the appearance of peaks at around $2\theta = 39.85°$ and $2\theta = 86.85°$ that correspond to the monoclinic VO_2 $(020)_{M1}$ and $(040)_{M1}$ planes, respectively. The appearance of these two VO_2 peaks confirmed the out-of-plane b_M-axis orientation growth of the VO_2 films deposited by reactive sputtering with substrate biasing, agreeing on the epitaxial crystalline growth of VO_2 films on Al_2O_3 (001) substrates explained in the introduction before.

On the film of without biasing, the growth of high oxidation phase, V_6O_{13} was also observed, as a peak at $2\theta = 40.26°$ that belongs to V_6O_{13} (312) plane was detected in the XRD pattern. To confirm the existence of this peak as only a double peak feature was observed in the wide XRD

pattern, enlarged XRD pattern from 2θ = 38 to 44º was shown in Fig. 2-6 (b). The growth of the VO_2 + V_6O_{13} in the film of 0 W was due to excess oxygen flow during the deposition. The O_2 flow rate of 2.5 sccm applied in the present work was two times more higher than that frequently applied flow rate for growing high-quality VO_2 films.[84,90] Enlarged XRD pattern of the film deposited at 10 W revealed that peak belongs to V_6O_{13} (312) was disappeared as the biasing was applied. Observation on the disappearance of the V_6O_{13} as the rf substrate bias was applied, even while keeping the O_2 flow rate constant at 2.5 sccm suggests that the increasing of the ion energy during deposition hindered the growth of the high-oxidation phase. Also, one should be notified that the growth of VO_2 was preserved even the deposition was performed at a high substrate biasing power of 40 W with E_{ion} of around 300 eV.

In different to other sputtered VO_2 films on Al_2O_3 (001) substrates, film of 10 W shows a characteristics growth orientation, where peaks at 2θ = 27.85° and 2θ = 57.85° that correspond to VO_2 $(011)_{M1}$ and $(022)_{M1}$ planes were observed to grow together with the typically observed $(020)_{M1}$ and $(040)_{M1}$ planes. This growth behavior was observed to have a good reproducibility, which thus requires particular studies to be carried out. Results of these studies on the extraordinary growth of film deposited at 10 W will be delivered in chapter 4.

Also, from Fig. 2-6 (a), the intensity of $(020)_{M1}$ peak was observed to apparently decrease on film of 40 W. To discuss the VO_2 $(020)_{M1}$ peak behavior, enlarged $(020)_{M1}$ peak of films deposited at 0, 10, 20, 30, and 40 W is shown in Fig. 2-7 (a). As one can observe, intensity of the $(020)_{M1}$ peak firstly increased in films of 10 and 20 W. However, increasing the substrate biasing power to 30 and 40 W was observed to result in the decreasing of the peak intensity. To further discuss these matters, quantitative analysis was performed by correspondingly define the area of the Gaussian curves of the $(020)_{M1}$ peak. The Gaussian function was used to fit the XRD profiles of all films. Gaussian curves (yellow dashed line) and calculated area (marked in red and green) of films deposited at 20 and 40 W are shown in Fig. 2-7 (b) and (c), respectively.

Calculated area of the VO_2 $(020)_{M1}$ peak of films deposited from 0 to 40 W, was summarized as a function of substrate biasing power in Fig. 2-7 (d) with the corresponding ion energy shown as an upper horizontal axis. A small area of the $(020)_{M1}$ peak in the film of 0 W was expected due to the excess flowing of the oxygen during the sputtering, correspondingly. Improved crystalline properties with significant increase in the $(020)_{M1}$ peak area were observed for films deposited at 10 and 20 W. As the energy of the ion irradiation increases with the increasing substrate biasing power later than 20 W, VO_2 $(020)_{M1}$ peak area was observed to decrease, suggesting that the crystalline growth properties of VO_2 on Al_2O_3 (001) substrates could be optimized by selecting

the substrate biasing power. However, it should be notified that the oriented growth of VO_2 films was preserved even in the film deposited with ion energy of 300 eV that achieved during substrate biasing power of 40 W. From these results, one could propose that this rf substrate biasing method enables control of the ion energy that could be effective for controlling the growth behavior of VO_2 films.

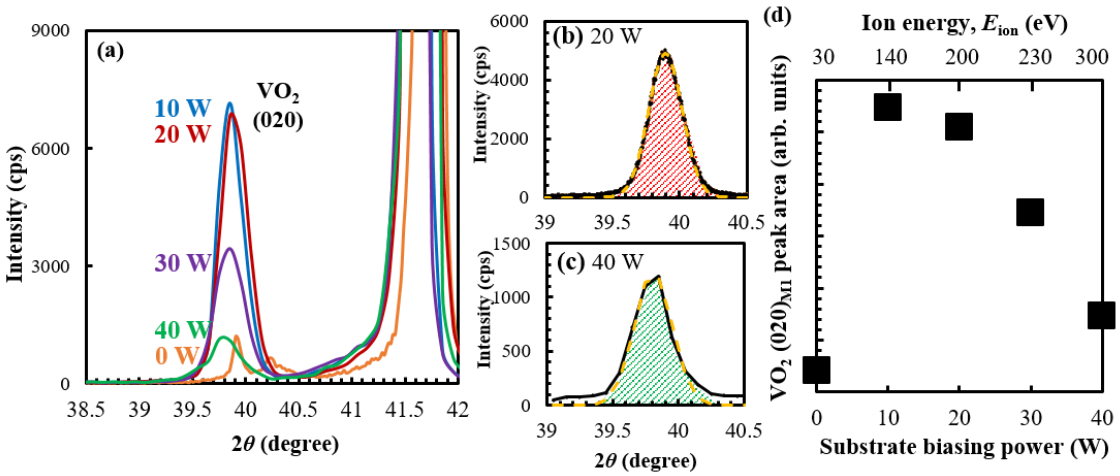

Fig. 2-7 (a) Enlarged XRD profiles of films deposited at 0 to 40 W. Gaussian fitted curves of $(020)_{M1}$ peak for films of (b) 20 and (c)40 W. (d) Calculated area of the Gaussian fitted curves for all films.

Preserved epitaxy properties in the film deposited with high-energy ion irradiation of 40 W were confirmed by performing high-resolution XRD measurement of in-plane phi scan analysis and selected area electron diffraction (SAED) measurement. The in-plane phi scan profiles and SAED pattern of film deposited at 20 W with the best crystalline properties were also taken for comparison. Figures 2-8 (a) and (b) present the results of the XRD analysis of the in-plane phi scan profiles and pole figures taken for films of 20 and 40 W. In-plane phi scan measurements were performed for both peaks of Al_2O_3 and VO_2 with an inclination of 57.76° and 44.94° of Al_2O_3 (012) and VO_2 $(011)_{M1}$, respectively. The phi scan profiles confirmed the six-fold symmetry of VO_2 $(011)_{M1}$ reflections as well as three-fold symmetry of Al_2O_3 (012), supporting the epitaxial growth of VO_2 $(020)_{M1}$ on Al_2O_3 (001) substrate for both films of 20 and 40 W. These six peaks of VO_2 $(011)_{M1}$ appeared in the in-plane phi-scan profiles were attributed to the two-fold symmetry of VO_2 $(020)_{M1}$ that growth in three different directions, where each grain was rotated by 120° from each other on the Al_2O_3 (001) substrate. From the phi scan profiles, one can understand that the VO_2 films grow on Al_2O_3 (001) substrates have an epitaxial relation of VO_2 $(010)_{M1}$ $[100]_{M1}$ ‖ Al_2O_3 (001) [100], [100], $[\bar{1}\bar{1}0]$. In corresponding to the observed phi scan profiles, pole figures were illustrated as also shown in Fig. 2-8.

SAED measurement was also performed to confirm the epitaxial growth of the sputtered VO_2 films. The diffraction spot patterns as shown in Fig. 2-9 revealed the typical growth pattern of VO_2 $(020)_{M1}$ on Al_2O_3 (001) substrates for both films, supporting the results of that the epitaxial relations were preserved even in the film deposited with high-energy ion irradiation of 300 eV.

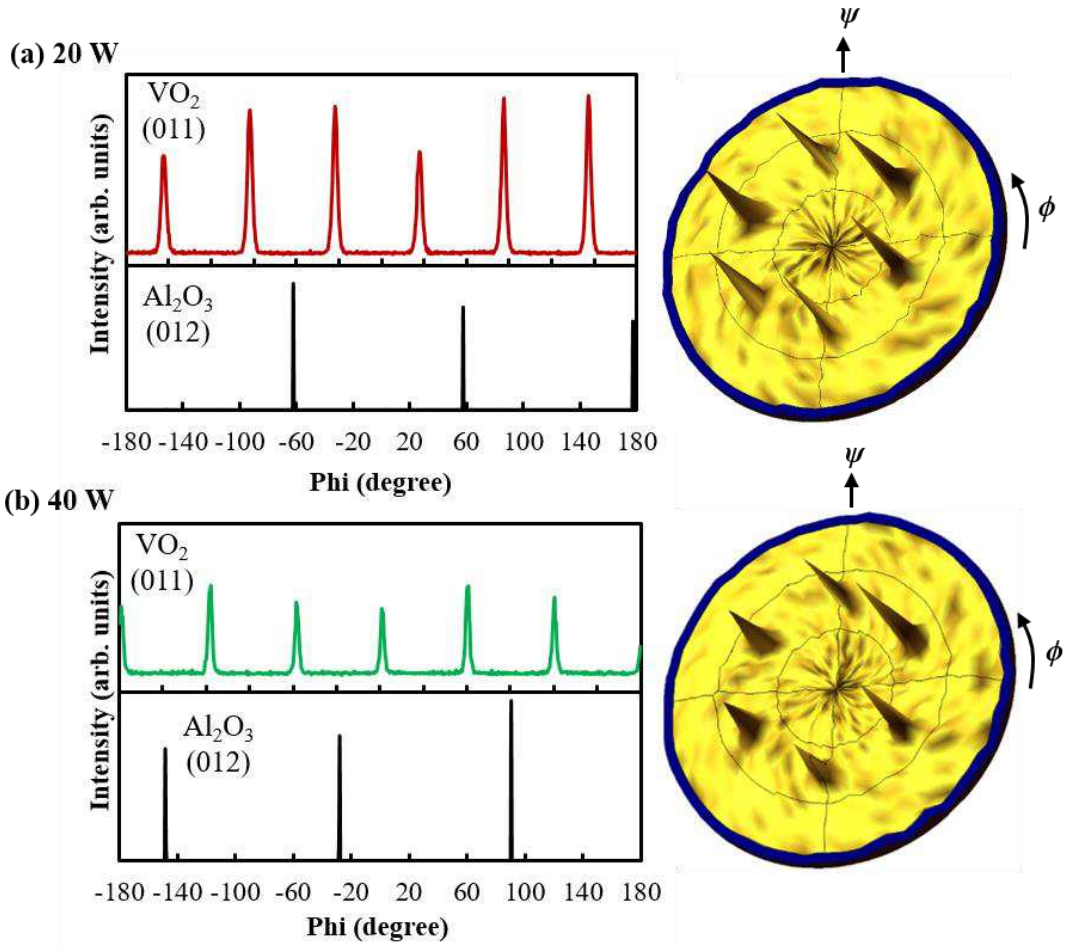

Fig. 2-8 High-resolution XRD analysis of in-plane phi scan profile and pole figure for films deposited at (a) 20 W and (b) 40 W.

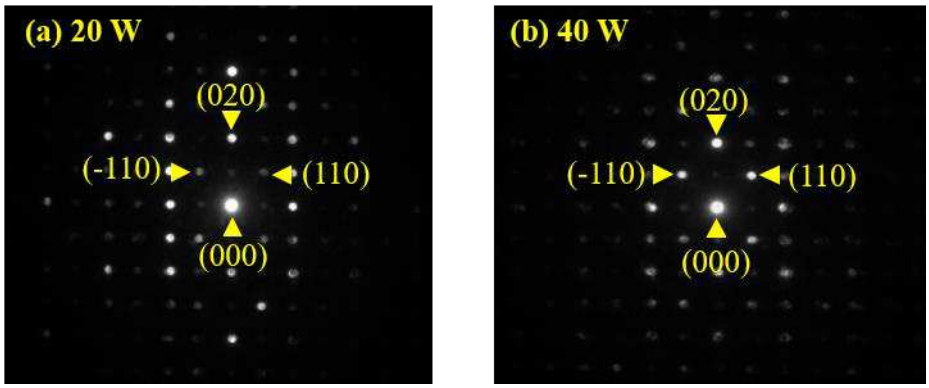

Fig. 2-9 Selected area electron diffraction (SAED) images for films of (a) 20 W and (b) 40 W. Reproduced from [ref. 96 of J. Appl. Phys. **119**, 55308 (2016)], with the permission of AIP Publishing.

2.3.2 Field Emission Scanning Electron Microscopy (FE-SEM) Images for Surface and Cross-sectional Views of VO_2 Films Deposited by Reactive Sputtering with Substrate Biasing

The growth of VO_2 was observed to be preserved despite the high-energy ion irradiation of around 300 eV achieved by applying substrate biasing power of 40 W. Increasing of the ion energy during deposition was reported to change the morphology of thin films significantly.[91] Thus, in this work, in which high-energy ion irradiation was introduced, it is definitely required to study the morphologies of the VO_2 films deposited by the reactive sputtering with substrate biasing. FE-SEM measurements were performed for both surface and cross-sectional views to discuss these morphology changes in the sputtered VO_2 films. Figure 2-10 shows the surface view of the FE-SEM images of films deposited at 0, 10, 20, 30, and 40 W.

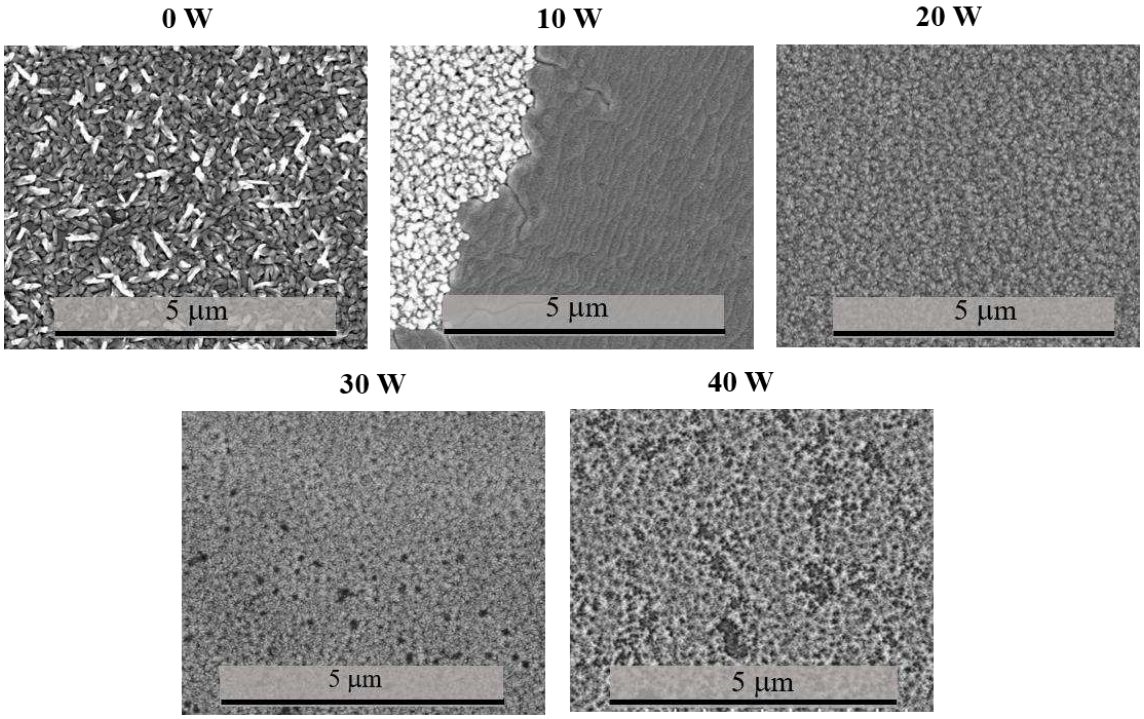

Fig. 2-10 Surface view of FE-SEM measurements for films deposited with biasing power of 0 to 40 W.

As shown in the surface images in Fig. 2-10, surface morphologies of the sputtered films was observed to change with the increasing substrate biasing power. The film of without biasing shows mixed grains growth, in which, small grains with size of several hundred nm were observed together with white color of rod-like grains. These small grains with size of several hundred nm are the typical grain features observed in case of VO_2 films grown on Al_2O_3 (001) substrates. This result of film deposited at 0 W was in agreement with the VO_2 and V_6O_{13} mixed growth of the film observed in the XRD 2θ-θ scan profiles given before (Fig. 2.6 (a)).

As the substrate biasing power applied, the rod-like grains were no longer observed, agreeing the single growth phase of VO_2 on films deposited by reactive sputtering with the substrate biasing method. At the biasing power of 10 W, unusual μm-sized crystalline grains were observed together with the conventional nm-sized VO_2 grains. This unusual grain growth of VO_2 crystals was different from the usual thin films growth properties, where the grain sizes were supposed to be smaller or equal to its film thickness. Further details discussion on this extraordinary growth behavior of film deposited at 10 W will be discussed in chapter 4. In comparison to the VO_2 nanograins observed on film of 0 W, rather large size of VO_2 nanograins with an average size of 150 nm were observed in the film of 10 W.

In Fig. 2-10, as the substrate biasing power increases, densification of the grains was observed due to the continuous energetic particles striking to the films during the deposition. The film of 20 W shows a homogeneous crystalline grains growth with the grains densification occurs, resulting in rather smaller crystalline grains with a rather smoother surface. Later, after a certain biasing power (30 W with ion energy of around 230 eV, in this work), hole-like features started to appear, as further grains densification occurs due to the high energy ions incidence. The appearance of such hole-like features in films deposited by high biasing power could also be caused by the re-sputtering process that simultaneously occurs during the sputtering deposition, due to the continuous high-momentum ions strike to the films. In the film of 40 W, small grains of VO_2 with the domination of the hole-like features were observed. Despite the hole-like features that were observed to dominate the growth on film of 40 W, as was mentioned before, the crystalline properties of this film are still well preserved.

Besides the densification of the grains, film thickness was also observed to decrease proportionally with the increasing of substrate biasing power. Figure 2-11 shows a cross-sectional view of FE-SEM images for films of 0, 10, 20, 30, and 40 W. Film thickness was decreased from 240 nm at 0 W to 150 nm at 20 W while maintaining all other deposition conditions unchanged. Later, as the biasing power increases to 40 W, the film thickness decreased to about 80 nm. Even so, all the films are thicker than the critical thickness. The decreasing of the film thickness with the increasing substrate biasing power significantly proposed the increasing of the re-sputtering rate during the deposition. From the film thickness value shown in Fig. 2-11, deposition rate and re-sputtering rate occur at the substrate during the deposition are calculated and shown in Fig. 2-12 as a function of substrate biasing power, respectively. As one can observe, with the increasing of substrate biasing power, deposition rate decreases from 6 nm/min at 0 W to nearly 2 nm/min at 40 W. In contrast, re-sputtering rate is significantly increased from 1 nm/min at 10 W to almost 4 nm/min at 40 W.

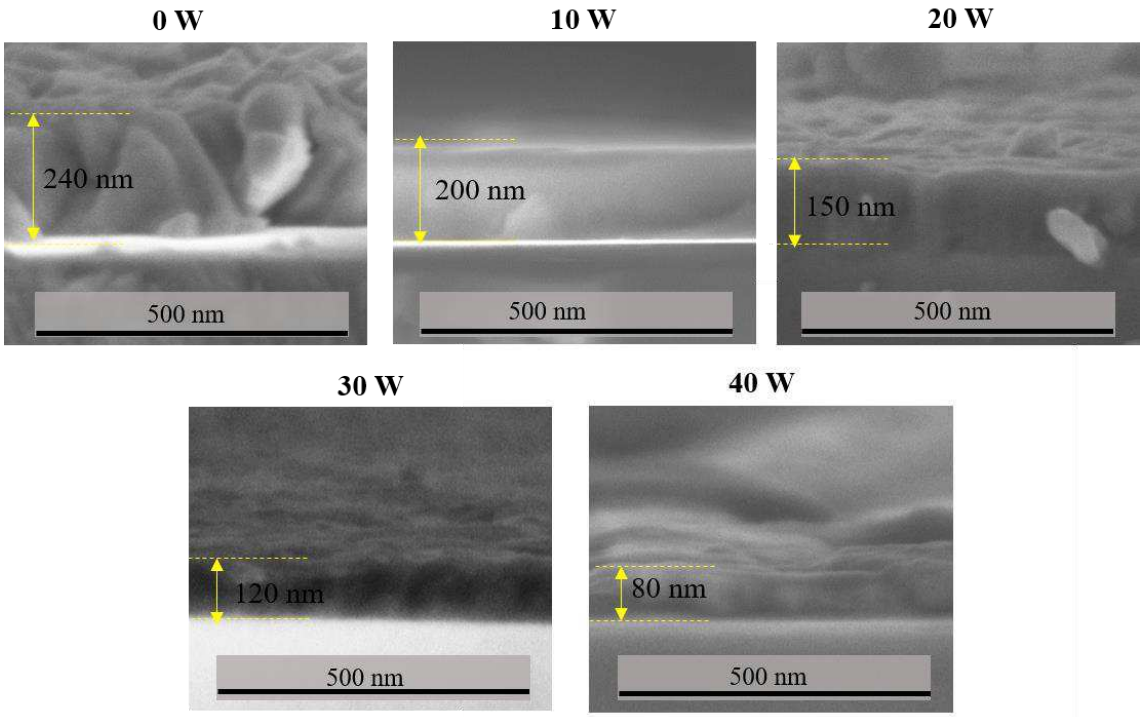

Fig. 2-11 Cross-sectional view of FE-SEM measurements for VO_2 films of 0 to 40 W.

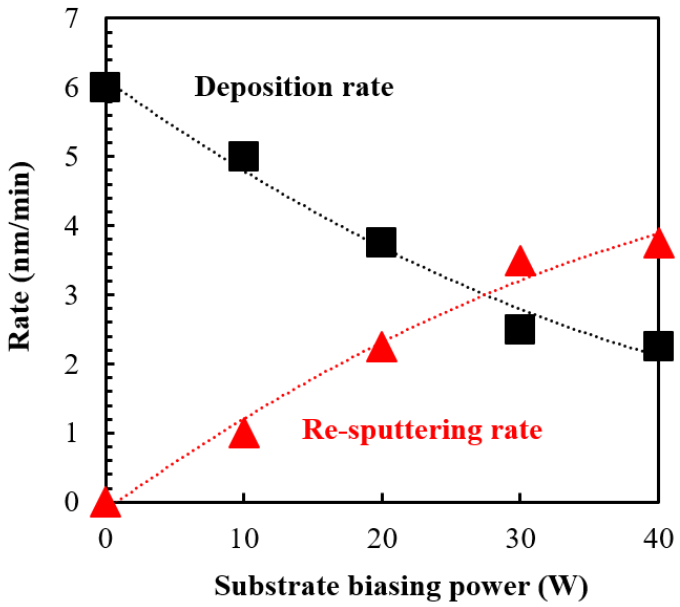

Fig. 2-12 Deposition rate and re-sputtering rate at the substrate with the increasing of substrate biasing power.

2.3.3 Insulator-Metal Transition (IMT) Properties of VO_2 Films Deposited by Reactive Sputtering with Substrate Biasing

As mention earlier, VO_2 thin films have been studied for their occurrence of IMT near room temperature. In this work, the substrate biasing method was introduced to investigate the possibility of modifying the transition temperature in the VO_2 films. In this section, those results of the IMT modifications in the VO_2 films on Al_2O_3 (001) substrates deposited by reactive sputtering with the substrate biasing power of 0, 10, 20, 30, and 40 W will be discussed.

In respect to the growth of VO_2 films deposited at 0, 10, 20, 30, and 40 W, IMT transition with a drop in electrical resistance, which is a characteristic feature of VO_2 was observed in all films. As one can observe, significant modifications in IMT properties with shift of the transition temperature (T_t) towards low temperature was observed with the increasing of substrate biasing power, while keeping all the deposition conditions constant.

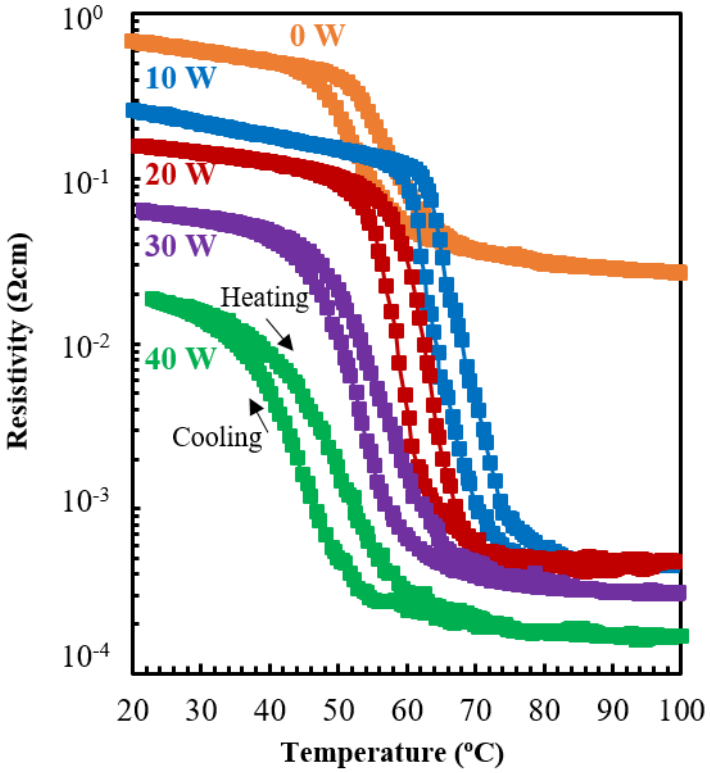

Fig. 2-13 Resistivity *vs*. temperature (ρ-T) characteristic of films deposited at 0, 10, 20, 30, and 40 W.

Figure 2-13 shows ρ–T characteristics for VO_2 films deposited on Al_2O_3 (001) substrates as a function of substrate biasing power. The transition for only around 1.5 order-of-magnitude was observed in the film deposited at 0 W. This small transition ratio in the film of without biasing

was due to its mixed growth states of VO_2 + V_6O_{13}. As the growth of high-oxidation phase was hindered with the applying of the substrate bias, rather larger transition width of nearly 2.5 order of magnitude changes were observed in films of 10 and 20 W. Signifying the improvement of the crystalline properties of film deposited at 20 W, sharp transition properties with an improvement in metallic phase was observed, where significant increase of the resistivity with the increasing of temperature was observed. One should be notified that the resistivity changes of nearly two order of magnitude were observed even in films with the transition occurred at a rather lower temperature of films deposited at 30 and 40 W. Figure 2-13 proposed certain IMT modifications of VO_2 films deposited by the rf substrate biasing method. However, in order to precisely describe the T_t modifications effect of the sputtered films, transition temperature calculation of $d(\log_{10}R)/dT$ curve will be needed.

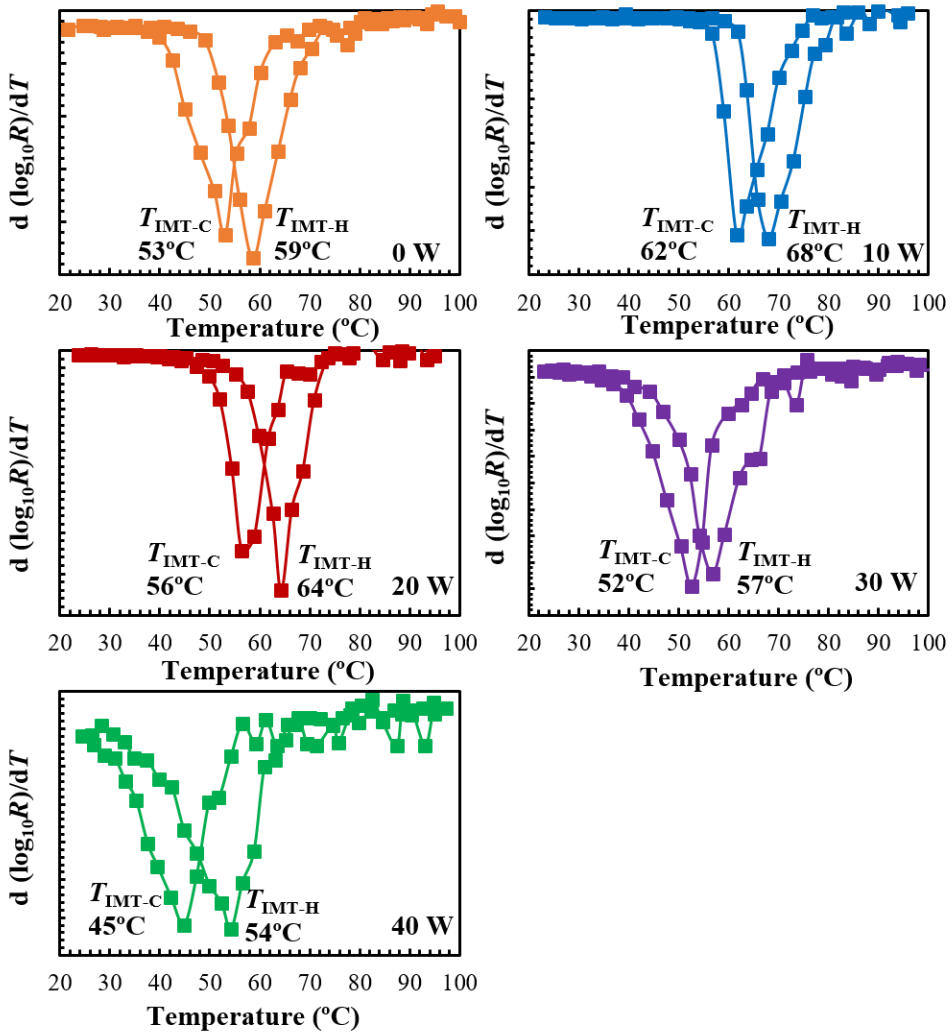

Fig. 2-14 Derivative curve of d $(\log_{10}R)/dT$ for VO_2 films deposited at 0, 10, 20, 30, and 40 W.

Figure 2-14 shows derivative curves plotted for films deposited at biasing power of 0, 10, 20, 30, and 40 W, where both IMT's transition temperature for heating and cooling were calculated and indicated as $T_{IMT\text{-}H}$ and $T_{IMT\text{-}C}$, respectively. Significant changes in T_{IMT} (referred to the $T_{IMT\text{-}H}$) value was observed, where the T_{IMT} first increases, then decreases with the increasing of substrate biasing power. In comparison to the reported T_{IMT} value of bulk VO_2 single crystal (at 68ºC), rather lower T_{IMT} of about 59ºC was observed on film of 0 W. This might be due to the low-quality of VO_2 crystalline structure, resulted by the excess O_2 flow during the deposition. As the substrate biasing power increases to 10 W, T_{IMT} was observed to increase to around 68ºC. Increasing the substrate biasing power to 20, 30, and 40 W was observed to result in a significant decrease of the $T_{IMT,}$ where the T_{IMT} at around 64, 57, and 54ºC were obtained for films of 20, 30, and 40 W.

An extensive shift of the T_{IMT} was observed in the film deposited at high-energy ion irradiation of 300 eV of biasing power 40 W. While most other research of VO_2 films on Al_2O_3 (001) substrates results in rather higher T_{IMT}, rf substrate biasing method introduced in the present work succeeded in lowering the T_{IMT} to 54ºC, almost 14ºC lower than the bulk. Also, it should be noted that decreasing of the T_{IMT} in this work was achieved while maintaining both the transition and the hysteresis properties. The hysteretic behavior indicates the coexistence of two phases over a finite temperature range due to superheating and supercooling effects, which was intrinsic of the first-order transition. Summarize results of the ρ-T characteristics, including their $T_{IMT\text{-}H}$ and $T_{IMT\text{-}C}$ for all films, were summarized in Table 2-1.

Table 2-1 Summarized IMT properties of films of 0, 10, 20, 30, and 40 W.

Biasing power (W)	$T_{IMT\text{-}H}$ (ºC)	$T_{IMT\text{-}C}$ (ºC)	Hysteresis width ($T_{IMT\text{-}H} - T_{IMT\text{-}C}$) (ºC)	Resistance ratio ($\rho_{RT}/\rho_{100ºC}$)
0	59	53	6	2.5×10^1
10	68	62	6	5.8×10^2
20	64	56	8	3.8×10^2
30	57	52	5	2.1×10^2
40	54	45	9	1.2×10^2

Three series of depositions were performed to confirm the reproducibility of the T_{IMT} modifications triggered by the rf substrate biasing. Figure 2.15 shows the ρ-T characteristics of all three series depositions. Variations in the T_{IMT} for both heating and cooling runs for sputtered VO_2 films in functions of substrate biasing power were summarized in Fig. 2.16. The ranges of

the temperature shifts was observed to increase with the increasing substrate biasing power, but, in overall, the T_{IMT} modifications patterns were consistent for all deposition series. This temperature ranges shift in the T_{IMT} was expected due to the slight changes in the $-V_{dc}$ achieved at the substrate that might be caused by the oxidation of the V plate or the occurrence of applied power reflectance at either target or substrate during the deposition. Also, the shifting of the transition temperature in cooling runs was similar to those in heating runs, meaning that the thermal hysteresis width is independent of the substrate biasing power. Furthermore, about two orders of magnitude change in resistance were preserved in all films.

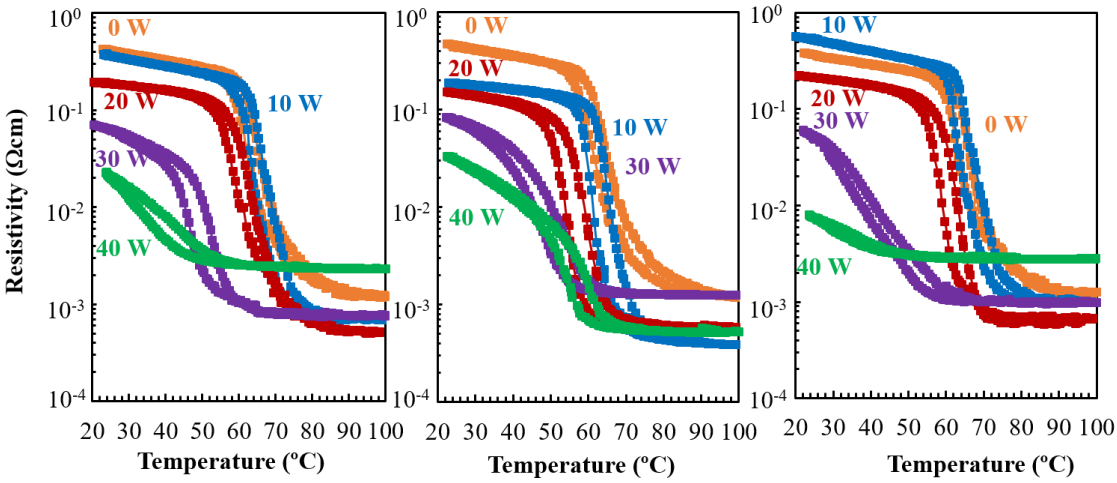

Fig. 2-15 Variation of ρ-T characteristics measured for different deposition series of sputtered VO_2 films deposited at 0, 10, 20, 30, and 40 W.

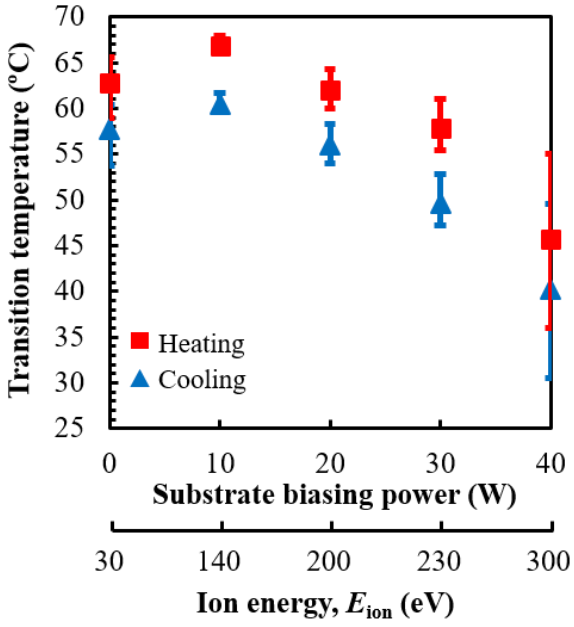

Fig. 2-16 Variations of T_{IMT} in films deposited in three different series of depositions.

From these results of three series of depositions, consistent T_{IMT} modifications pattern in the sputtered VO_2 films was observed, giving the certainty of the T_{IMT} modifications in the VO_2 films deposited by the reactive sputtering with substrate biasing, thus confirming the ability of the rf substrate biasing method on controlling the IMT in the VO_2 films, in which there are no deposition conditions changes are needed.[92]

For futher dicussion on the modifications of the transition properties of films deposited by reactive sputtering with substrate biasing, analysis on the SPT and the valence bands behavior are certainly needed. For that matter, series with the sharpest transition and the lowest T_{IMT} value achieved in the films deposited at 20 W and 40 W was chosen. Corresponded IMT properties for films of 0, 10, 20, 30, and 40 W that used for studying the effect of substrate biasing are shown in Fig. 2-17. As one can observe, as the substrate biasing power increases from 0 W to 10 W, and later to 20, 30, and 40 W, the T_{IMT} first increased from 66ºC to 69ºC, and later decreased to 65, 55, and 36ºC, respectively. In addition to the T_{IMT} at almost room temperature for the film deposited at 40 W, the large transition ratio of nearly 10^2 is one that should be notified. In respect to the IMT properties shown in Fig. 2-17, a summary of that IMT properties is given in Table 2-2.

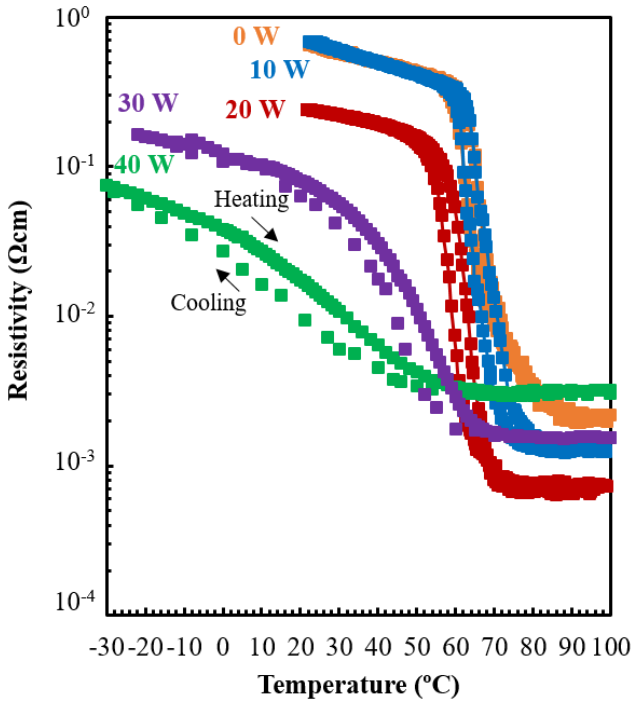

Fig. 2-17 *ρ-T* characteristics for films deposited at 0, 10, 20, 30, and 40 W to be used for discussion.

Table 2-2 Summarize IMT properties for films deposited at 0, 10, 20, 30, 40 W.

Biasing power (W)	T_{IMT-H} (ºC)	T_{IMT-C} (ºC)	Hysteresis width ($T_{IMT-H} - T_{IMT-C}$) (ºC)	Resistance ratio ($\rho_{RT}/\rho_{100ºC}$)
0	66	61	5	4.7×10^{2}
10	69	62	7	5.8×10^{2}
20	65	57	8	3.8×10^{2}
30	55	49	6	1.1×10^{2}
40	36	30	6	6.4×10^{1}

2.3.4 Temperature-dependent Raman Measurements for SPT Analysis in VO_2 Films Deposited by Reactive Sputtering with Substrate Biasing

The occurrence of IMT in VO_2 is accompanied by the structural phase transition (SPT). In this work, in which the T_{IMT} was significantly decreased with the increasing of substrate biasing power, observation on the SPT would needed, especially for the film of 40 W, where the transition occurred near room temperature. In order to study the occurrence of SPT in the VO_2 films deposited by reactive sputtering with substrate biasing, temperature-dependent Raman measurements were performed. In low-temperature M1 phase, 18 Raman active modes (9Ag and 9Bg) are allowed. In contrast, in the high-temperature R phase, only four modes of A_{1g}, B_{1g}, B_{2g}, E_g are confirmed. Schilbe *et al.* performed comprehensive Raman scattering measurements on both M1 and R phases of VO_2 bulk crystal, where out of the 18 allowed modes, 17 sharp Raman peaks in the M1 phase and four broad peaks in the R phase were observed.[93] In this section, temperature-dependent Raman spectra will be used to evaluate the crystalline growth properties of VO_2 films as well as their structural phase transition.

Figure 2-18 shows the temperature-dependent Raman spectra of VO_2 films deposited at 0, 10, 20, 30, and 40 W. Spectra shown as blue line is the one measured for low-temperature monoclinic M1 phase, and the red line remarks the completion of SPT from M1 to R structure. 11 characteristic peaks of VO_2 M1 phase were observed at 132, 193, 224, 261, 310, 336, 386, 440, 498, 615 and 825 cm^{-1} in films of 0, 10, and 20 W measured at room temperature of 23ºC, and in the films of 30 and 40 W measured at low temperature of -195ºC. The observation of these peaks in the film of 30 and 40 W evidenced the existence of VO_2 M1 crystalline lattice at a very low temperature of -195ºC. In the case of the film deposited at 0 W, an additional peak at 143 cm^{-1} suggests a mixture growth of VO_2 with the V_nO_{2n+1} phase of V_2O_5.[94] This peak was observed to have an insignificant change with the increasing of temperature, supporting the characteristics of V_2O_5 that undergo semiconductor-to-metal transition at a higher temperature of around 250ºC. This peak was no longer observable as the substrate biasing power been applied, supporting the growth of a single phase VO_2 in films deposited by reactive sputtering with rf substrate biasing.

As temperature increases, VO_2 M1 peaks completely disappeared at 75ºC on the films of 0 and 20 W, suggesting the completion of the SPT from the low-temperature M1 to the high-temperature R phase. In different with that completion of the SPT at 75ºC on the films deposited at 0 and 20 W, the film of 10 W was observed to show a completion of SPT at a rather higher temperature of 80ºC. In contrast, the disappearance of M1 peaks on the film of 30 W was observed to occur at a rather low temperature of 70ºC. Among these films, the film deposited at 40 W shows

a different transition behavior with an obvious early onset of the SPT was observed. The peak positions do not obviously change until -20°C, but noticeably get weaker as getting near the room temperature of 20ºC. Later, at 50ºC, those VO_2 M1 peaks disappeared, indicating the completion of the SPT to the R phase. These results are consistent to the T_{IMT} modification observed in the ρ-T characteristics shown in Fig. 2-17, where the T_{IMT} shifted to rather higher temperature at the biasing power of 10 W, then shifted to lower temperature as the biasing power increases to 20, 30, and 40 W. Note that, a peak appeared at 415 cm^{-1} on films of 30 and 40 W, is recognized to be a substrate's peak that appeared due to the noticeable film thickness decreased in films deposited at 30 and 40 W.

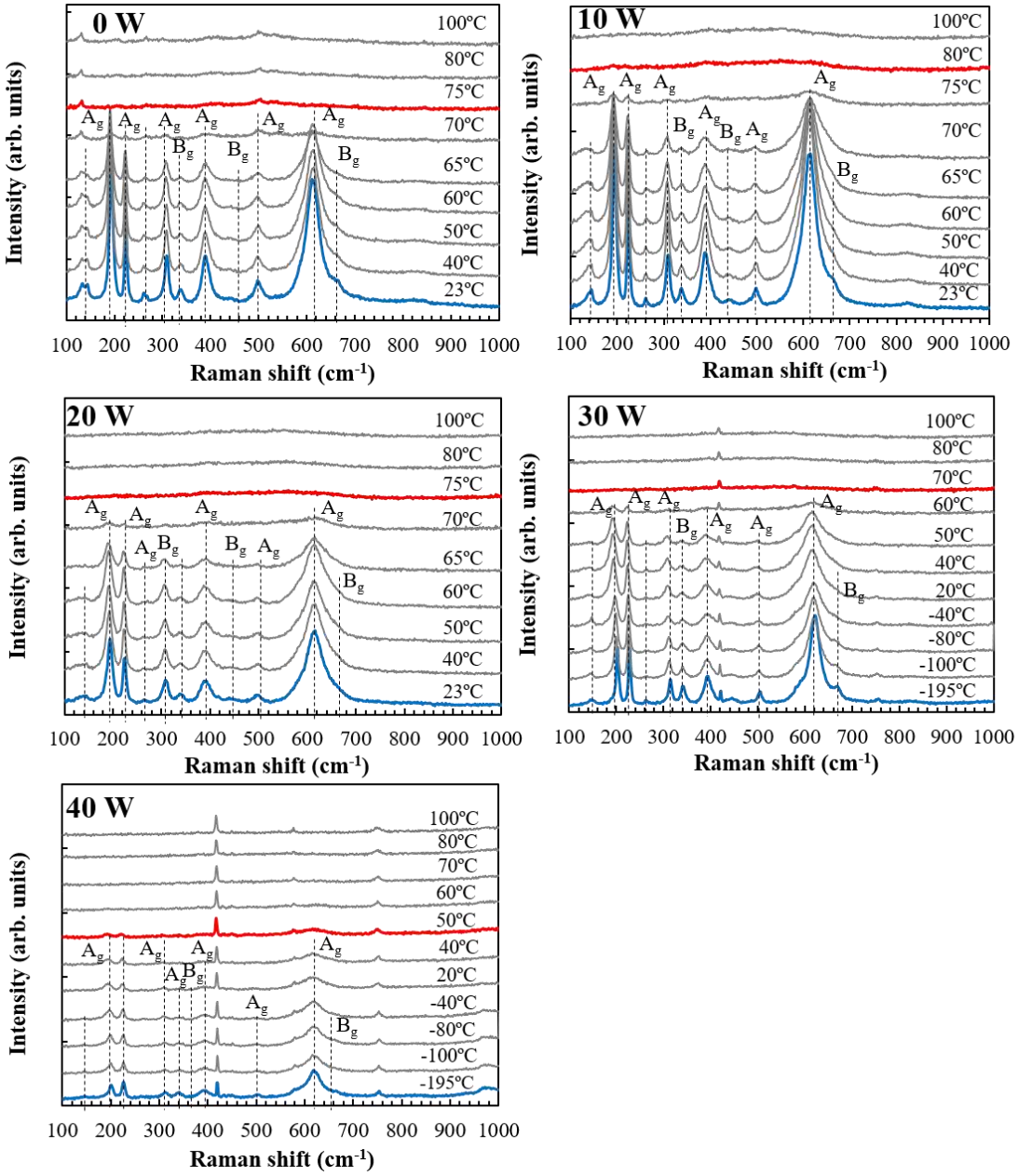

Fig. 2-18 Temperature-dependent Raman spectra for VO_2 films deposited at 0, 10, 20, 30, and 40 W.

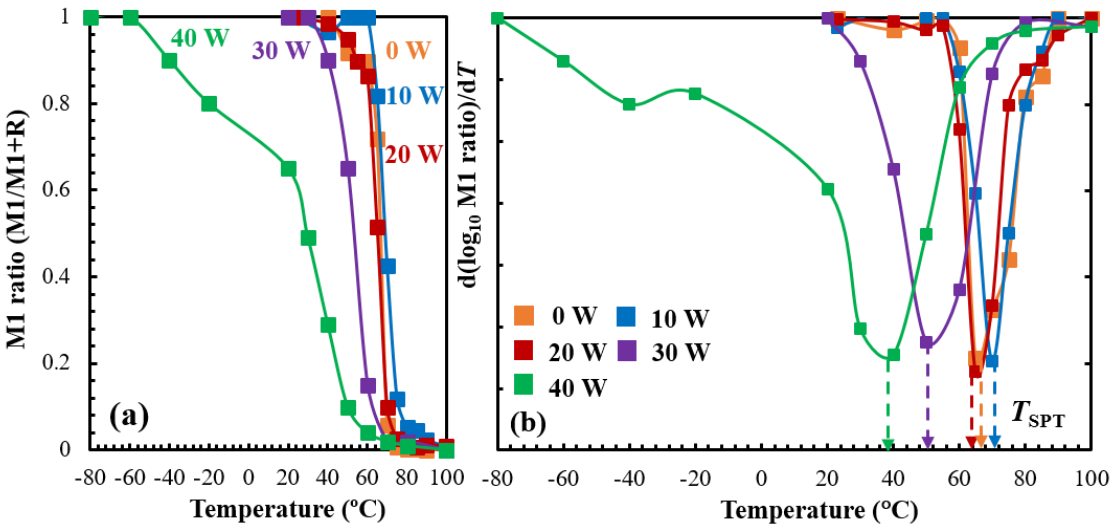

Fig. 2-19 (a) VO_2 M1 phase ratio changes with the increase of temperature and (b) derivative d($\log_{10}$ M1 ratio)/dT of phase transition temperature, T_{SPT} for films of 0, 10, 20, 30, and 40 W.

To further studying the SPT on the VO_2 films deposited by substrate biasing, transition phase ratio *vs.* temperature and SPT's transition temperature (T_{SPT}), were examined. Transition phase ratio was deduced by taking VO_2 peaks area of the M1 phase of 23ºC (for films of 0, 10, 20, and 30 W) and -80ºC (for films of 40 W), and R phase representative spectra of 100ºC into the account. This consideration was provided by assuming that the thermal evolution of the Raman spectra shows a transition from M1 to R phase, with the coexistence of only these two phases around the transition temperature. Minute procedure for obtaining the ratio was reported in elsewhere.[57] Figure 2-19 (a) shows VO_2 M1 phase ratio changes with the increasing of temperature. Films deposited at 0, 10, 20, and 30 W were observed to be completely in the VO_2 M1 phase (M1 phase ratio equal 1) at room temperature. In contrast, M1 ratio was observed to already decreased to almost half (M1 phase ratio equal 0.6) in the film of 40 W at room temperature.

SPT's transition temperature (T_{SPT}) was calculated from the derivative curve of d($\log_{10}$ M1 ratio)/dT *vs.* temperature as plotted in Fig. 2-19 (b). In comparison to the film of 0 W, whereas the T_{SPT} was around 66ºC, rather higher T_{SPT} was observed in the film of 10 W, which is around 70ºC. Further increasing of the substrate biasing power observed to result in a significant decrease of the T_{SPT}, where the T_{SPT} of 65ºC, 50ºC, and 38ºC was obtained for films of 20, 30, and 40 W, respectively. These results support the occurrence of IMT accompanying with the SPT as both transition temperatures (T_{IMT} and T_{SPT}) were observed to be in good agreement with each other in all VO_2 films deposited on Al_2O_3 (001) by reactive sputtering with substrate biasing. To compare both modifications in the T_{IMT} and T_{SPT}, the values of those transition temperatures were

plotted and presented in Fig. 2-20.

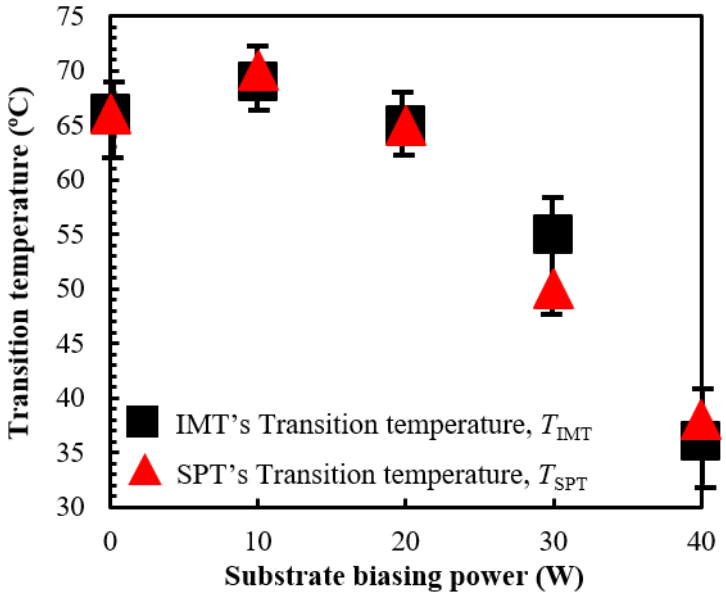

Fig. 2-20 Modifications of the transition temperatures in biased VO_2 films; T_{IMT} (plotted in square) and T_{SPT} (plotted in triangle).

Figure 2-20 shows the change of the T_{IMT} and the T_{SPT} values for the films of 0, 10, 20, 30, and 40 W. Note that, the T_{IMT} values plotted in the figure are the $T_{IMT\text{-}H}$ in corresponding to the IMT properties shown in Fig. 2-17. As one can observe, both transition temperatures show a similar modifications pattern, thus evidenced the lowering of the transition temperature (T_t) in the sputtered VO_2 films due to the high-energy ion irradiation. This result of the T_t modifications in the VO_2 films triggered by high-energy ion irradiation during the substrate biasing as a thing that should be notified by considering the well-preserved transition ratio and hysteresis behavior, without no changes in the deposition conditions will be needed.

2.3.5 Infrared (IR) Transmittance Properties of VO_2 Films Deposited by Reactive Sputtering with Substrate Biasing

VO_2 possesses reversible IMT triggered by changes in the temperature, accompanied by a distinct change in its infrared (IR) transmittance; hence make it as a suitable candidate material for the smart window applications. VO_2 films could be used for energy-saving coatings for windows could that block out the incident infrared light when the temperature is higher during summer; while in the meantime allowing the infrared light incident to pass through when the temperature is decreased in cold weather.[95]

As was introduced in sections 2.3.3 and 2.3.4, reactive sputtering with substrate biasing method succeeded in significantly modifying the transition temperature (T_t) to low temperature, close to the room temperature. The same modifications in the T_t are expected to occur also in the IR transmittance properties, which will then broaden the usage of VO_2 for the optical applications.

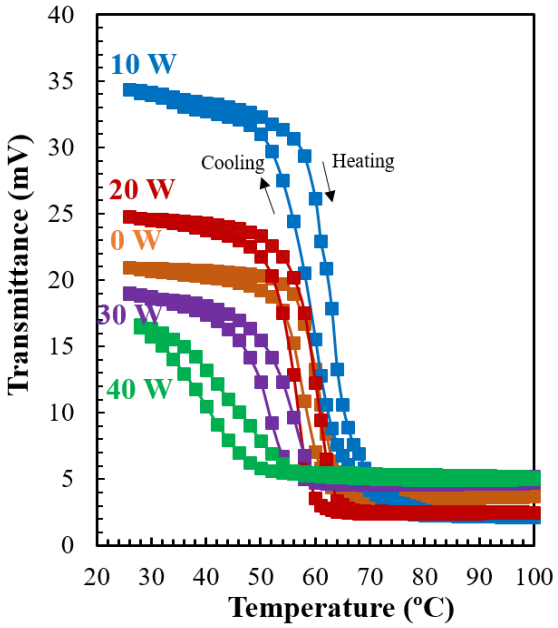

Fig. 2-21 Temperature-dependent IR transmittance properties of VO_2 films deposited with the substrate biasing power of 0, 10, 20, 30, and 40 W.

Figure 2.21 shows the temperature-dependent IR transmittance properties for both heating and cooling runs of VO_2 films deposited by reactive sputtering with substrate biasing power varied from 0 to 40 W. One can observe fully reversible optical transition properties for all films. As addition to that, by signifying the modifications of the T_t observed in IMT and SPT, modifications of the T_t was also observed in the IR transmittance properties, thus evidenced the lowering of the T_t in the sputtered VO_2 films due to the high-energy ion irradiation.

2.3.6 Temperature-dependent Ultraviolet Photoelectron Spectroscopy (UPS) for Valence Band Characterization

In previous sections, preserved crystalline properties of films deposited in high-energy ion irradiation and the occurrence of IMT and SPT at rather lower temperature were given. For further discussion about the transition from insulator to metallic phase, it is important to study the behavior of electronic valence band spectra for both low- and high-temperature states.

In order to investigate the electronic valence band spectra near the Fermi level (E_F), UPS measurements were performed for films with excellent crystalline properties and with the most extensive T_t shift prepared at 20 and 40 W, respectively. Figure 2-22 shows normalized wide UPS spectra of sputtered VO_2 films deposited with the substrate biasing power of 20 and 40 W, where the photoemission spectra were taken in the range of the binding energies consists the levels O 2*p* and V 3*d*. In the formation of VO_2, vanadium's outer shell electron (V 3*d*) will fill up the 2*p* orbit of oxygen (O 2*p*), which was in insufficient states, thus give the VO_2's band structure as shown in Fig. 1-3, where hybridization by the O 2*p* affects the energy level of the components of V 3*d*, correspondingly. Considering this matter, in order to characterize the VO_2 valence band, characterization on the V 3*d* spectra was carried out. Characterization of the V 3*d* in the UPS spectra gives information between the top of the valence band and the Fermi level (E_F) in the VO_2's band structure.

Fig. 2-23 presents temperature dependence of V 3*d* spectra near the Fermi level (E_F) of films deposited at 20 and 40 W measured at different temperatures of 27ºC, 57ºC, 67ºC, and 107ºC, where insets show the enlarged figures of the V 3*d* spectra near the E_F within the binding energy from -0.2 to 1.0 eV. Measured V 3*d* spectra (marked in red and green for films of 20 and 40 W) were fitted by using Gaussian functions and was indicated by dashed lines in the spectra.

In the case of the film deposited at 20 W, as one can be observed in the fitted narrow curve at 27ºC, the V 3*d* band was observed to have its peak at 1.52 eV, and there is no significant changes observed as the temperature increases until 57ºC. Then, as temperature increases to 67ºC, the increase of signal below the E_F was observed (hatched area in red). The appearance of this signal, which its edges moved beyond the E_F suggests the VO_2 band gap closing, with respect to the insulator-metal transition that occurs. Further increasing in the temperature to 107ºC was observed to cause the increasing of the signal below E_F. This clear band gap closing of VO_2 films was the first to be observed through this work, suggesting excellent crystalline properties of the VO_2 film deposited with the substrate biasing power of 20 W.[96]

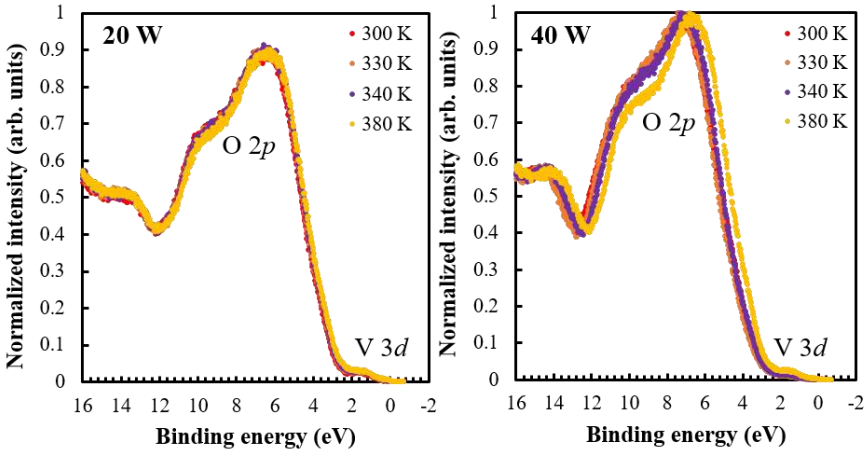

Fig. 2-22 Normalized wide scan UPS spectra of films deposited with the substrate biasing power of 20 and 40 W.

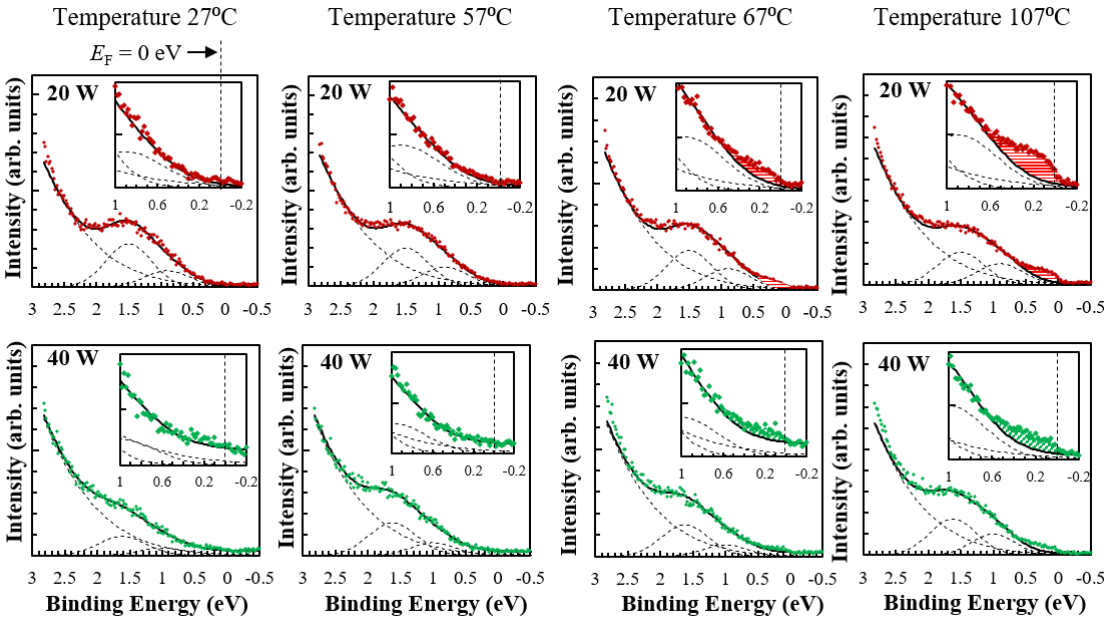

Fig. 2-23 Valence band spectra of films deposited at 20 and 40 W measured at four different temperatures of 27ºC, 57ºC, 67ºC, and 107ºC. Reproduced from [ref. 96 of J. Appl. Phys. **119**, 55308 (2016)], with the permission of AIP Publishing.

In contrast, film of 40 W was observed to have its V 3*d* peak at a rather low energy of 1.62 eV compared to the one observed in the film of 20 W at 27ºC. In spectra measured at 57ºC, although the signal was relatively small, the increasement of signal below the E_F was observed, suggesting rather early occurrence of the SPT on film deposited at 40 W. This was in agreement with the early transition behavior that was observed in the IMT and SPT properties given in the

previous sections, where the transition observed to be almost completed at around 60ºC. As the temperature later increases to 67ºC and 107ºC, the increasing in the area of the signal with its edges moved beyond the E_F (hatched in green area) were clearly observed. These results of proposed clear signal of the band gap closing on both films of 20 and 40 W, suggesting metallic state are entirely established at the high-temperature. The opening gap between valence band top and E_F at 27ºC and the gap closing observed at almost 60ºC, and 67ºC on films of 40 W, and 20 W fully supports the transition modifications in the VO_2 films deposited by the rf substrate biasing.

One should note that an intense Gaussian fitted peak with center at around 0.85–0.95eV below E_F was observed in both films deposited at 20 and 40W at all temperature. The increasing of the weight of this peak was in totally metallic state for films of 20W at 107ºC. As on film of 40W, an increase of this peak was obvious from a temperature higher than 67ºC. Biermann *et al.* in their theoretical calculations suggested the presence of this narrow d_{II} band at 0.8 eV in the VO_2 M1 phase.[47] They noted that this peak should be interpreted as a quasiparticle, which included electron correlation effect, rather than an incoherent lower Hubbard band (LHB). In this work, strengthening of this peak might with the increasing of temperature is interpreted to be due to the correlations of the electrons from the d_{II} orbitals, which form straight chains along the c_R-axis.

2.3.7 High TCR Value and Activation Energy in VO_2 Films Deposited with High-energy Ion Irradiation

The introduction of substrate biasing during reactive sputtering succeeded in modifying the IMT and SPT properties with significant transition temperature (T_t) shift towards lower temperature was observed. Together with these modifications of the T_t, remarkable modification in the TCR values was also obtained. As mentioned before, VO_2 was considered as a suitable candidate for the uncooled bolometers, due to its high TCR values at room temperature. In the present, TCR value of the VO_2-based bolometers is -2 %ºC^{-1}.[6,97]

Temperature coefficient of resistance (TCR) is a change in the resistance of the material with the change of temperature (1ºC) and can be defined as

$$\text{TCR} = \frac{1}{R}\frac{dR}{dT} \quad \ldots(2\text{-}3)$$

where, R is the material's sheet resistance, and T is the temperature. The temperature-dependent resistance curve (R-T characteristics) could be fitted to the Arrhenius relation of

$$\sigma = \sigma_0 \exp\left(-\frac{E_a}{kT}\right) \quad \ldots(2\text{-}4)$$

where, k is the Boltzman constant, and E_a is the activation energy. This equation, in which the E_a is involved, implies that the conduction is a thermally activated process. E_a is derived from a straight-line fitting of the Arrhenius plot. Satisfying the Eq. (2-3) and (2-4), the relation between the TCR and the E_a is defined as follow.

$$\text{TCR} = -\frac{E_a}{kT^2} \quad \ldots(2\text{-}5)$$

From this equation, one can define; the increasing of the TCR value will also significantly increase the activation energy (E_a). In this section, the increasing of the TCR value with significant increasing of the E_a in the VO_2 films deposited by the substrate biasing will be presented.

Figure 2-24 shows the R/R_{RT} versus temperature characteristics for films of 20 W and 40 W, whereas the slope of the R/R_{RT} *vs.* temperature characteristics defines the TCR value at room temperature. As one can observe, in comparison to that of film deposited at 20 W, rather steep slope was observed for film deposited at 40 W, signifying the increasing of the TCR values at room temperature with the increasing of substrate biasing power. From the slope of the R/R_{RT} *vs.* temperature characteristics, the TCR value for the films deposited at 20 and 40 W is calculated to be -1.5 %ºC^{-1} and -3.3 %ºC^{-1}, respectively. The changes in the absolute value of the TCR in films of 0, 10, 20, 30, and 40 W are plotted in Fig. 2-26.

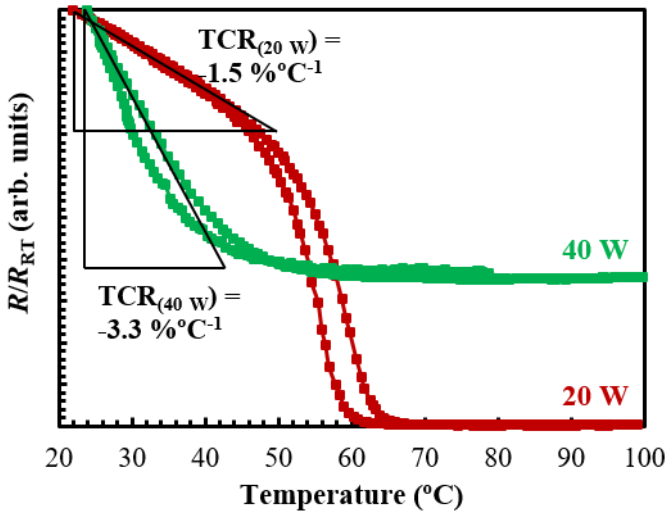

Fig. 2-24 R/R_{RT} vs. temperature characteristics for films of 20 and 40 W.

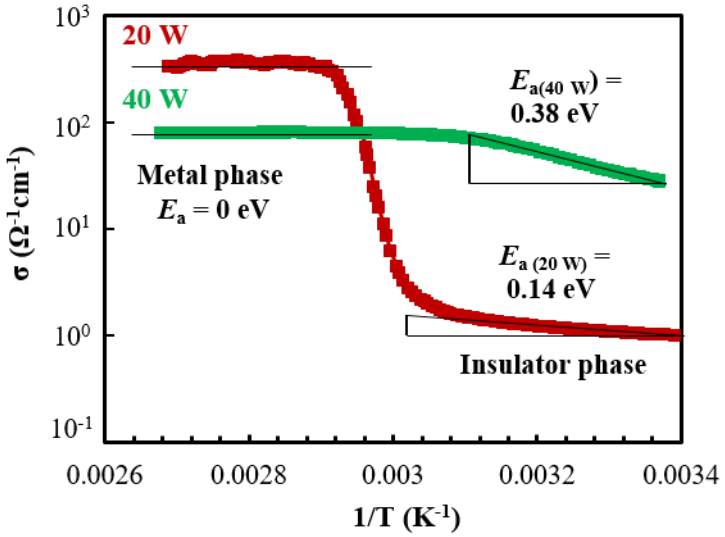

Fig. 2-25 Arrhenius plot of σ-1/*T* characteristics for films deposited at 20 and 40 W.

As described before, the increasing of the TCR value is also signifying the increasing of the activation energy. The activation energy (E_a) is defined by applying the Arrhenius equation to the ρ-T characteristics, which thus give an Arrhenius plot of σ-1/T characteristics, whereas the slope of the Arrhenius plot defines the activation energy value. Figure 2-25 shows the Arrhenius plot (for the heating runs) of films deposited at 20 and 40 W. In the case of VO_2, where the IMT occurs, the activation energy for both low- and high-temperature were calculated, giving activation energy for both insulator and metal phase. For the insulator phase, as one can observe, in comparison to the E_a calculated for film of 20 W (0.14 eV), film deposited at 40 W shows rather higher E_a of 0.38 eV, respectively. Significant to the occurrence of IMT, E_a value for the metal

phase calculated for both films of 20 W and 40 W is 0 eV, supporting the completion of IMT and the metallic behavior of the VO_2 films deposited by substrate biasing at high temperature. The changes of the E_a value for insulator phase in films of 0 to 40 W are plotted in Fig. 2-19.

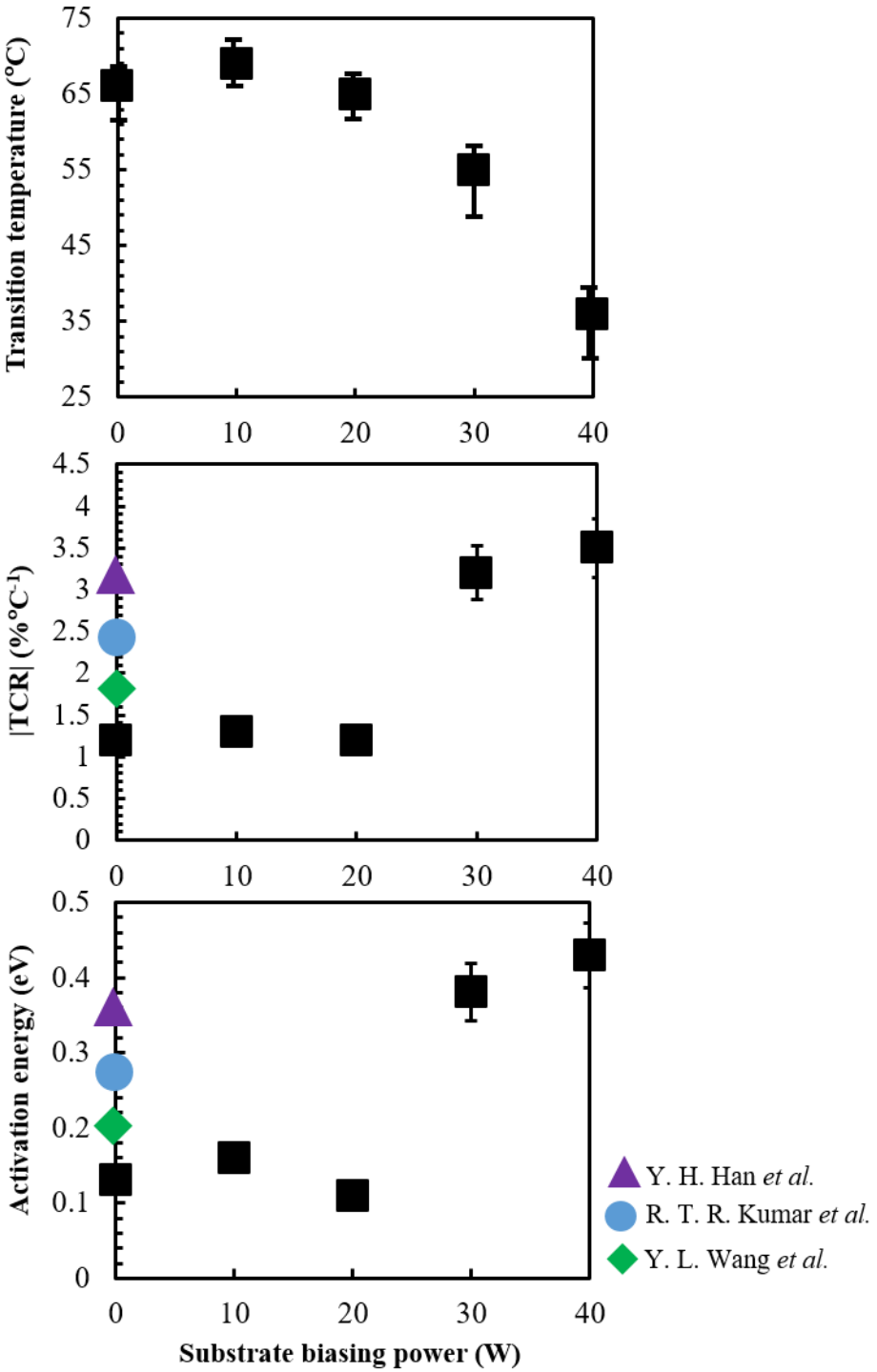

Fig. 2-26 Relation between the transition temperature, TCR value, and activation energy as a function of substrate biasing power. Reproduced from [ref. 92 of J. Appl. Phys. **117**, 185307 (2015)], with the permission of AIP Publishing.

Figure 2-26 presents the relationship between the transition temperatures (T_t), |TCR| value, and activation energy (E_a) of the sputtered VO_2 films in function of substrate biasing power. One can understand, by lowering of the T_t in the films deposited at 30 and 40 W, significant increase in the |TCR| and E_a values were observed, respectively. Corresponding to the small modifications of the T_t in the films deposited at 0, 10, and 20 W, no significant |TCR| value changes were observed, where low |TCR| values of around 1.3 $\%^oC^{-1}$ were obtained. In agreement with that insignificant changes in the |TCR| value of films deposited at 0, 10, and 20 W, almost similar E_a value of about 0.15 eV was observed for the films of 0, 10, and 20 W, correspondingly. Signifying an extensive decrease of the T_t in the films of 30 and 40 W, the increasing of the |TCR| values to be at around 3.5 $\%^oC^{-1}$ were observed in both films of 30 and 40 W, correspondingly. Also, as one can observe, the E_a correspondingly increases to almost 0.38 eV in both films of 30 and 40 W. These increased |TCR| values and E_a of the insulator phase in the films deposited at 30 and 40 W are comparable to those previously reported TCR values for doped VO_2 films,[6] pulsed-laser-deposited VO_2 films,[97] and post-annealed VO_2 films,[98] respectively.

2.4 Conclusions

In this chapter, rf magnetron reactive sputtering with the rf substrate biasing method and its effect on the sputtered VO_2 films on Al_2O_3 (001) substrates were introduced.

An installation of the V plate on the heater and the matching circuit equipped with the blocking condenser enabled the rf substrate biasing to be applied and the introduction of negative self-bias voltage ($-V_{dc}$) at the substrate. This method was observed to be succeed in enabling the ability to control of the ion irradiation energy during sputtering. By varying the substrate biasing power at 0, 10, 20, 30, and 40 W, $-V_{dc}$ with values of 0, 110, 170, 200, and 270 V was introduced at the substrate. As results, increasing of the ion irradiation energy to 30, 140, 200, 230, and 300 eV were achieved, correspondingly.

XRD and SAED measurements were performed to examine the crystalline properties of the sputtered VO_2 films. The appearance of VO_2 peaks of $(020)_{M1}$ and $(040)_{M1}$ at around $2\theta = 39.85°$ and $2\theta = 86.85°$ suggests an out-of-plane b_M-axis orientation growth of the VO_2 films deposited by rf substrate biasing. Despite the high-energy ion irradiation, the growth of the VO_2 films with b_M-axis orientation on Al_2O_3 (001) substrates were well-preserved even in the film deposited at 40 W. This well-preserved crystalline property for film of 40 W was discussed regarding its in-plane phi-scan XRD profile, confirming the VO_2 films grow on Al_2O_3 (001) substrates with an epitaxial relation of VO_2 $(010)_{M1}$ $[100]_{M1}$ ‖ Al_2O_3 (001) [100], [100], $[\bar{1}\bar{1}0]$. Also, the diffraction observed in SAED image revealed the typical growth pattern of VO_2 $(020)_{M1}$ on Al_2O_3 (001) substrates for both films, supporting the results of that the epitaxial relations were preserved even in the film deposited with high energy ion irradiation.

Morphologies of the VO_2 films deposited by the substrate biasing were examined by performing surface and cross-sectional view of FE-SEM measurements. VO_2 grains size decreased with the increasing substrate biasing power. However, it should be noted that the grains size once increases to rather larger size in the film deposited at 10 W, where VO_2 nanograins with an average size of 150 nm together with the unusual μm-sized crystalline grains were observed. Then, grains densification occurred, resulting in smaller crystalline grains with a rather smoother surface on films deposited at 20 W. Further increasement of the substrate biasing power led to an appearance of such hole-like features, expected due to the re-sputtering that occurs due to the high $-V_{dc}$ that achieved. Thus, as a result by increasing the ion irradiation energy during sputtering, the film thickness significantly decreases with the increasing of substrate biasing power, suggesting the decreasing and increasing of the deposition rate and sputter rate.

The occurrences of IMT and SPT in the sputtered VO_2 films were studied by performing ρ-T characteristics and temperature-dependent Raman scattering measurements. As the substrate biasing power increases to 20 W, signifying the improvement of the crystalline properties of the film deposited at 20 W, sharp transition properties with an improvement in metallic phase were observed, where a significant increase in the resistivity with the increasing of temperature was observed. By introducing rf substrate biasing, high energy ion irradiation during deposition was achieved and results in the modifications of the transition temperature (T_{IMT}). T_{IMT} was observed to once increased to the higher side, then turned to shift towards lower side, recording lowest T_{IMT} of 36ºC at the high biasing power of 40 W.

Temperature-dependent Raman spectra revealed the growth of VO_2 M1 phase at 27ºC on films deposited at 0, 10, 20, and 30 W. In comparison, at 27ºC, apparent decrease of the VO_2 M1 peak mode was observed, signifying an early occurrence of SPT on film deposited at 40 W. SPT's transition temperature (T_{SPT}) was determined and observed to have a similar modifications pattern with the T_{IMT}, thus evidenced by lowering of the transition temperature (T_t) in the sputtered VO_2 films due to the high-energy ion irradiation. This resulting towards the T_t modifications of the VO_2 films triggered by high-energy ion irradiation during the substrate biasing should be notified considering the well-preserved transition ratio and hysteresis behavior in the IMT properties, without no changes in the deposition conditions needed. The same T_t modifications pattern was also observed to occur in the IR transmittance properties, which expected to broaden VO_2 for optical applications, such as smart windows. Signifying an extensive decrease of the T_t in the films of 30 and 40 W, the increasing of the TCR values to be at around -3.5 %ºC^{-1} was observed in both films of 30 and 40 W, correspondingly. Also, as one can observe, the E_a correspondingly increases to almost 0.38 eV in both films of 30 and 40 W.

Temperature-dependent UPS measurement was performed to study the behavior of the valence band near the Fermi level, E_F. Measurements were performed for films with excellent crystalline properties and with the most extensive T_t shift prepared at 20 and 40 W, respectively. The opening gap between valence band top and E_F at 27ºC and the gap closing observed at almost 60ºC, and 67ºC on films of 40 W, and 20 W fully supported the transition modifications in the VO_2 films deposited by the rf substrate biasing. These results proposed clear signal of the band gap closing on both films of 20 and 40 W, suggesting metallic state are entirely established at the high-temperature.

Chapter 3

Mechanisms of the Transition Temperature Modifications Triggered by the Substrate Biasing

Chapter 3 Mechanisms of the Transition Temperature Modifications Triggered by the Substrate Biasing

3.1 Introduction

Chapter 2 reveals systematic modifications of the transition temperature (T_t) in VO_2 films deposited by substrate biased reactive sputtering. The effect of this method on modifying the T_t indicates that the increasing of the ion irradiation energy strongly determines the growth aspects of the VO_2 films on Al_2O_3 (001) substrates. In significant with increasing of the substrate biasing power, modifications of the IMT and SPT were observed, where both the T_{IMT} and T_{SPT} were found to be in perfect agreement with each other, evidencing lowering of the T_t in the sputtered VO_2 films due to the high-energy ion irradiation. As introduced before, the works on modifying the T_t of VO_2 have been performed for years, by using a variety of methods. Due to that matter, to verify comparability of the T_t values obtained in the present work, a summary on the modified T_t obtained by epitaxial stress controlled, and doping methods were plotted together with the T_t achieved in the films deposited by reactive sputtering with the substrate biasing.

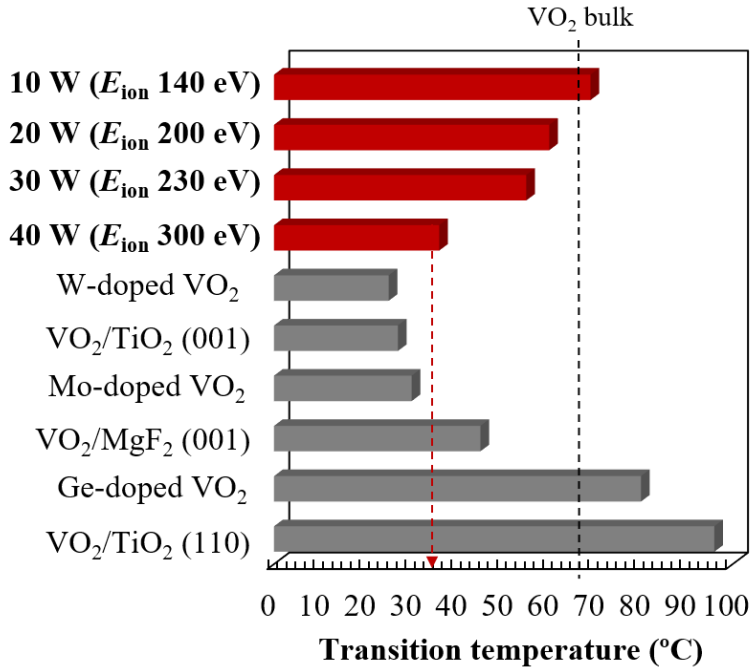

Fig. 3-1 Transition temperature obtained in the present work, in comparison to other reported values.

Figure 3-1 shows the T_t values observed by doping[15,80,81] and epitaxial-stress controlled[16,69] methods, as compared to the T_t values obtained in the present study as results of varying the ion irradiation during sputtering. As one can observe, increasing of ion energy to 140, 200, 230, and 300 eV with the substrate biasing power of 10, 20, 30, and 40 W resulted in modifying the T_t to

69, 65, 55, and 36ºC, respectively. Modifications of the T_t to near room temperature observed on film of 40 W remarks efficiency of this method. Furthermore, controllability of the T_t achieved by this rf substrate biasing method does not acquired any deposition condition changes. Apart from that, unlike other methods, one should be notified that the transition of about two order-of-magnitude and the hysteresis properties were able to be preserved.

In this chapter, the mechanism behind the T_t modifications in the VO_2 films deposited by reactive sputtering with substrate biasing will be discussed. Analytical methods for estimating in-plane stress and measuring the in-plane a_M-axis length will be given in section 3.2. Changes in the in-plane stress will first be discussed in section 3.3.1. In corresponding to the change of the out-of-plane axis observed from XRD pattern analysis, VO_2 films' behavior agreeing the theory of elasticity will be given by TEM analysis in section 3.3.2. In respect to the extensive decrease of the T_t, shortening of the in-plane a_M- axes length and the V–V pair distance will be introduced in sections 3.3.3 and 3.3.4. As high-energy ion irradiation was utilized during the depositions, the introduction of oxygen vacancies is undeniable. Thus, in section 3.3.5, the oxygen vacancies states in the sputtered VO_2 films will then be given. Later, in section 3.3.6, mechanisms behind the T_t modifications in the VO_2 films deposited by reactive sputtering with substrate biasing will be discussed by considering both in-plane $a_M/2$ lattice length and contribution of the oxygen vacancies. Considering those mechanisms, consideration on the T_t modifications in films thicker than 100 nm will be delivered. In the last section, section 3.4, conclusions on modifications of the T_t triggered by increasing of the ion energy irradiation during sputtering will be given.

3.2 Analytical Methods

3.2.1 Analysis on the In-plane Thin Film Stress

Stress in thin films known to arise from certain factors, including the lattice matching and thermal expansion coefficient different between film and substrate. Accordingly, factors such as low- and high-energy ion irradiation could also modify the stress states in thin films.[83,99] Considering the high-energy ion irradiation that is responsible for the growth and transition properties of the VO_2 films in the present work, stress becomes an important factor that needs to be analyzed. As known, film stress (σ) is related to the film strain (ε) by Hooke's law of

$$\sigma = E\varepsilon \qquad \ldots (3\text{-}1)$$

where, E is the Young's modulus of elasticity.

Young's modulus is a measure of the ability of the material is going to elongate or compressed under certain stress states. There are several Young's modulus values reported for VO_2; 200 GPa[100], 140-155 GPa[101], and 240-260 GPa[102]. Rúa *et al.* proposed that the Young's modulus obtained in particular experiments depend on film microstructure and orientation, and directions of extension or contraction provoked during the measurements, which thus result in variations of the value.[35] In this work, widely accepted Young's modulus value for VO_2 thin films of 200 GPa is used.

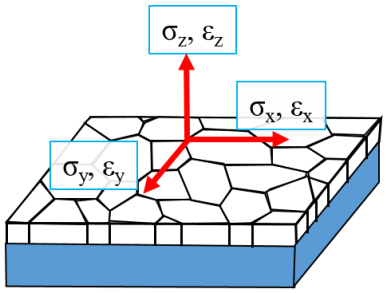

Fig. 3-2 Schematic diagram of stress (σ) and strain (ε) in thin films.

Accordingly, stress and strain in thin films in each axis of *x*-, *y*-, and *z*-axes are written as σ_x and ε_x, σ_y and ε_y, and σ_z and ε_z (shown in Fig. 3-2). The thin film is considered to load biaxially. Thus, in the case of thin films, an assumption of there will be no normal or shear stresses in the direction perpendicular to the film surface ($\sigma_z = 0$) is proposed. Due to this matter, stress and strain relation along the in-plane *x*- and *y*-axes, and the out-of-plane *z*-axis could be written as follow.

$$E\varepsilon_x = \sigma_x - \nu\sigma_y \qquad \ldots (3\text{-}2)$$

$$E\varepsilon_y = \sigma_y - \nu\sigma_x \qquad \ldots (3\text{-}3)$$

$$E\varepsilon_z = -\nu\,(\sigma_x + \sigma_y) \qquad \ldots (3\text{-}4)$$

where, for the stress calculation along the out-of-plane *z*-axis, the ratio of the relative transverse strain normal to the applied load is considered, and that so-called Poisson's ratio (ν) is introduced. Boulle *et al.* performed a calculation of the Poisson's ratio corresponding to the (010) orientation of the VO_2, thus give $\nu = 0.372$.[103] By considering the in-plane stress during the growth process is isotropic ($\sigma_x = \sigma_y = \sigma$), Eq. (3-4) could later be written as

$$E\varepsilon_z = -\nu(\sigma_x + \sigma_y) = -2\nu\sigma \quad \ldots (3\text{-}5)$$

, later gives Eq. (3-6) of

$$\text{In-plane stress, } \sigma = -\frac{E}{2\nu}\varepsilon_z \quad \ldots (3\text{-}6)$$

In the case of VO_2 films grow on Al_2O_3 (001) substrates, where the crystal grains grow with an orientation of (010) in the out-of-plane direction, difference in the *d*-spacing crystallographic of (020) plane ($d_{(020)}$) obtained from the XRD analysis could be used to determine the in-plane stress, gives by Eq. (3-7) of

$$\text{In-plane stress, } \sigma = -\frac{E}{2\upsilon}\left(\frac{d_{(020)} - d_0}{d_0}\right) \quad \ldots (3\text{-}7)$$

where, the $d_{(020)}$ could be obtained by using the Bragg's law in the form of

$$d_{(020)} = \frac{n\lambda}{2\sin\theta} \quad \ldots (3\text{-}8)$$

where, λ is a wavelength (λ= 1.5418 Å, mainly used in this work) and θ is the angle of diffraction.

From the above relation, the in-plane tensile ($\sigma > 0$) and compressive ($\sigma < 0$) stresses are affecting the result in the shortening and lengthening of the out-of-plane lattice length. Figure 3-3 shows a schematic diagram for oriented VO_2 films grow on Al_2O_3 (001) substrates, where the out-of-plane and the in-plane axes refer to b_M-axis, and a_M- and c_M-axes, respectively. The in-plane compressive stress ($\sigma < 0$) gives a significant shortening of the in-plane a_M-axis (= $2c_R$) and lengthening of the out-of-plane b_M-axis of VO_2 films, respectively.

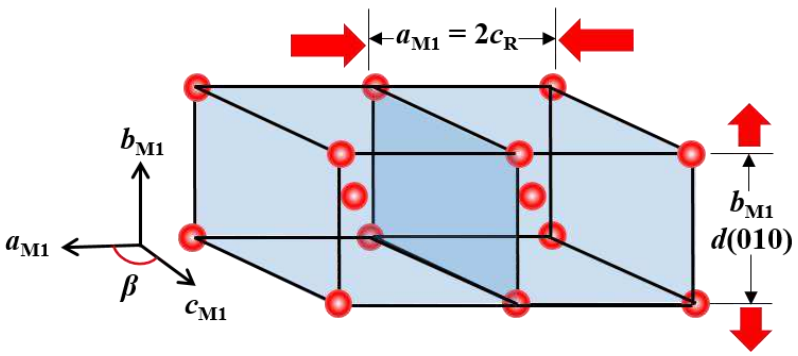

Fig. 3-3 Schematic diagram of VO_2 grow on Al_2O_3 (001) as in-plane compressive stress is taking place.

3.2.2 Analysis on the In-plane a_M-Axis Length by Asymmetrical XRD Measurement

Analysis on the in-plane a_M-axis length was conducted to study the mechanisms behind the transition temperature (T_t) modifications triggered by the substrate bias sputtering, as the T_t of VO_2 was directly related to the a_M (c_R)-axis. To examine the in-plane a_M-axis lattice parameter length, asymmetrical XRD analysis of lattice parameter measurements at the room temperature was performed. Four lattice parameters of the low-temperature monoclinic VO_2 phase were derived from the basis of the relationship between lattice distance and lattice parameters with a specified Miller index for a monoclinic crystalline structure.[67] Relationship between lattice distance ($d_{(hkl)}$) and lattice parameters *(hkl)* for a monoclinic crystal is given as below.

$$\frac{1}{d_{(hkl)}{}^2} = \frac{1}{sin^2\beta}\left(\frac{h^2}{a^2} + \frac{k^2 sin^2\beta}{b^2} + \frac{l^2}{c^2} - \frac{2hl\,cos\beta}{ac}\right) \quad \ldots (3\text{-}9)$$

Diffractions from four lattice distances, d_1 (020), d_2 (022), d_3 (220), and d_4 ($\bar{2}11$) were used to derive the four lattice parameters a_M, b_M, c_M, and β. In-plane lattice parameter (a_M-axis) was calculated by solving three equations for d_2, d_3, and d_4. All four diffraction measurements were performed at specific inclined angles ϕ and rotated angles ψ. Diffraction measurements for d_1 (020), d_2 (022), d_3 (220), and d_4 ($\bar{2}11$) were performed for the films at positions of 2θ = 39.832º, 55.542º, 55.563º, and 37.030º with specific inclinations of ψ = 0º, 44.94º, 43.04º, and 57.56º, respectively. Schematic diagram of the asymmetrical XRD measurement is shown in Fig.3-4.

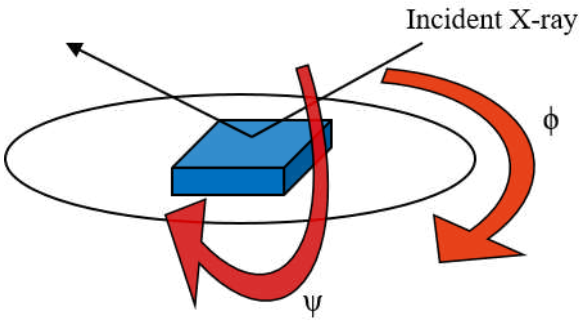

Fig. 3-4 Schematic diagram of the asymmetrical XRD analysis for lattice parameter measurement.

3.3 Results and Discussion

As elaborated in Chapter 2, rf substrate biasing method succeeded in shifting the T_t towards lower temperature. In the present work, the lowest T_t of 36ºC was achieved for the film deposited at 40 W. In this case of the T_t decreased to almost room temperature of the film deposited at 40 W, slight diminution in abruptness was observed. However, one should be notify, the transition of approximately 2-order of magnitude changes and 6ºC of hysteresis attributed to its first order IMT were still preserved.

In this chapter, the mechanism behind the T_t modifications in sputtered VO_2 films will be discussed considering the films of 0, 10, 20, 30, and 40 W, with the T_t of 66ºC, 69ºC, 65ºC, 55ºC, and 36ºC, where their IMT properties are shown in Fig. 3-5, respectively. However, regarding the film deposited without biasing (0 W), further discussion will be performed considering the VO_2 single-phase growth deposited with suppressed O_2 flow rate of 1.0 sccm (will later know as non-biasing film). As shown in the previous chapter, a film of without biasing deposited at O_2 flow rate of 2.5 sccm (0 W) was in a mixed growth states of VO_2 + V_6O_{13}. Hence, it was inappropriate to discuss the T_t of this film further. The ρ-T characteristic of this non-biasing film was shown in Fig. 2-2. Going through this chapter, the T_t modifications will be discussed as a function of the energy of ion irradiation, correspondingly.

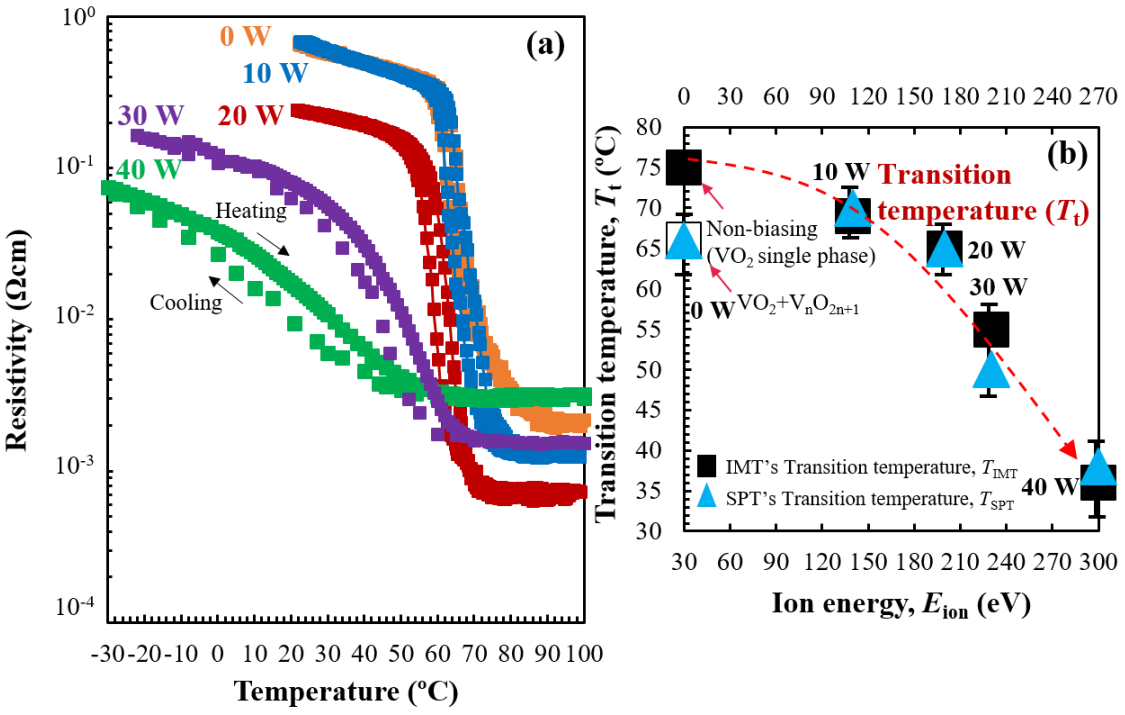

Fig. 3-5 (a) ρ-T characteristics for films of 0, 10, 20, 30, and 40 W. (b) The T_t modifications of sputtered VO_2 films with the increasing ion energy.

3.3.1 In-plane Stress Consideration of VO_2 Films Deposited by Reactive Sputtering with Substrate Biasing

Stress plays a major role in modifying the properties of thin films. It was reported that the epitaxial stress played a major role in inducing the T_t near room temperature in VO_2 films grow on TiO_2 (001) substrates.[104] Both VO_2 and TiO_2 with rutile-tetragonal structure have a small lattice mismatch at their a_R-axis. In comparison to the VO_2's a_R-axis ($a_{R(VO2)}$), TiO_2 has longer a_R-axis ($a_{R(TiO2)}$). The elongation of the in-plane $a_{R(VO2)}$-axis length significantly results in shortening of the out-of-plane VO_2's c_R-axis length, correspondingly. The shortening of the VO_2's c_R-axis length results in lowering of the T_t towards lower temperature, accordingly. In the present work of VO_2 films on Al_2O_3 (001) substrates, c_R (a_M)-axis lies in parallel to the substrate (in-plane a_M-axis). Hence, the in-plane stress is expected to play a major role in the IMT modifications triggered by the rf substrate biasing method.

According to the Eq. 3-7, $d_{(020)}$ could be used for determining the in-plane stress. Figure 3-6 (a) shows the shift in the position of the VO_2 (020) peak. The changes in the b_M-axis length ($2\times d_{(010)}$) in the VO_2 films deposited at 0, 10, 20, 30, and 40 W, at ion energy respectively of 30, 140, 200, 230, and 300 eV were shown in Fig. 3-6 (b). Dashed lines represent the bulk value of the $(020)_{M1}$'s 2θ value and the b_M-axis length. To accurately define the 2θ peak value, Gaussian fittings were performed to the XRD curves data of 2θ-θ scans in the range from 2θ = 38.35º to 41.35º. As ion energy increases with increasing substrate biasing power, VO_2 (020) peak was observed to shift towards a lower position. In agreement with that lower position of the 2θ peak, out-of-plane b_M-axis length was observed to be lengthened with the increasing of energy of ion irradiation, correspondingly.

Figure 3-7 shows the estimated in-plane stress (σ) of the VO_2 films on Al_2O_3 (001) substrates deposited by reactive sputtering with substrate biasing in function of ion energy calculated by using Eq. 3-7. In the case of the film deposited at 0 W, a slight low T_t in the film of 0 W is due to the low-quality crystalline structure of mixed VO_2 growth. Considering that matter, further discussion on the film of without biasing will be performed by taking the non-biasing film with single VO_2 phase (deposited in suppressed O_2 flow rate of 1.0 sccm) into account. The stress was of tensile state in films deposited with ion energies at 30 and 140 eV (0 W and 10 W) and then turned into the compressive state in films deposited at ion energy of and larger than 200 eV (20, 30, and 40 W). From these results, the increasing of substrate biasing power that results in a simultaneous increase in the ion irradiation energy was observed to lead to the change of the in-plane stress state in the VO_2 films, thus, change the out-of-plane lattice length of b_M-axis.

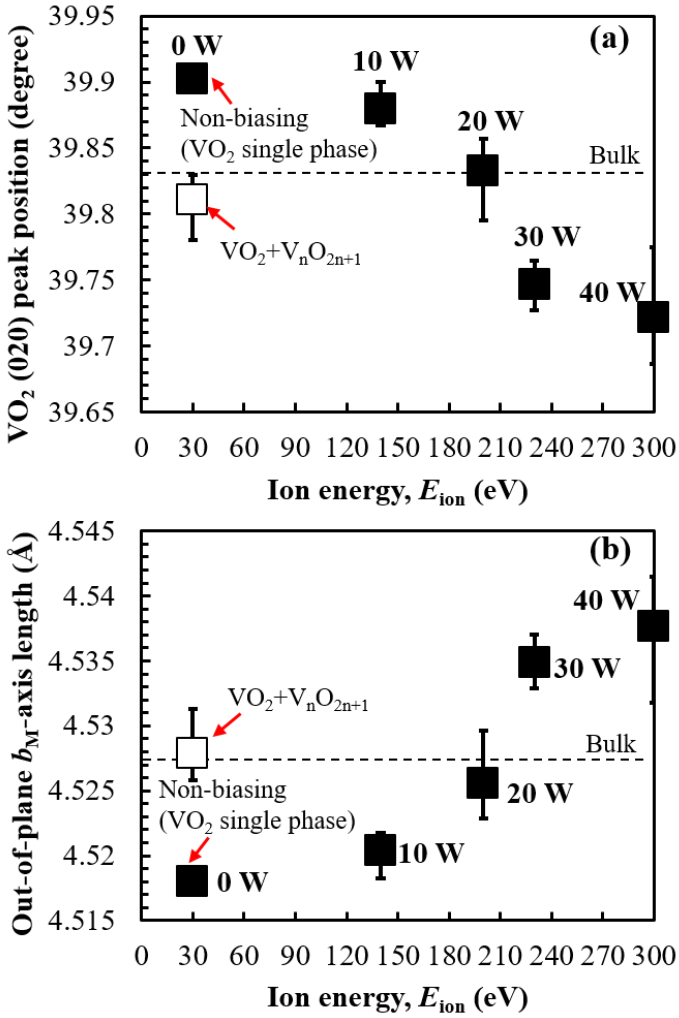

Fig. 3-6 Shift of (a) VO_2 (020) peak position and (b) calculated b_M-axis length of sputtered VO_2 films.

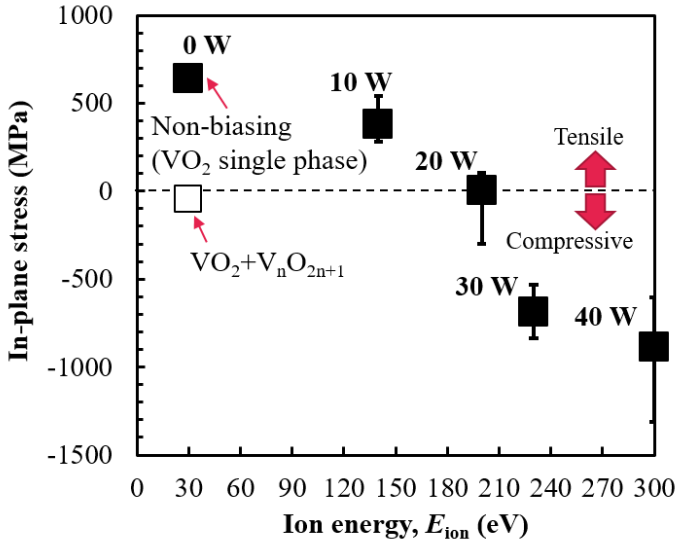

Fig. 3-7 In-plane stress estimation of VO_2 films plotted in functions of ion energy irradiation.

In the non-biasing film and film deposited at ion energy of 140 eV (10 W), tensile stress state was observed in agreement with compression of the out-of-plane b_M-axis length. In comparison to the stress induced by the ion irradiation energy during sputtering deposition (growth stress), rather larger thermal stress effect was expected to take place and results in the in-plane tensile stress in the non-biasing film and film of 10 W. High substrate temperature (T_S) of 400ºC utilized in the present work is responsible for the occurrence of the in-plane tensile stress, respectively. This so-called thermal stress occurs due to large difference in thermal expansion coefficients between film and substrate, given by equation as follow;

$$\sigma_{thermal} = E\Delta\alpha\Delta T \quad \ldots (3\text{-}10)$$

where, E is a Young's modulus, $\Delta\alpha$ is a difference between the thermal expansion coefficient, and ΔT is the temperature difference between substrate temperature and room temperature. Thermal expansion coefficients of VO_2 and Al_2O_3 are given in Table 3-1. From Eq. 3-10, in the present work of T_S = 400ºC (673 K), by considering E = 200 GPa, thermal stress ($\sigma_{thermal}$) is calculated to be 1600 MPa (tensile). From this matter, the compression stress introduced by the ion irradiation energy of around 140 eV achieved at the substrate biasing power of 10 W is still not enough to result in the in-plane stress evolution in the VO_2 films, thus gives tensile stress state even in the film deposited at 10 W.

Table 3-1 Thermal expansion coefficients of VO_2 films and Al_2O_3 substrates.[105]

Material	Thermal expansion coefficient ($^oC^{-1}$)	
	$\alpha_{//} \times 10^{-6}$	$\alpha_{\perp} \times 10^{-6}$
VO_2 (M1)	4.9	26
VO_2 (R)	26	4.9
Al_2O_3	5.3	4.5

In this work, a significant increase of the ions irradiation energy during deposition with continuous strikes of energetic particles was observed to change the microstructural properties, where simultaneous compaction of the lattice and a concomitant evolution of a denser microstructure as was introduced by surface view of the FE-SEM images. As the substrate biasing power increases, the compressive stress induced by the increasing of ion irradiation energy caused the in-plane tensile stress decreases as pores collapse and grains densification occurs by atomic displacement attributed to the energetic particles striking deeper into the film due to the occurrence of atomic peening. This so-called "atomic peening" was enhanced with increasing of

kinetic energy of the ions during sputtering. At this state, porosity decreases and the network becomes more interconnected. In such a compact but still somewhat porous network, short range interatomic forces across small defects takes place, thus results in the stress revolution from tensile to compressive.

In addition to the grains densification, incorporation of the Ar ion irradiation during the sputtering process is also expected to responsible for inducing compressive stress in VO_2 films deposited by substrate biasing reactive sputtering. In this work, depths analysis of XPS measurements was performed confirming an appearance of Ar 1*s* peak in the VO_2 films deposited by reactive sputtering with substrate biasing. Hoffman and Thornton reported that the compressive stress in sputtered films is correlated with the presence of Ar content trapped in the films.[106] Thus, it can be understood that incorporation of Ar atoms in inducing compressive stress in thin films is also a factor that should not be neglected.

Based on the theory of elasticity, compression (elongation) of the out-of-plane lattice length gives significant elongation (compression) of the in-plane lattice length. Consequently, tensile stress in the non-biasing film and film of 10 W that results in the shortening of the out-of-plane lattice length is supposed to give significant lengthening in the in-plane lattice length, correspondingly. In contrast, in-plane compressive stress in films deposited at 20, 30, and 40 W is expected to give significant compression in the in-plane lattice length, correspondingly. In the next section, observation on these out-of-plane and in-plane axes modifications triggered by the energetic ion irradiation will be delivered.

3.3.2 Transmission Electron Microscopy (TEM) Measurements for In-plane and Out-of-plane Lattice Length Analysis

XRD measurements revealed that the increasing of ion energy of and larger than 200 eV (≥ 20 W) resulted in the in-plane compressive stress and was observed to trigger the elongation of out-of-plane b_M-axis length. Based on the consideration of elasticity, significant shortening of the in-plane axis length would be expected to occur simultaneously. Transmission Electron Microscopy (TEM) measurements were performed to study significant changes in both out-of-plane and in-plane axes length with the increasing substrate biasing power.

Cross-sectional TEM images revealed strong evidence of the lattice length modifications and improved crystalline behavior with the increasing energy ion irradiation *via* the substrate biasing method. The measurement was performed for films deposited at 0, 10, 20, and 40 W. One should note that, in this section, in-plane axis modification of film deposited at 10 W will be discussed considering the TEM images taken at the nanograins region. The investigation of this film is remarkable considering the difference in-plane stress behavior (of tensile stress) that is expected to modify both out-of-plane and in-plane axes, correspondingly.

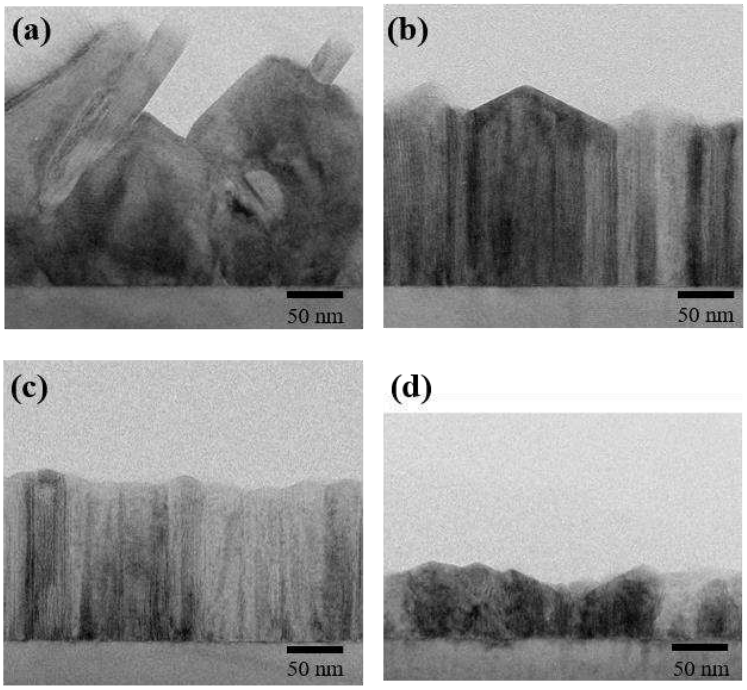

Fig. 3-8 Cross-sectional TEM images of films deposited at (a) 0 W, (b) 10 W, (c) 20 W, and (d) 40 W.

Figure 3-8 shows the cross-sectional TEM images for films of (a) 0 W, (b) 10 W, (c) 20 W, and (d) 40 W. In the film of 0 W, mixed structure and scattered crystalline properties were

observed. As the energy of ion irradiation increases together with the increasing substrate biasing power, fine VO_2 grains grown in columnar structure with a size of the width of several hundred nm was observed in the film deposited at 10 W (Fig. 3-8 (b)). As grains densification and peening effect occurs with increasing of the biasing power, decreasing of columnar structure's width from several hundred nm in the film of 10 W to several tens nm in the film of 20 W was observed. One can observe in Fig. 3-8 (c), a densely packed columnar grains structure of high crystalline properties of film deposited at 20 W. This densely packed columnar grains structure has significantly improved the IMT properties, where improvement in the transition sharpness with improved metallic properties was observed in film of 20 W. The microstructure from film of 10 to 20 W observed in this cross-sectional TEM images was in a well agreement with discussion on the in-plane stress evolution from tensile to compressive presented before. During deposition with high biasing power of 40 W, high-energy ion irradiation of around 300 eV was observed to interrupt the columnar growth of the VO_2 films, as the columnar structure was no longer observable in Fig. 3-8 (d). Limitation in surface migration due to the continuous bombardment of the energetic particles was expected to result in the decrease of crystal grains size.

Figure 3-9 shows high-resolution TEM images for films deposited at (a) 0 W, (b) 10 W, (c) 20 W, and (d) 40 W. These images were investigated to understand the lattice parameters changes that were expected to occur as the ion irradiation energy increases during the substrate biasing deposition. The TEM observation was performed in [120] direction ($[01\bar{1}0]$ in four index notation). Rectangular unit cells that are shown as an inset in Fig. 3-9 (a), (b), (c), and (d) represent one VO_2 unit cell, where the x- and y-axes are equivalent to the $c_M \sin\beta$ (a_{R1}) and b_M (a_{R2}) -axes, respectively. Figure 3-10 illustrates a schematic of VO_2 grows on Al_2O_3 (001) substrate on the TEM observation in [120] direction.

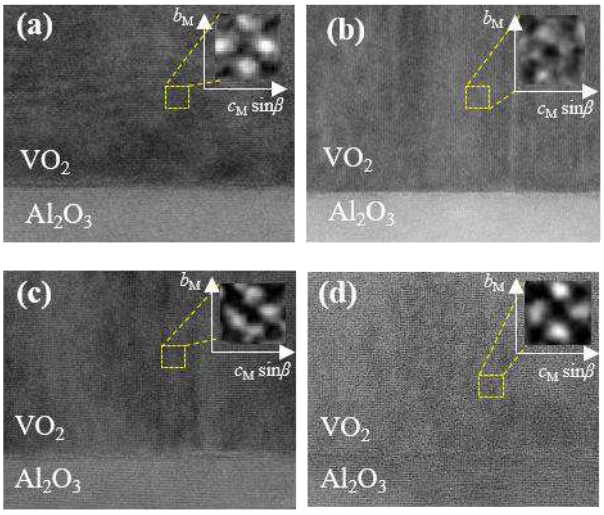

Fig. 3-9 High-resolution TEM images for films of (a) 0 W, (b) 10 W, (c) 20 W, and (d) 40 W.

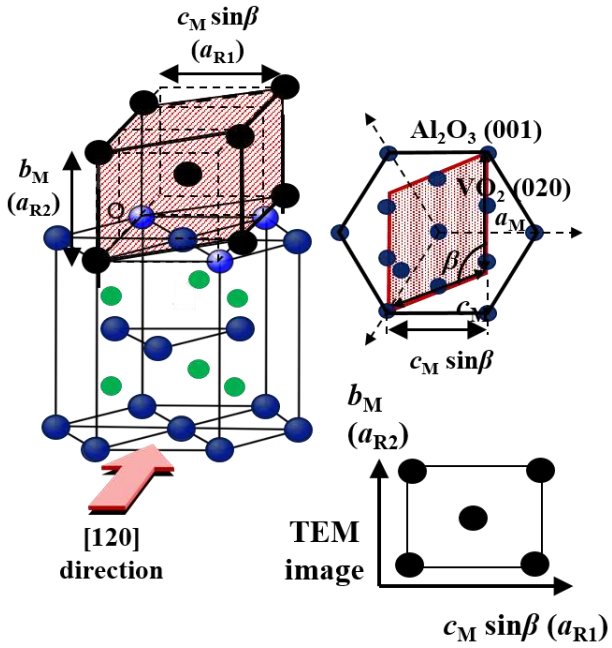

Fig. 3-10 Schematic of VO_2 grows on Al_2O_3 in respect to the TEM observation in [120] direction.

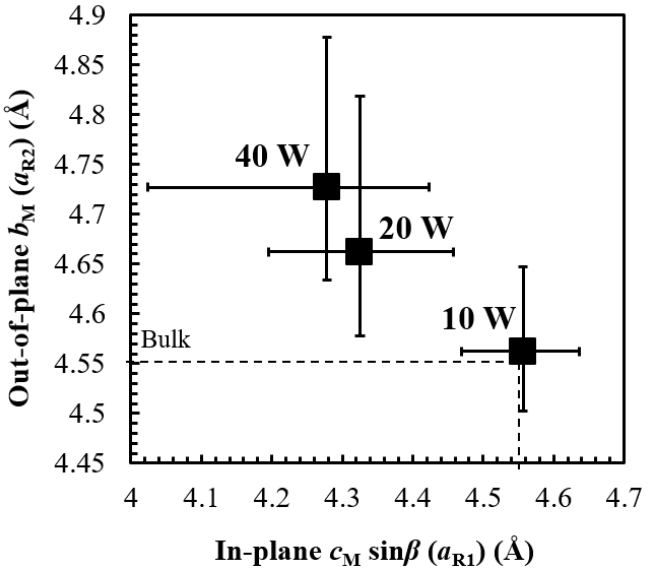

Fig. 3-11 Changes in both out-of-plane and in-plane lattice parameters of sputtered VO_2 films.

Figure 3-11 shows the lattice parameters of the out-of-plane b_M-axis and the in-plane $c_M \sin\beta$ -axis, measured at several spots on films deposited at different energy ion irradiation of 140, 200, and 300 eV of films deposited at 10, 20, and 40 W, respectively. In this calculation, the angle of β was considered constant at 122.6º. In agreement with the in-plane tensile stress observed in the film of 10 W, in comparison to the bulk, rather longer in-plane axis was observed with an average length of 4.556 Å. In significant to that elongation in the in-plane axis, rather shorter out-of-plane axis with an average length of 4.562 Å was observed.

As was proposed before, further increasement in the energy of ion irradiation to 200 and 300 eV at substrate biasing power to 20 and 40 W, shortened in-plane axis lattice length was observed with elongated out-of-plane lattice length. In comparison to the film of 10 W, rather shorter in-plane lattice length of 4.325 Å and 4.278 Å were observed in films of 20 W and 40 W. Accordingly, elongation of the out-of-plane lattice length was observed as the out-of-plane lattice length with average value of 4.662 Å and 4.727 Å were obtained in films of 20 and 40 W. From the above results, one can understand that agreeing the theory of elasticity, the in-plane tensile (compressive) stress works in the sputtered VO_2 films results in the elongation (compression) of the in-plane axis length, respectively. These observations support the hypothesis proposed before, where the in-plane compressive stress results in the shortening of the in-plane axis, respectively. However, this observation on shortening of the in-plane axis of $c_M \sin\beta$ was not enough to support the T_t modifications in the present work, as the T_t was modified according to its c_R (a_M)-axis. For further discussing modifications of the T_t in the present work, lattice length analysis on the in-plane a_M-axis is needed. Results on the analysis of the in-plane a_M-axis lattice parameter for sputtered VO_2 films will be given in the next section.

3.3.3 Asymmetrical XRD Measurements for In-plane a_M-axis Lattice Length

In the previous section, the increasing of substrate biasing power to larger than 20 W that results in increasing of the ion energy to larger than 200 eV was observed to result in the in-plane compressive stress and was observed to trigger elongation of the out-of-plane b_M-axis length and shortening of the in-plane $c_M \sin\beta$-axis length, respectively. However, for further discussion on the mechanisms behind the transition temperature (T_t) modifications triggered by the substrate biasing in the present work, analysis on the in-plane a_M-axis is needed. The a_M-axis length gives direct information on the V–V atoms distance, where the shortening of the a_M-axis and V–V atoms distance result in the early occurrence of IMT in the VO_2. Accordingly, the length of the a_M-axis is almost equal to two times of c_R-axis length. In this work, the modifications of the T_t will later be discussed in relation to the $a_M/2$ lattice length.

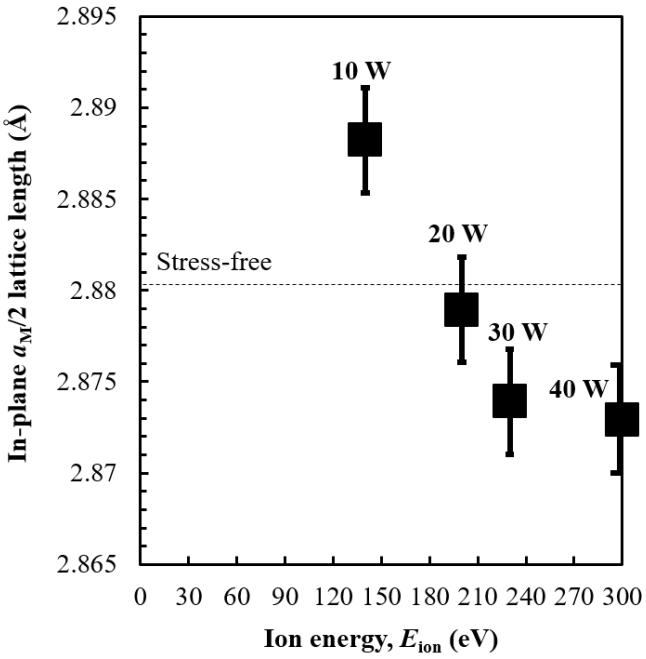

Fig. 3-12 In-plane $a_M/2$ lattice length in sputtered VO_2 films in function of ion energy.

Figure 3-12 shows the $a_M/2$ lattice length measured by the asymmetrical XRD measurements for films deposited with the substrate biasing power of 10, 20, 30, and 40 W, plotted in function of ion energy. In agreement with in-plane tensile stress observed in the film of 10 W, rather longer in-plane $a_M/2$ lattice length was observed with an average length of 2.888 Å. With later increasing in the energy of ion irradiation to 200 and 230 eV (increasing of substrate biasing power to 20 to 30 W), in-plane $a_M/2$ lattice length was observed to decrease in almost linear relationship to 2.879 Å and 2.874 Å. As substrate biasing power increases to 300 eV (at 40 W), $a_M/2$ lattice length was observed to shorten to 2.873 Å. However, different from the shortening of $a_M/2$ lattice length from

10 to 30 W, saturation behavior in shortening of the $a_M/2$ lattice length was observed. Despite saturation behavior in shortening of the $a_M/2$ lattice length, the increasing of ion energy from 140 eV (10 W) to 300 eV (40 W) results in the evolution of the in-plane stress state from tensile to compressive, where significant lengthening and shortening of $a_M/2$ lattice length were observed in films deposited at 10 W and 40 W. These observations revealed that modifications of the T_t triggered by the energetic ion irradiation in this substrate biasing reactive sputtering are resulted by the modifications of the $a_M/2$ lattice length, correspondingly. The in-plane compressive stress results in the shortening of the in-plane a_M-axis, hence give modifications of the T_t towards lower temperature, respectively.

3.3.4 Characterization on Raman Peak at 339 cm^{-1} for Determining Stress on the V–V Atoms Along the a_M-axis

As mentioned before, lattice parameter of the a_M-axis that lies in plane to the substrate plays a major role in controlling the transition temperature (T_t) in the VO_2 films. In the previous section, significant shortening of the in-plane a_M-axis lattice length in films deposited in high-energy ion irradiation was revealed. As the V atoms reside along the a_M-axis, shortening of the in-plane a_M-axis length was supposed to give similar behavior to that V–V atoms distance. Raman scattering is a phenomenon that sensitive to crystalline structure and stress. Raman measurement is one of the most convincing methods to characterize stress in the VO_2 films. In chapter 2, Raman spectra were discussed to investigate SPT in the sputtered VO_2 films. In this section, stress along the V atoms pair in the sputtered VO_2 films will be discussed concerning the behavior of the phonon mode in the Raman spectra.

Transition phase ratio *vs.* temperature characteristics shown in Fig. 2-19 (a) gives the information regarding the behavior of VO_2 at a certain temperature. The M1 ratio is equal to 1 (M1 ratio = 1) at 23ºC in films of 0, 10, 20, and 30 W. In contrast, M1 ratio is equal to 1 at rather lower temperature of -80ºC. The "M1 ratio = 1" is referred to the state where the SPT is still not yet begin. Accordingly, further evaluation of these spectra will give a significant information on the stress behavior of the V–V atoms. To fully understand the mechanisms behind the modified properties in films deposited by reactive sputtering with substrate biasing, Raman spectra whereas the M1 phase ratio is equal to one (M1 ratio = 1) are taken into account. Note that, Raman spectra for a film of 10 W illustrated in the figure below is taken from the nanograins region.

Figure 3-13 shows the Raman spectra of films deposited at 10, 20, 30, and 40 W, whereas the VO_2 M1 ratio is equal to 1. In all spectrum, 11 characteristic peaks of VO_2 M1 phase were observed at 132, 193, 224, 261, 310, 338, 386, 440, 498, 610, and 670 cm^{-1}. As one can observe, certain peaks in high-energy ion irradiated films of films deposited at 30 and 40 W (ion energy of around 230 and 300 eV) were shifted. These shifts suggested strong stress effect in the films of 30 and 40 W, in agreement with the strong in-plane compressive stress estimated from the strained out-of-plane b_M-axis length obtained from the XRD measurements presented before. However, for determining the behavior of the two V atoms that become a pair in the low-temperature M1 phase, the behavior of Raman peak at 339 cm^{-1} is taking for consideration.

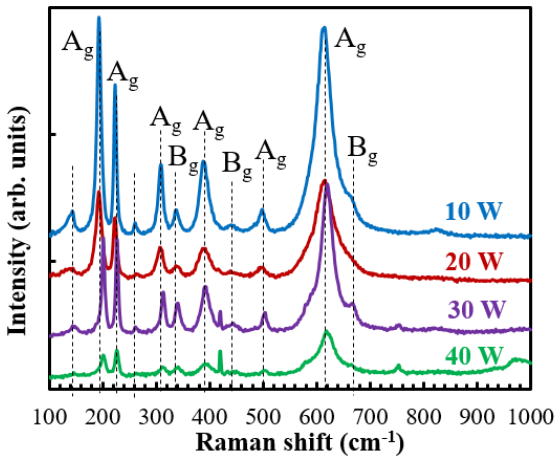

Fig. 3-13 Raman spectra for films of 10, 20, 30, and 40 W, whereas VO_2 M1 ratio is equal to 1.

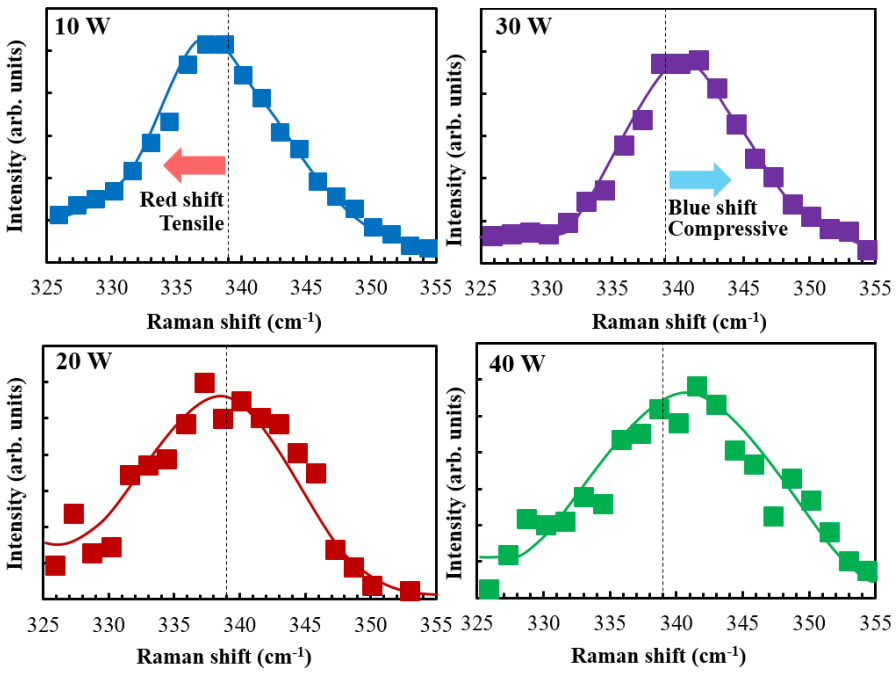

Fig. 3-14 Variation of Raman phonon mode of V–V binding at 339 cm^{-1} for films of 10, 20, 30, and 40 W.

Figure 3-14 shows the variations of Raman phonon mode of V–V binding at 339 cm^{-1} for films deposited at 10, 20, 30, and 40 W, respectively. V–V phonon mode of 339 cm^{-1} is taken into consideration, due to its vibration direction that is parallel to the a_M-axis, thus corresponding to the V–V stretching mode, respectively.[107,108] A clear red-shift behavior was observed on film of 10 W, suggested elongation of the V atoms pair due to the in-plane tensile stress on the V–V pair along the a_M-axis. As biasing power increases to 20 W, the peak shifted slightly to a higher position; blue-shift. Further increasement of substrate biasing power to 30 and 40 W results in an apparent blue shift suggesting compression of the V–V atoms distance, respectively. One can

observe, the shift value of the peak getting larger as the substrate biasing increases, where the film of 40 W was observed to be the most shifted one with an approximate shift of 2 cm^{-1}. The decreasing of the V–V atoms distance along the a_M-axis strengthened the V–V atoms pair, thus trigger an early occurrence of the SPT and IMT in VO_2. There observations of tensile (compressive) stress along the V–V atoms pair support the modifications of the T_t to high (low)-temperature, correspondingly.

3.3.5 X-ray Photoelectron Spectroscopy (XPS) Measurements for Oxygen Vacancies Characterization

The formation of oxygen vacancies in films deposited with high-energy ion irradiation is inevitable. Recently, 'defects engineering' became a commonly discussed topic, where controlling defects in VO_2 films reported to have a significant effect in controlling the transition behavior of VO_2 thin films.[109,110] Due to that matter, in order to clarify the mechanism behind the transition temperature (T_t) modifications in VO_2 films deposited by reactive sputtering with substrate biasing, where high-energy ion irradiation up to 300 eV was achieved during the deposition, analysis on the vacancies state is necessary. In this section, those vacancies state in the sputtered films were analyzed by X-ray Photoelectron Spectroscopy (XPS) and their effects on the IMT properties were discussed. Note that, this measurement was performed at room temperature.

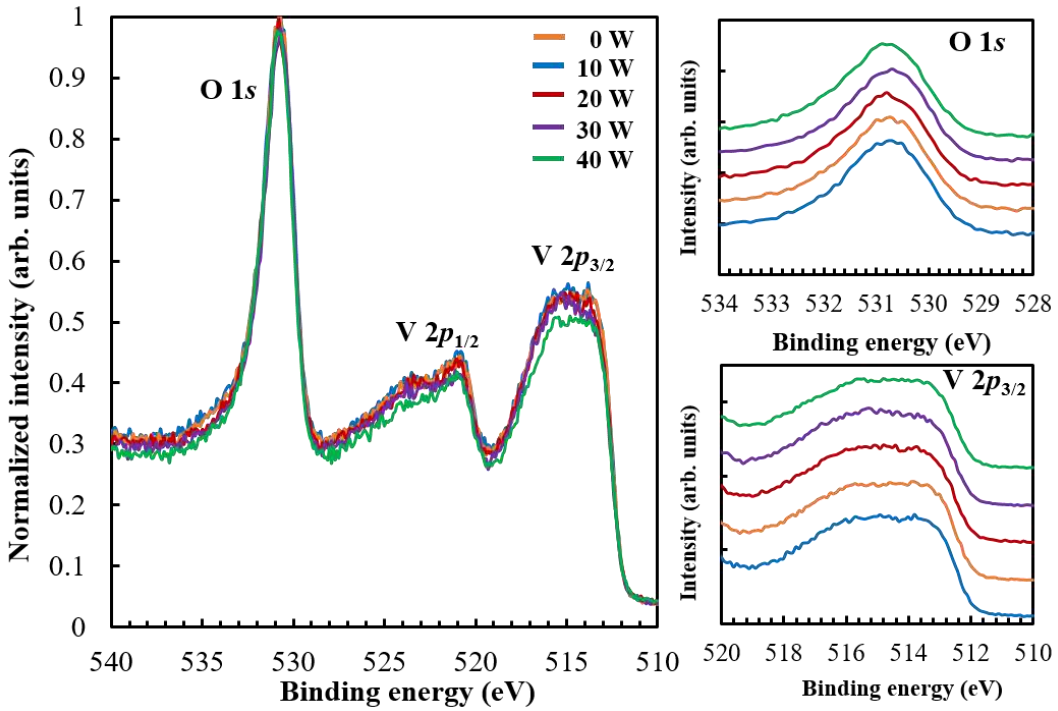

Fig. 3-15 Normalized wide XPS spectra of films deposited at 0, 10, 20, 30, and 40 W (a) with the narrow spectra taken for O 1*s* (b) and V $2p_{3/2}$ (c) spectra measured at room temperature.

Figure 3-15 (a) presents normalized wide XPS spectra of the sputtered VO_2 films, respectively deposited with the biasing power of 0, 10, 20, 30, and 40 W, where photoemission spectra are taken in the range of the binding energies consists of V $2p_{3/2}$, V $2p_{1/2}$, and O 1*s* spectra. Figure 3-15 (b) and (c) show the narrow spectra taken in the range of 528 to 534 eV and 510 to 520 eV of O 1*s* and V $2p_{3/2}$ spectra, respectively. In the films of 0, 10, 20, 30, and 40 W, diffracted peak of the O 1*s* was observed at 530.8 ± 0.1 eV. This position is consistent with other reported

O 1*s* spectra in VO_2 films.[111,112] In contrast to the sharp O 1*s* peak width, rather broader VO_2 characteristic peak of V $2p_{3/2}$ was observed. Blaauw *et al*., and Sawatzky and Post suggested that these broader peaks are characteristics of the narrow-band metals.[111,113] Hush suggested that this broad bandwidth of a mixed valence compound was due to the Coulomb interaction that takes place between the core hole and the valence electron.[114] As for VO_2 peak of V $2p_{3/2}$ spectra, slight shifts towards lower binding energy was observed as the biasing power increased. However, for further discussion regarding this shift in V $2p_{3/2}$, which is important in determining the vacancies state in VO_2 films. The spectra were fitted with partial Lorentzian and Gaussian line shapes and Shirley line shape for the background of the spectra, where Multipak software was utilized for fitting the spectra.

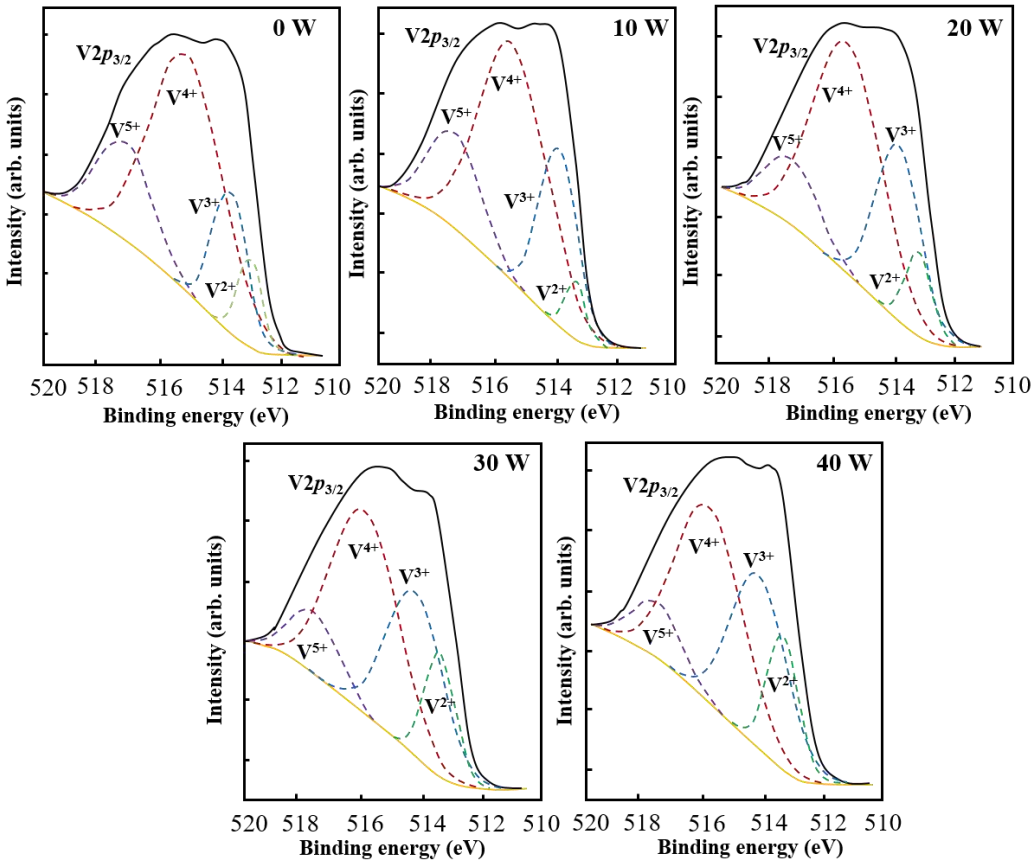

Fig. 3-16 High-resolution XPS spectra of V $2p_{3/2}$ for films deposited at 0, 10, 20, 30, and 40 W.

Figure 3-16 shows XPS spectra of V $2p_{3/2}$ signal in the binding energy range of 510-520 eV at the room temperature for films of 0, 10, 20, 30, and 40 W, while four fitted sub-peaks (dashed lines) of V $2p_{3/2}$ indicate that the sputtered VO_2 films possessed with multivalent states of V^{5+}, V^{4+}, V^{3+}, and V^{2+} at binding energy of 517.5 ± 0.3, 515.8 ± 0.3, 514.2 ± 0.4, and 513.2 ± 0.2 eV, respectively.[27] Defects population in the sputtered VO_2 films in the present work will be discussed considering its oxidation states area (%).

Film deposited without biasing (0 W) shows a rather higher ratio of V^{5+} of nearly 20% in agreement with its mixed growth state of VO_2 and the presence of high oxidation phases of V_2O_5 (V^{5+}) and V_6O_{13} (mix states of V^{5+} and V^{4+}) due to the excess oxygen flow rate during deposition (O_2 of 2.5 sccm). As the substrate biasing power applied, significant decrease of the V^{5+} area was observed, where only 17% of V^{5+} was observed in film of 10 W. As the substrate biasing power increases to 20 W, further decrease of V^{5+} area was observed, where only 12% of V^{5+} was seen in film deposited at 20 W. Furthermore, slight increase of V^{4+} in film of 20 W was also observed in comparison to the films deposited at 0 and 10 W, signifying the crystalline structure improvement with improved transition abruptness that observed.

Later, as the energy of ion irradiation increases to 230 and 300 eV with increasing substrate biasing power to 30 and 40 W, increasing of low oxidation states area of V^{2+} and V^{3+} were observed with significant decrease in high oxidation states area of V^{4+} and V^{5+}, respectively. Significant increase of the low oxidation states were observed in films deposited with substrate biasing power larger than 20 W (E_{ion} larger than 200 eV), where the high oxidation states area decreases from 69.8% (12.0% and 57.8% of V^{5+} and V^{4+}) in film of 20 W to 56.0% (10.1% and 45.9% of V^{5+} and V^{4+}) and 53.3% (9.4% and 44.0% of V^{5+} and V^{4+}) in films of 30 and 40 W, respectively. In respect to that decrease of the high oxidation states area, significant increasement of the low oxidation states were observed, where the low oxidation states area increases from 34.4% (26.9% and 7.6% of V^{4+} and V^{3+}) to 44.0% (30.9% and 13.1% of V^{4+} and V^{3+}) and 46.6% (32.5% and 14.1% of V^{4+} and V^{3+}) in films of 30 and 40 W, respectively. These changes of the high- and low- oxidation states in the films deposited by reactive sputtering with substrate biasing were summarized and shown in Fig. 3-17.

These results of increasement of the low oxidation states area in films deposited with ion energy of 230 and 300 eV at the biasing power of 30 and 40 W were observed to verify the increasing of the oxygen defects in the films. This relation between the introduction of oxygen defects and early IMT onset in high-biased films agrees well Goodenough's proposal, where the early IMT transition is introduced by the existence of extra electrons in the VO_2 films.[42] Oxygen defects are frequently discussed considering deposition with low oxygen flow rate of oxygen loss (O_O^x) state. The relation between oxygen defects and extra electrons could be expressed as below:

$$\boldsymbol{O_O^x \leftrightarrow V_O^{\cdot\cdot} + 2e' + \left(\frac{1}{2}\right) O_2} \qquad \text{…(3-11)}$$

From the above equation, one can understand that in order to maintain the stoichiometry, oxygen loss (O_O^x) will require the creation of oxygen vacancies ($V_O^{\cdot\cdot}$) in VO_2 films, whereas extra electrons

($2e'$) will be introduced and will be trapped at the V^{4+} octahedral sites, correspondingly. In order to study the increasing of free carrier concentration in the VO_2 films signifying the increase of oxygen vacancies, Hall Effect measurement of van der Pauw technique was performed.

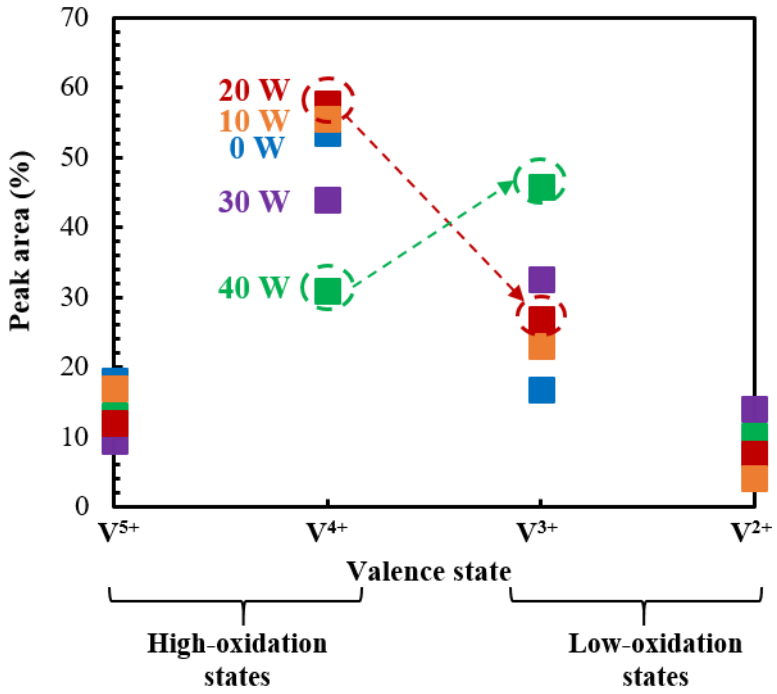

Fig. 3-17 Peak area of the valence band spectra of films deposited at 0, 10, 20, 30, and 40 W.

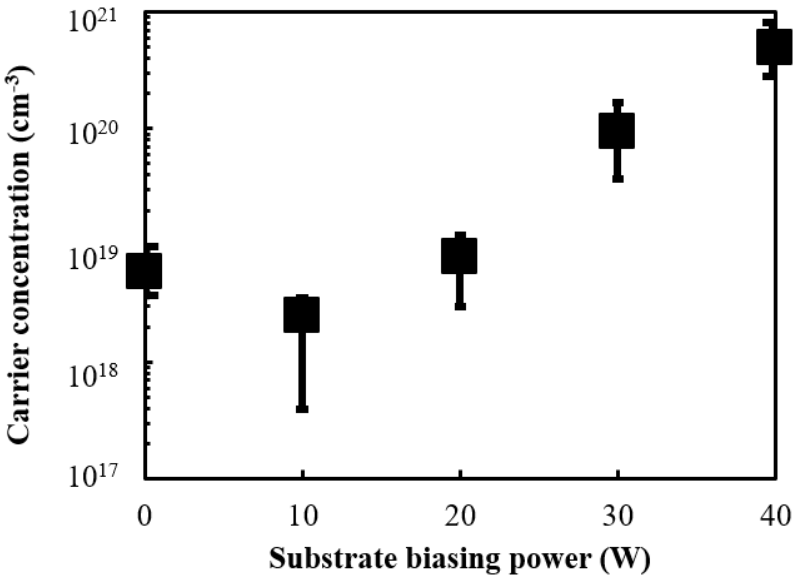

Fig. 3-18 Carrier concentrations measured for films deposited by substrate biasing.

Figure 3-18 shows the carrier concentration measured for VO_2 films deposited by reactive sputtering with substrate biasing. This measurement was performed at room temperature. VO_2 was reported to have a carrier concentration of around 10^{18} to 10^{19} cm^{-3} at room temperature.[115,116] Ruzmemetov *et al.* measured the carrier concentrations of the VO_2 films at high temperature of 90ºC and reported that across the T_t, carrier concentration increases to 10^{23} cm^{-3}.[116] Agreeing that frequently reported range of carrier concentration in VO_2 films measured at room temperature, films deposited at 0, 10, and 20 W were observed to have carrier concentration of around 10^{19} cm^{-3}, respectively. In contrast, a rather higher carrier concentration of 10^{20} cm^{-3} and almost 10^{21} cm^{-3} was measured for films deposited at high-energy ion irradiation of 230 and 300 eV (biasing power of 30 and 40 W). These results of high carrier concentration in high-energy ion irradiated films of 30 and 40 W were observed, agreeing that oxygen vacancies introduced extra electrons in the films. One should note that, VO_2 films deposited by reactive sputtering with substrate biasing were observed to be an electrically conductive n-type semiconductor.

This introduction of free electrons near the octahedral sites is reasonable to cause an early onset of IMT in VO_2 films. The increase of free electrons gives rise to an early metallic-like state that results in rather an early onset of IMT, thus significantly deteriorating the IMT in the in high-energy ion irradiated VO_2 films. From the above matters, the introduction of oxygen deficiency by the high-energy ion irradiation is understood to responsible for the early transition onset, whereas significantly broadened transition properties were observed in the film of 40 W that was deposited with ion energy of around 300 eV. Also, one could expect that introduction of the metallic-like state in films of 30 and 40 W could also contribute for modifying the T_t. Details on the contribution of oxygen vacancies in modifying the T_t in the present work will be discussed in later section.

3.3.6 Transition Temperature Modifications Triggered by Substrate Biasing; Shortening of the In-plane a_M Lattice Length and Oxygen Vacancies

XRD, TEM, and Raman measurements revealed significant modifications of the a_M-axis length and V–V atoms distance in VO_2 films deposited by reactive sputtering with substrate biasing. VO_2 film deposited at ion energy around 140 eV (10 W) with the in-plane tensile stress was observed to have rather higher T_t with significant lengthened in-plane a_M-axis and elongation of the V–V atoms distance. In opposite to that, films deposited at 20, 30, and 40 W (ion energy larger than 200 eV) revealed to have in-plane compressive stress with shortened in-plane a_M-axis length. Strong blue shift in Raman peak at 339 cm^{-1} revealed a strong compression behavior on the V–V atoms distance of these films. Accordingly, these properties of the in-plane stress, in-plane a_M-axis, and V–V atoms pair distance are in good agreement with modifications of the T_t observed in the VO_2 films deposited by reactive sputtering with substrate biasing (presented in chapter 2).

However, as was introduced in the previous section of XPS characterization, energetic ion bombardment also results in an introduction of oxygen vacancies. The introduction of oxygen vacancies results in excess free electrons, which thus introduced metal-like states, and expected to result in an early IMT transition onset in the high-energy ion irradiated VO_2 films. Considering these two factors; shortening of the a_M-axis and high concentrations of oxygen vacancies, that both have their significant effect in reducing the T_t, argumentation on these matters is needed in order to clarify the mechanism of the T_t modifications in the present work. In order to clarify the mechanism of the T_t modifications in the present work, strain along the a_M-axis (in a unit of %) of the films deposited by reactive sputtering with substrate biasing was calculated. The calculation was performed by taking the $a_M/2$-axis of the film with T_t of 68ºC deposited by reactive sputtering with substrate biasing into account. Results of the strain along the a_M-axis as compared to other reported VO_2 films with the T_t modifications obtained by epitaxial-stress control method were plotted in Fig. 3-19.

Figure 3-19 shows the strain along c_R ($a_M/2$)-axis *vs*. transition temperature characteristics plotted for VO_2 films deposited by reactive sputtering with substrate biasing, in comparison to other reported VO_2 films with modified T_t triggered by the epitaxial stress control method. Considering variation that could be introduced by temperature measurement system, c_R-axis at 68ºC of each modification pattern is taken for the strain calculation. As the T_t modifications triggered by the modifications of stress (modifications of c_R-axis), modifications of the T_t was observed to have a linear relationship with changes of the strain along c_R ($a_M/2$)-axis. In the case

of the T_t modifications triggered by the energetic ion bombardment of biasing power from 10 to 30 W, the T_t decreases agreeing on the linear relationship signifying the T_t modifications triggered by the compression strain along the c_R (a_M/2)-axis, correspondingly. However, as for the films deposited with biasing power larger than 30 W (ion energy, E_{ion} > 230 eV), despite of the extensive decrease in the T_t from 55ºC (at 30 W) to 36ºC (at 40 W), slight saturation in the strain changes along the c_R (a_M/2)-axis was observed. The non-linear relationship between T_t and strain along c_R (a_M/2)-axis of the film deposited larger than 30 W revealed that the T_t modifications that achieved are not only triggered by the compression strain along the c_R (a_M/2)-axis. Satisfying these results, the T_t modifications for films deposited with biasing power greater than 30 W (ion energy larger than 230 eV) are expected to be triggered by a collaboration between strain compression along the a_M-axis and oxygen vacancies. An apparent increase in free carrier concentration and oxygen vacancies support this consideration, correspondingly.

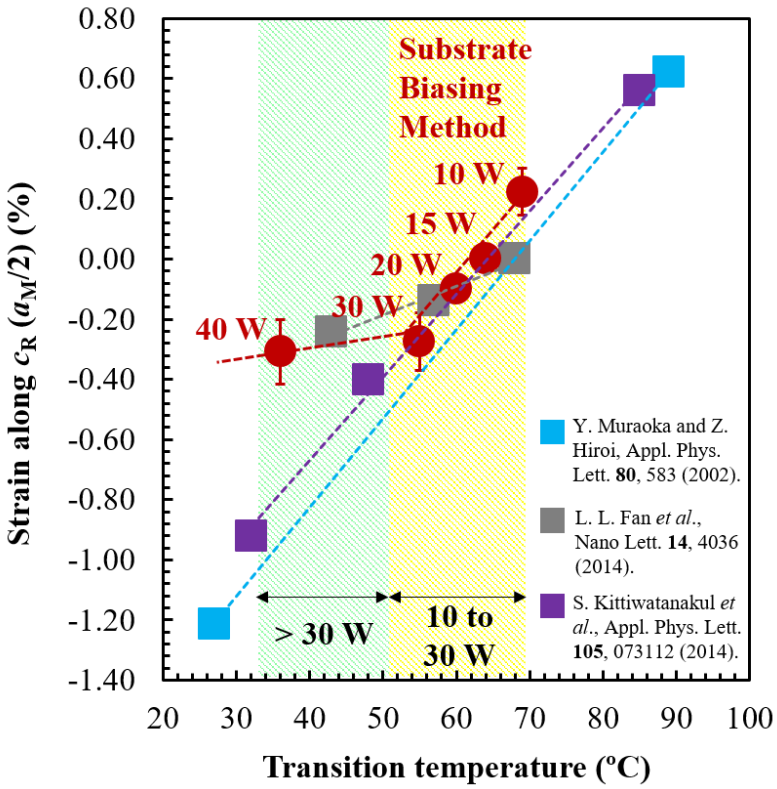

Fig. 3-19 Strain along the c_R (a_M/2)-axis *vs*. transition temperature characteristics.

3.3.7 Film Thickness Consideration; Transition Temperature Modifications in Films with Film Thickness Larger than 100 nm

In the previous section, transition temperature (T_t) modifications were understood to be mainly triggered by the compression of the in-plane $a_M/2$ (c_R)-axis for films deposited with ion energy up to around 230 eV. However, T_t modifications for films deposited with ion energy larger than 230 eV result by a collaboration of strain compression along the a_M-axis and oxygen vacancies. Considering these matters, as a shortening of the $a_M/2$-axis length plays a major role in modifying the T_t, VO_2 films with a thickness of 150 nm were deposited by reactive sputtering with substrate biasing and analysis on the T_t modifications of those films were performed. As known, limitation in film thickness has limited the applications of this VO_2 material.

In this present work, the film thickness was controlled by adjusting the deposition time. By taking the deposition rate (nm/min) into account, the deposition time for each biasing deposition was decided. Deposition rate (nm/min) and deposition time for each substrate biasing power were summarized in Table 3-1. In Chapter 2, the deposition rate was observed to decrease with the increasing of substrate biasing power; the increasing of the ion energy irradiation during sputtering increases the re-sputtering rate, thus results in the decreasing of film thickness. Due to that matter, rather longer deposition time will be needed to obtain rather thicker films, especially for rather higher biasing power. In order to deposit VO_2 films with a thickness of 150 nm, deposition was performed for 25, 30, 40, 60, and 70 min, for the substrate biasing power of 0, 10, 20, 30, and 40 W, respectively.

Figure 3-20 (a) shows the ρ-T characteristics of films with film thickness of 150 nm deposited at biasing power of 0, 10, 20, 30, and 40 W. In correspond to that, Fig. 3-20 (b) shows the T_t for each film, where each film was observed to show the transition of nearly two-order-of-magnitude. While maintaining the transition magnitude and the hysteresis properties, sputtered VO_2 films with a thickness of 150 nm were observed to show significant T_t modifications with increasing of substrate biasing power. From these results, one can understand, the T_t modifications triggered by the substrate biasing would be an efficient method to control the T_t even in the films with a thickness larger than 100 nm. The orientation of a_M-axis in parallel to the substrate has allowed the T_t modifications controlled by the energetic ion irradiation triggered by the substrate biasing method, and thus enable the occurrence of the T_t modification even in rather thicker films. In addition, these results also verify that the T_t modifications triggered by modifications of the growth stress (ion irradiation in this work) could be achieved by having VO_2 with in-plane a_M-axis orientation growth, correspondingly.

Table 3-2 Substrate biasing power, deposition rate, and deposition time.

Substrate biasing power (W)	Deposition rate (nm/min)	Deposition time (min)
0	6.0	25
10	5.0	30
20	3.8	40
30	2.5	60
40	2.3	70

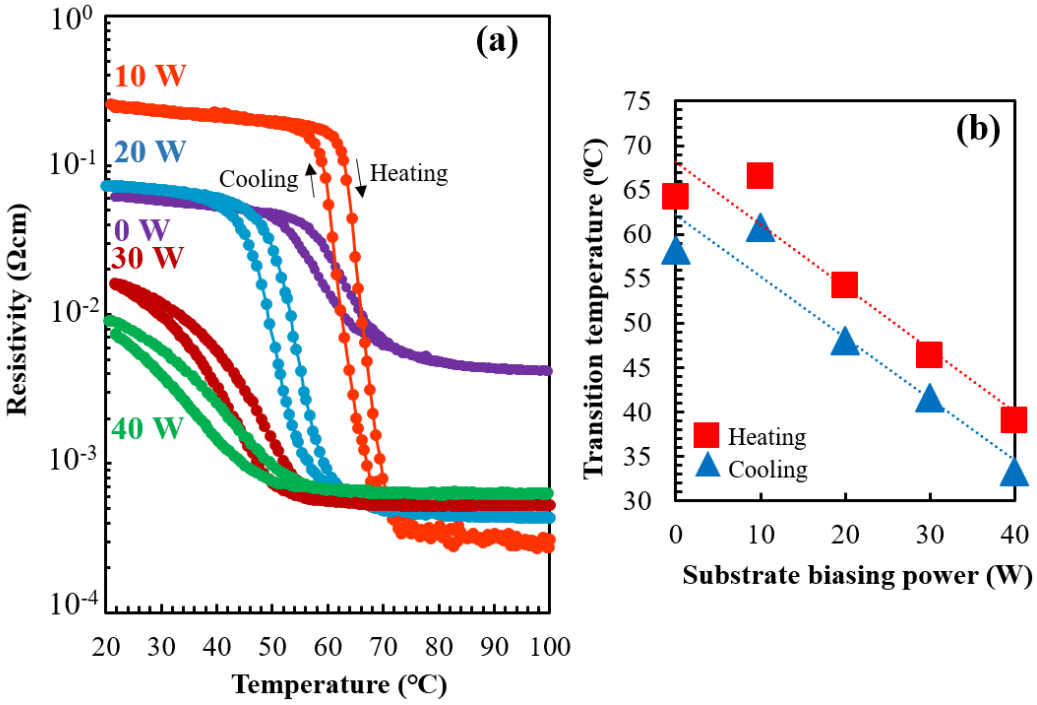

Fig. 3-20 (a) ρ-T characteristics (b) transition temperature for both heating and cooling of films with a thickness of 150 nm deposited by the substrate biasing power of 0, 10, 20, 30, and 40 W.

3.4 Conclusions

In this chapter, the mechanism behind the transition temperature (T_t) modifications in films deposited by reactive sputtering with substrate biasing was discussed. VO_2 films on Al_2O_3 (001) substrates deposited with the substrate biasing power of 0, 10, 20, 30, and 40 W with ion energy of 30, 140, 200, 270, and 300 eV with the T_t respectively at 66ºC, 69ºC, 65ºC, 55ºC, and 36ºC were mainly discussed.

In-plane stress state (σ) of the sputtered VO_2 films was estimated by considering the shift of the VO_2 $(020)_{M1}$ peak that corresponds to the out-of-plane b_M-axis length. The in-plane stress was of tensile state in the film deposited at ion energy of 140 eV (10W), then turned into the compressive state by increasing the ion energy to a value larger than 200 eV ($\geq$ 20 W). At the substrate biasing power of 10 W, tensile stress was remained due to thermal stress effect resulting in T_t higher than 68ºC. As the stress conversion from tensile to compressive occurred at around 20 W with enhancement of ion energy beyond 200 eV, T_t modifications towards lower temperature was observed. Accordingly, the in-plane tensile and compressive stress should give significant elongation and compression of the in-plane a_M-axis in the film of 10 W (E_{ion} around 140 eV) and films of 20, 30, and 40 W ($E_{ion} \geq 200$ eV).

TEM images revealed improved crystalline properties of columnar crystalline structure in the film deposited at ion irradiation energy of around 200 eV (20 W). High ion irradiation energy of around 300 eV was observed to result in the collapsed columnar structure with significant densification of the grains in the film of 40 W. High-resolution TEM images gave information on the out-of-plane b_M (a_{R2})-axis and the in-plane $c_M \sin\beta$ (a_{R1})-axis. As results, shortened out-of-plane axis and elongated in-plane axis were observed in the film deposited at 10 W (E_{ion} around 140 eV). In contrast, lengthening of the out-of-plane axis and shortening of the in-plane axis length were observed in the films deposited at 20, 30, and 40 W ($E_{ion} \geq 200$ eV), correspondingly. These observations support the hypothesis proposed before; the in-plane compression stress results in the elongation of the out-of-plane axis and shortening of the in-plane axis.

Asymmetrical XRD measurements revealed the relation between the in-plane $a_M/2$-axis length and the T_t. In agreement with the in-plane tensile stress observed in the film of 10 W, rather longer in-plane $a_M/2$ lattice length was observed with an average length of 2.888 Å. Later increasing in substrate biasing power to 20 to 30 W, in-plane $a_M/2$ lattice length was observed to decrease in almost linear relationship to 2.879 Å and 2.874 Å. As substrate biasing power increases to 40 W, $a_M/2$ axis was observed to shorten to 2.873 Å. However, different from the

shortening of $a_M/2$ lattice length from 10 to 30 W, slight saturation in the shortening of $a_M/2$ lattice length was observed. Despite slight saturation in the shortening of the $a_M/2$ lattice length, the increasing of ion energy from 140 eV (10 W) to 200 eV (20 W) results in the evolution of the in-plane stress state from tensile to compressive, where significant lengthening and shortening of $a_M/2$ lattice length were observed on films deposited at 10 W and 20 W, respectively. Film deposited at 40 W (300 eV) revealed to have the shortest $a_M/2$ lattice length, signifying the lowest T_t value observed in this work. These observations revealed that the modifications of the T_t triggered by the energetic ion irradiation in this substrate biasing reactive sputtering are due to the modifications of the $a_M/2$ lattice length.

Considering the shortening of the in-plane $a_M/2$-axis length in films deposited with a biasing power larger than 20 W ($E_{ion} \geq 200$ eV), V–V atoms distance also was expected to decrease as the V atoms reside on the a_M-axis. Significant compression behavior of V–V atoms in films deposited at high energy ion irradiation was revealed as a blue shift of Raman peak at 339 cm^{-1}. The decreasing of the V–V atoms distance along the a_M-axis strengthened the V–V atoms pair, thus trigger an early occurrence of the SPT and IMT in VO_2. Through these discussions, continuous strikes of the high energy ions during the deposition are responsible for inducing the in-plane compressive stress that results in the shortening of the in-plane a_M-axis length and also the V–V pair distance. This thus led to the decreasing of the T_t in films deposited with a substrate biasing power larger than 20 W ($E_{ion} \geq 200$ eV).

Continuous strikes of high-energy ions were also expected to introduce the oxygen defects in films. In order to discuss the introduction of oxygen defects in the sputtered films, XPS measurement was performed. V $2p_{3/2}$ spectra weight changes from V^{4+} to low oxidation states of V^{2+} and V^{3+} suggested that high-energy ions introduce defects population and partially contribute for modifying the transition properties. The introduction of the oxygen vacancies in high-energy irradiated films introduce free electrons near the octahedral sites and give rise to an early metallic-like state that results in rather an early onset of the IMT. This, thus significantly deteriorating the IMT properties of the VO_2 films, whereas significantly broadened transition properties were observed in the film of 40 W (300 eV).

Characterization of the strain along c_R ($a_M/2$)-axis *vs*. transition temperature characteristics revealed that the T_t modifications in films deposited by reactive sputtering with substrate biasing are understood to be mainly triggered by the compression of the in-plane $a_M/2$ (c_R)-axis for films deposited with ion energy up to around 230 eV ($\leq$30 W). However, T_t modifications for films deposited with ion energy larger than 230 eV (> 30 W) result by a collaboration of strain

compression along the a_M-axis and oxygen vacancies. The orientation of a_M-axis in parallel to the substrate has allowed the T_t modifications controlled by the energetic ion irradiation during the sputtering with substrate biasing, and thus enable the occurrence of the T_t modifications even in rather thicker films (films thicker than 100 nm).

Chapter 4

Micro-sized Grains Growth under Particular Substrate Biasing

Chapter 4 Micro-sized Grains Growth under Particular Substrate Biasing

4.1 Introduction

During previous chapters, high substrate biasing power was observed to be effective in reducing the T_t of the VO_2 films on Al_2O_3 (001) substrates. High-energy ion irradiations during sputtering revealed to shorten the in-plane a_M-axis length, thus, significantly reduce the V–V atoms distance in VO_2 films. During this study, unique growth aspects of VO_2 films on Al_2O_3 (001) were observed, where the unusually large crystalline grains with the size over several μm appeared under particular biasing power.[117] Together with this unique crystalline growth, the small conventional grains with average size of several hundred nm were also observed. Considering the growth aspect of VO_2 on Al_2O_3 (001) that supposed to result in only several tens nm grain size, the growth of micro-sized grains VO_2 is an interesting topic needs to be discussed. In this chapter, structural morphologies of the μm-sized grains will first be discussed. Later, crystalline properties of the μm-sized grains will be delivered. Then, the growth mechanism and the applications of these μm-sized grains by the substrate biasing method will be proposed. Finally, IMT and SPT of the μm-sized crystalline grains, including its stress state, will be revealed.

4.2 Experimental methods

Films were deposited on a double side polished Al_2O_3 (001) substrate that was ultrasonically cleaned in acetone for 3 min and rinsed in pure water. Depositions were performed at a constant substrate temperature, oxygen and argon flow rate, and target power of 400ºC, 2.5 and 38 sccm, and 200 W, respectively, with constant total gasses ambient pressure of 0.5 Pa for 40 minutes time. During deposition, only substrate biasing power was varied.

R-T characteristics were performed for both heating and cooling runs between room temperature and 100°C. 2θ-θ scans and rocking curve measurements in XRD (X'Pert MRD Philips Co.) were performed using Cu Kα radiation. Temperature-controlled Raman spectroscopy was carried out by using a reflex device (Renishaw, inVia) and a temperature controller (Linkam, THMS 600). An argon-ion laser with 514.5 nm in wavelength and 0.5 mW in power was used as the excitation light source. Field emission scanning electron microscopy (FE-SEM) and atomic force microscopy (AFM) measurements were carried out for the film morphologies observation. Electron Probe Micro-Analyzer (EPMA) measurement was performed to study oxygen distribution on the sputtered VO_2 films.

4.3 Results and Discussion

In previous chapters 2 and 3, the film deposited at 10 W was introduced to have peculiar growth aspects, where mixed growth with the orientation of VO_2 (020) and (011) planes was observed. In this film of 10 W, μm-sized grains were observed together with the conventional nano-sized grains in FE-SEM. It should be noted that the μm-sized grains appeared only on films deposited under particular substrate biasing power of 10 W. In chapter 3, in different to films of 20, 30, and 40 W with that T_t shift to rather lower temperature, film of 10 W shows shifting of the T_t towards higher temperature due to the in-plane tensile stress with elongation in the in-plane a_M-axis length and V–V atoms distance, accordingly.

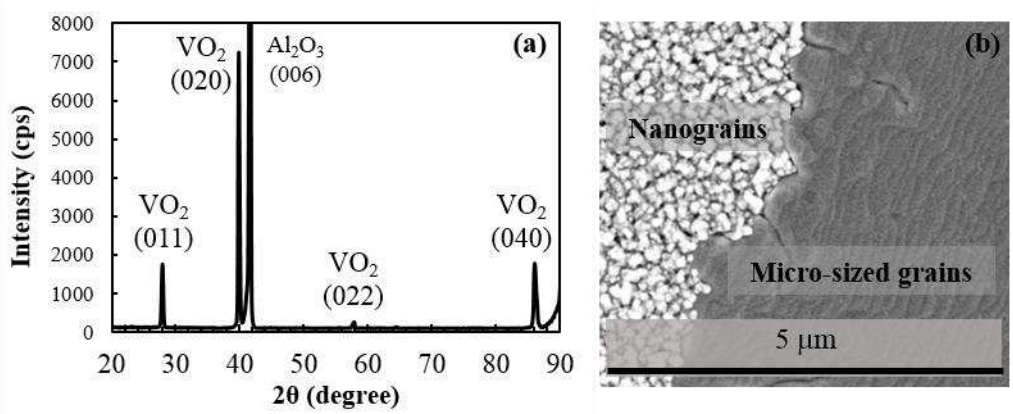

Fig. 4-1 Characteristics growth of the VO_2 film on Al_2O_3 (001) substrate deposited at 10 W observed trough (a) XRD profile and (b) FE-SEM image.

Figure 4-1 shows different characteristics growth of the VO_2 film on Al_2O_3 (001) substrate deposited with the substrate biasing power of 10 W observed through XRD 2θ-θ scan profile and FE-SEM image. In the XRD 2θ-θ scan profile, one can observe four diffraction peaks corresponding to VO_2 $(010)_{M1}$ orientation with diffractions from (020) and (040) planes at 2θ = 39.83º and 85.88º, and VO_2 $(011)_{M1}$ orientation with those from (011) and (022) planes at 2θ = 27.85º and 57.54º. Corresponding to this two-orientation growth on film of 10 W, FE-SEM revealed two different regions growth of the conventional nanograins and the unusual μm-sized grains that will later be known as nanograins and μm-sized grains regions. In previous chapters, film of 10 W was discussed only regarding its nanograins region. In this chapter, characteristics of the μm-sized grains region will be discussed.

4.3.1 Morphologies of the Micrometer-sized VO_2 Grains

FE-SEM images shown in Fig. 4-1 (b) revealed the two-type region of the film deposited at 10 W. Fig. 4-2 shows microscopic images for a film of 10 W, where optically dark and bright areas composed of nanograins and μm-sized grains coexist, accordingly. The film of 10 W was observed to have two types of regions, one with several tens nm-sized small grains and the other with large grains structure with size over several μm-sized grains. As mentioned in the introduction part, this growth is unusual considering the growth direction of VO_2 on Al_2O_3 (001) substrate, where relatively small nanograins of highly oriented $(010)_{M1}$-orientation is expected.

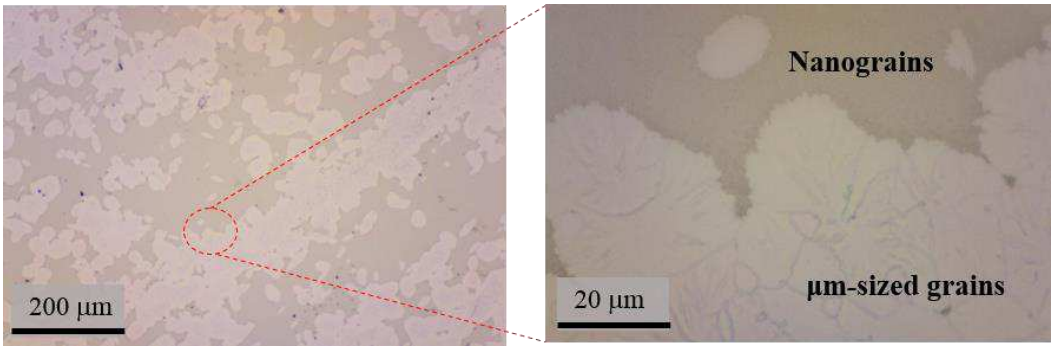

Fig. 4-2 Optical microscopic images of the film deposited at 10 W. Reproduced from [ref. 117 of J. Appl. Phys. **117**, 245314 (2015)], with the permission of AIP Publishing.

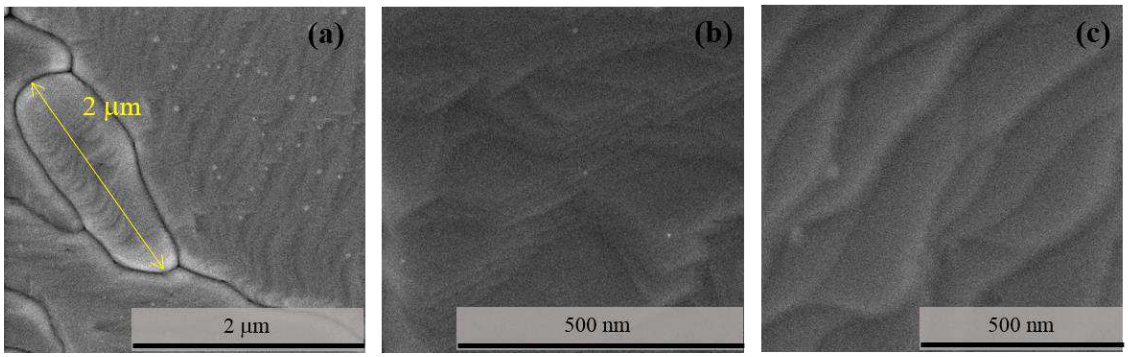

Fig. 4-3 High-resolution FE-SEM images for single large crystalline grains.

Figure 4-3 shows several characteristic high-resolution FE-SEM images of large grains structure on film of 10 W. In Fig. 4-3 (a), one can observe single grains structure with a length of nearly 2 μm. This single crystal-like growth mode was grown in wide areas with random size, where the largest grains could grow to nearly 10 μm. High-resolution of FE-SEM images (in Fig. 4-3 (b) and (c)) revealed smooth step and terrace structures of the large grains with sizes of several tens nm. The well-aligned step and terrace structures suggest a single crystalline growth inside

the domain. The step and terrace structures of the large crystalline grains were then precisely characterized by performing surface profiling of AFM measurements.

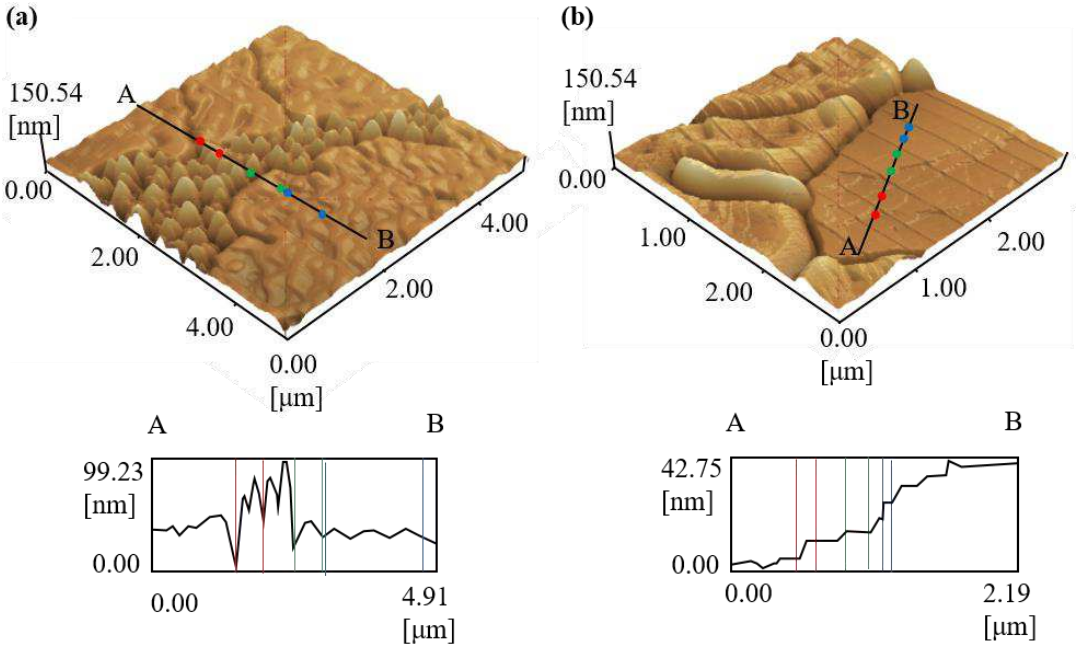

Fig. 4-4 AFM images of the film deposited at 10 W, consists of nanograins and large domains, where (a) nanograins+ μm-sized grains and (b) μm-sized grains with step and terrace structure, respectively. Reproduced from [ref. 117 of J. Appl. Phys. **117,** 245314 (2015)], with the permission of AIP Publishing.

Figure 4-4 shows AFM images of the film deposited at 10 W, consisting of two different regions, nanograins, and μm-sized grains. Area of 25 μm^2 that consists both nanograins and μm-sized grains region (Fig. 4-4 (a)) and a segment with an area of 9 μm^2 (Fig. 4-4 (b)) were taken into consideration. In the cross-sectional profiling analysis result of Fig. 4-4 (a), a very smooth surface of large grains structure was observed, indifferent to that of the nanograins structure. One can also find some grains are rather flatter than others. In Fig. 4-4 (b), the cross-sectional profile was revealed to confirm the step and terrace structure of the μm-sized grains. Most of the large crystalline grains were observed to show the same order of step height and terrace width; several tens nm for each. The cross-sectional profiles with the step and terrace structures satisfied the single crystalline growth behavior of the large crystalline grains.

TEM observations were performed to support the single crystalline behavior of the large grains grow on the film of 10 W, with an observation of the nanograins was also performed for comparison. Figure 4-5 shows cross-sectional TEM images of nanograins and μm-sized grains on the film deposited at 10 W. In agreement with the nanograins structure observed on other sputtered VO_2 films; fine columnar grains were also observed on the film of 10 W (Fig. 4-5 (a)). In

comparison to the several tens nm size of columnar structure observed in the film of 20 W (shown in Fig. 3-7 (c)), rather large grains with size of nearly 100 nm was observed on film of 10 W. In different, single crystalline μm-sized grains, where single crystal with the size of nearly of 2 μm was observed in Fig. 4-5 (b). Also, the appearance of an amorphous layer between the VO_2 films and the Al_2O_3 substrates was observed. However, it is important to mention that there is also some other part of μm-sized grains regions that does not consist the amorphous layer. One should be noted, the film thickness for nanograins and μm-sized grains regions are both same, with a thickness of approximately 200 nm.

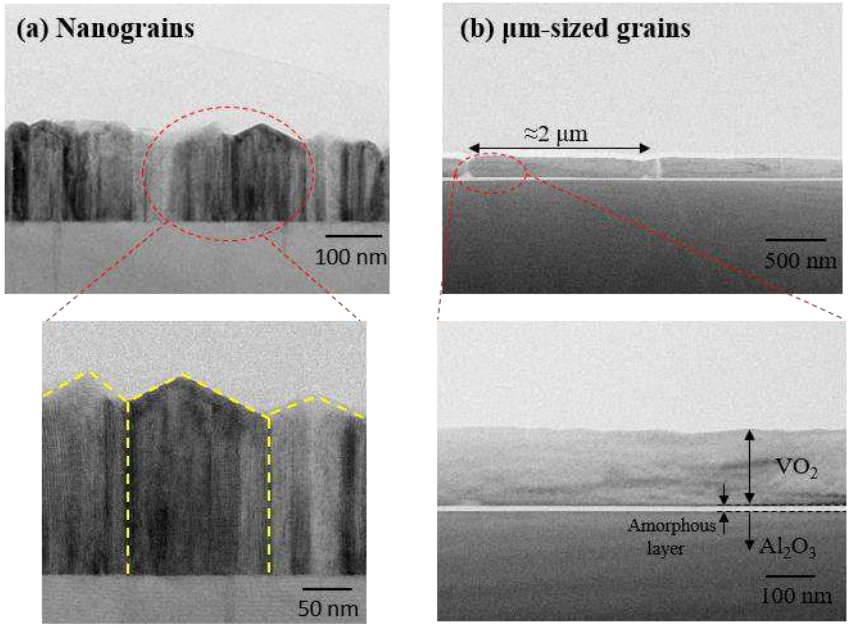

Fig. 4-5 TEM observations of (a) nanograins and (b) μm-sized grains for a film of 10 W.

4.3.2 Micro-sized VO_2 Grains; Growth Concepts and Applications View

4.3.2.1 Micro-sized Grains Growth Concepts

The growth of the μm-sized grains of VO_2 films on Al_2O_3 (001) substrates is undoubtedly extraordinary considering the lateral domains growth with its in-plane crystal size is several times larger than its out-of-plane size (film thickness). High reproducibility of this crystalline growth motivated further studies on this crystal growth to be performed.

Considering the growth direction of the VO_2 on Al_2O_3 (001) substrate that only allows the growth of crystals with several nm in size, some other chemical phenomena are expected to occur in the chamber of either during or after the deposition (cooling) process. Here, recrystallization was proposed to occur and thus, resulted in the growth of the rather stable crystalline growth of (011) plane with rather large grains size, correspondingly. Recrystallization phenomena have been long recognized to occur during the thermomechanical process and known to be potentially happened in all types of materials.[118] However, this phenomenon was often reported only in the case of metals, in which the melting point of materials are significantly low. Koch reported a remarkable large grain in Ag (001) film with an average size of 1 μm.[119] To date, this phenomenon is often studied with its relation to the post-annealing process.[118,120]

To support this hypothesis, recent work by Makarevich *et al.* also proposed that the recrystallization could also occur in VO_2 films by post-annealing the VO_2+V_nO_{2n+1} at a temperature of around 600ºC.[26] Considering this matter, the growth of the μm-sized grains under particular biasing conditions in the present work might also be related to the existence of the high-oxidation phase, V_nO_{2n+1}. To study this matter, detailed consideration of the XRD patterns of the 2θ-θ scan was performed. Figure 4-6 shows the XRD patterns of VO_2 films deposited with the substrate biasing power of 0, 10, and 20 W with O_2 flow rate of 2.5 sccm (a) and VO_2 film deposited with rf sputtering (non-biasing) with O_2 flow rate of 1.0 sccm (b). Note that, this non-biasing film is the same film as was introduced in Chapters 2 and 3. In comparison to non-biasing film and film deposited at 20 W, films deposited at 0 and 10 W were observed to have a characteristic of broad peak at around 2θ = 20º, suggesting the growth of amorphous V_nO_{2n+1}. This growth of amorphous V_nO_{2n+1} in the film of 10 W supports the hypothesis proposed before; the growth of the μm-sized grains is related to the existence of the V_nO_{2n+1}.

Also, to support the co-existence of V_nO_{2n+1}, which thus significantly contribute to the growth of the μm-sized grains, Electron Probe Micro-Analyzer (EPMA) measurement was

performed to study oxygen distribution on the sputtered VO_2 films. Figure 4-7 shows EPMA mapping images for oxygen of films deposited at 0, 10, and 20 W. Agreeing on the existence of V_nO_{2n+1}, uniform high distribution of oxygen was observed in film of 0 W. On film of 10 W with two regions growth of nano- and μm-sized grains, oxygen was observed to be highly distributed in the nanograins region. As the biasing power increases to 20 W, the selective sputtering (i.e. oxygen) occurred, thus results in the balance and uniform oxygen distribution on the film.

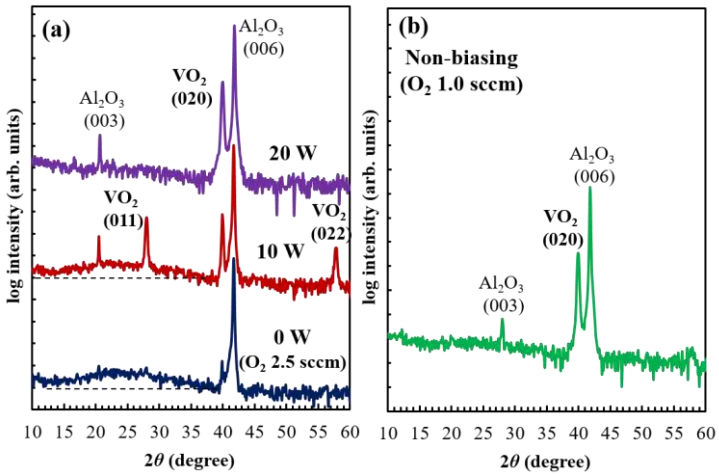

Fig. 4-6 XRD patterns of VO_2 films deposited (a) with the substrate biasing power of 0, 10, and 20 W with O_2 flow rate of 2.5 sccm and (b) with normal rf sputtering with O_2 flow rate of 1.0 sccm.

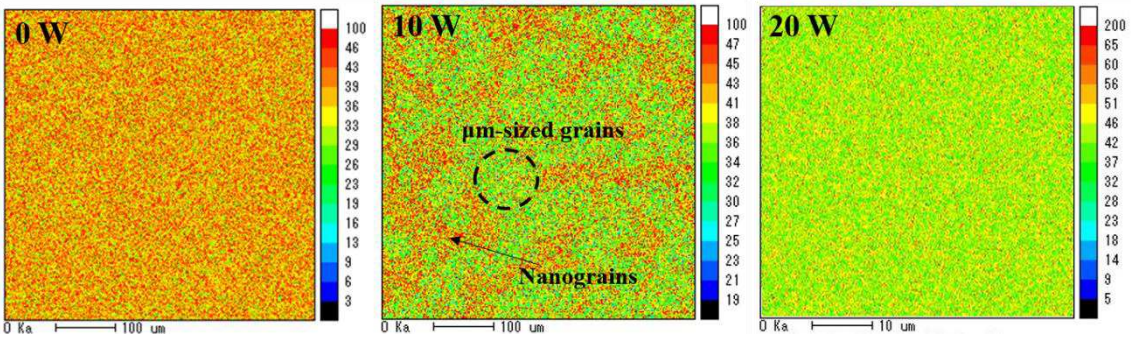

Fig. 4-7 EPMA mapping images for oxygen of films deposited at 0, 10, and 20 W.

The above results support the co-existence of V_nO_{2n+1}, which thus significantly contribute to the growth of the μm-sized grains. According to the V_2O_3-V_2O_5 phase diagram, V_nO_{2n+1} has rather low melting temperature (T_M) of around 670ºC (at a pressure of 1 Pa). As a note, depositions were performed at a constant substrate temperature (T_S) of 400ºC. In this work, in which total gasses ambient pressure is constant at 0.5 Pa, 10% decrease in the T_M is expected. The existence of high-oxidation phase, V_nO_{2n+1} results in the increasing of homologous temperature (T_S/T_M) value to around 0.77. The recrystallization occurs due to an effective atomic diffusion, thus introduce the

energetically favorable VO_2 $(011)_{M1}$ plane. In order to keep the thermodynamic equilibrium of the film, shrinkage of the $(020)_{M1}$ occur simultaneously with the continuing growth of the energetically favorable VO_2 $(011)_{M1}$ plane, resulting in the growth of the large crystalline grains.

As mentioned earlier, this growth of μm-sized grains only appeared on films deposited under certain biasing condition, i.e. 10 W. One could expect the effect of the ion bombardment in assisting and preventing the recrystallization in the present work. Appropriate ion bombardment conditions proposed to help in introducing active occurrence of atoms diffusion and providing high defects concentrations that work as a driving force for the recrystallization. However, further increasing in the ion bombardment results in the selective sputtering that decreases the existence of oxygen in films and the occurrence of ion peening prevent the occurrence of recrystallization.

4.3.2.2 Applications view of μm-sized crystalline grains

Micro-sized crystalline grains growth of VO_2 films on Al_2O_3 (001) substrates with sizes over several μm could lead in opening new vistas of VO_2 thin films growth.

Raman spectroscopy technique, which allows studies on the SPT and the stress analysis, is one of the important measurement in studying the characteristics of VO_2 thin films. However, through these years, no consensus was reached for Raman modes assignment of VO_2 M1 phase, due to the lack of single crystals VO_2. Most studies were conducted on oriented or epitaxial thin films with nano-sized crystal grains. By considering the size of the laser spot, where can only focus on an area of 300 nm in diameter, recorded Raman spectrum represents contributions of multiple grains. This thus results in the maximum of 12 to 13 modes observation of the VO_2 M1 phase. Recently, this growth of the μm-sized crystals grains of more than 10 μm with their single-crystalline properties has allowed polarized Raman scattering measurement to be performed, thus allowed the assignment of the 17 modes among the 18 expected modes in VO_2 M1 phase.[108]

In addition, this μm-sized crystalline growth phenomenon could have been utilized for the development of a low-temperature, low-cost process of VO_2 layers for optical devices, such as smart windows, or even for electronic devices if the problem of a weak link at domain boundaries will be solved.

4.3.3 Crystalline and Transition Properties of the μm-sized Crystalline Grains

The characterization of crystalline properties was performing XRD analysis of omega scans. In a comparison to that film deposited at 10 W with nanograins + μm-sized grains and the films of 20, 30, and 40 W that consists of nanograins only, the crystal growth of μm-sized grains region was confirmed to be in the $(011)_{M1}$-orientation.

In this section, crystalline properties of the VO_2 films will be discussed concerning the film of 10 W (nanograins + μm-sized grains) and the film with most improved crystalline properties of the film deposited at 20 W (nanograins only). Figure 4-6 (a) illustrates the XRD analysis profiles of 2θ-θ scan of the film deposited at 10 W and 20 W measured at room temperature. Figure 4-8 (b) shows the normalized ω scan profiles taken for $(020)_{M1}$ peak for films deposited at 0, 20, and 40 W. Despite of different full-width half maximum (FWHM) of those peaks; all films confirm to have $(010)_{M1}$-orientation growth, respectively. In comparison to that film of 20 W (nanograins only), a film of 10 W (nanograins + μm-sized grains) revealed to have rather good crystalline properties as rather smaller FWHM value of almost 0.2° was observed. Fig. 4-8 (c) illustrates the normalized ω scan profiles of $(011)_{M1}$ peak for film of 10 W. Different to the typical ω scan profiles for $(020)_{M1}$, $(011)_{M1}$ was observed to have a sharp peak with FWHM of almost 0.2° (not so far different with that observed for $(020)_{M1}$ peak), superimposing the high background signal. From the ω scan profile of $(011)_{M1}$ peak, the film of 10 W also confirmed to have an orientation of $(011)_{M1}$ plane.

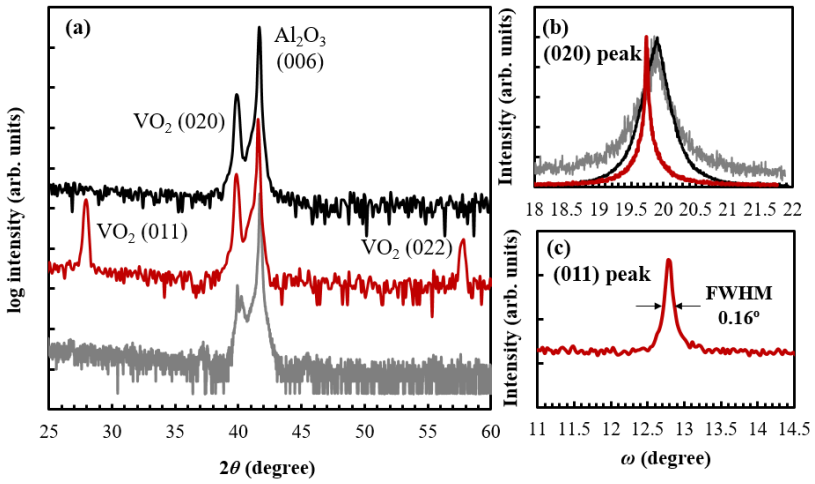

Fig. 4-8 XRD analysis of (a) 2θ-θ scan profile for films of 0, 10, and 20 W, with ω scan profiles of the $(020)_{M1}$ and $(011)_{M1}$ peaks are shown in (b) and (c).

Temperature-dependent XRD analysis was performed to study the crystalline properties of film 10 W, in which the film revealed to have the in-plane tensile stress. Agreeing on the VO_2 strain-temperature phase diagram, in-plane tensile stress proposed resulting in the appearance of another monoclinic phase, known as VO_2 M2 phase.[34] Figure 4-9 (a) and (b) shows the temperature-dependent XRD analysis for a film of 10 W, corresponding to that of $(020)_{M1}$ and $(011)_{M1}$ peaks, respectively. Profiles for the film deposited at a biasing power of 20 W is given in Fig. 4-9 (c) for comparison.

SPT in VO_2 occurs from M1 to R phase at a temperature of 68ºC (in bulk). Temperature-dependent Raman spectra (shown in Fig. 2-18) revealed this M1 to R phase transition on films deposited by substrate biasing of 20, 30, and 40 W, also for the nanograins region of film 10 W. As one can observe in Fig. 4-9 (a), at a temperature of 66ºC, the appearance of a new diffraction at $2\theta = 28.25^{o}$ was observed in corresponding to (201) plane of M2 phase, respectively.[37,121] The diffraction intensity of this peak getting smaller with the increasing temperature, but remains to be until rather high temperature, before completely disappear at 96ºC. The single peak in high temperature (of 96ºC) at $2\theta = 27.70^{o}$ corresponds to the VO_2 $(110)_R$ suggests a completion of the SPT in the film. As for the VO_2 $(020)_{M1}$ peak, the shift of the peak from $2\theta = 39.94^{o}$ to 39.90^{o}, signifying the peak shifts from VO_2 $(020)_{M1}$ to $(200)_R$ was observed. However, as one could find, this shift was a small (shift of -0.04^{o}) compared to the peak shift observed in the film of 20 W (shown in Fig. 4-9 (b)) for of almost -0.1^{o}.

From these above results, one can understand, agreeing the in-plane tensile stress of film deposited at 10 W, the occurrence of SPT, where the M2 phase appeared as an intermediate phase of the transition from the M1 to R phase. One can also propose that this appearance of the M2 phase was due to the growth of the μm-sized crystalline grains since only the peak of $(011)_{M1}$ phase show the significant appearance of this M2 phase. However, it was difficult to clarify this matter with only the XRD profiles. Thus, to clarify this occurrence of M2 phase, micro-Raman measurement on the μm-sized grains was performed and will be discussed in the next section.

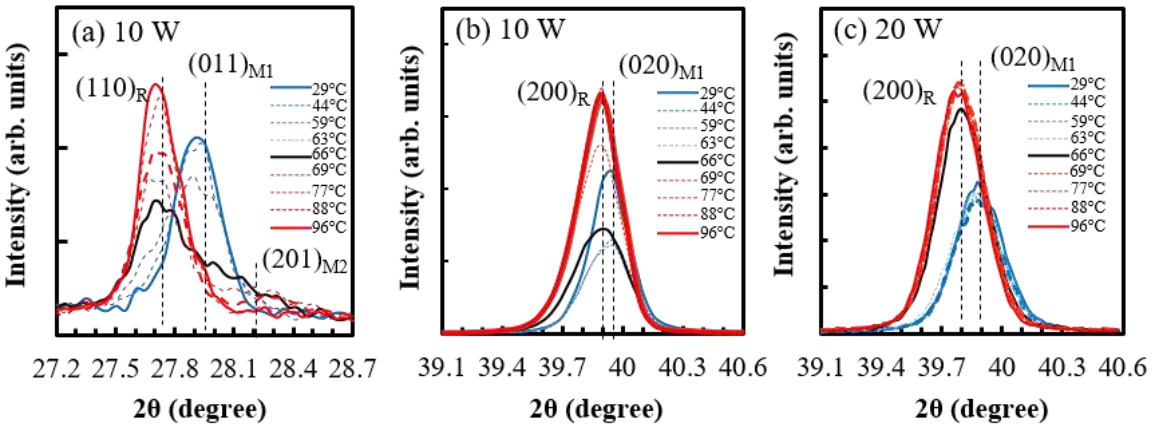

Fig. 4-9 Temperature-dependent XRD for the film deposited at 10 W, in correspond to its (a) $(011)_{M1}$ peak and (b) $(020)_{M1}$ peak. Profiles for a film of 20 W is given in (c). Reproduced from [ref. 117 of J. Appl. Phys. **117**, 245314 (2015)], with the permission of AIP Publishing.

4.3.4 Temperature-dependent Raman Spectra of μm-sized Crystalline Grains

In this section, the SPT of this film of 10 W will be further discussed by choosing the regions, accordingly. Single μm-sized crystalline domains with its size could be as large as 10 μm has allowed measurement on the selected region to be performed.[108] Figure 4-10 shows the temperature-dependent Raman spectra measured at the nanograins and the μm-sized grains.

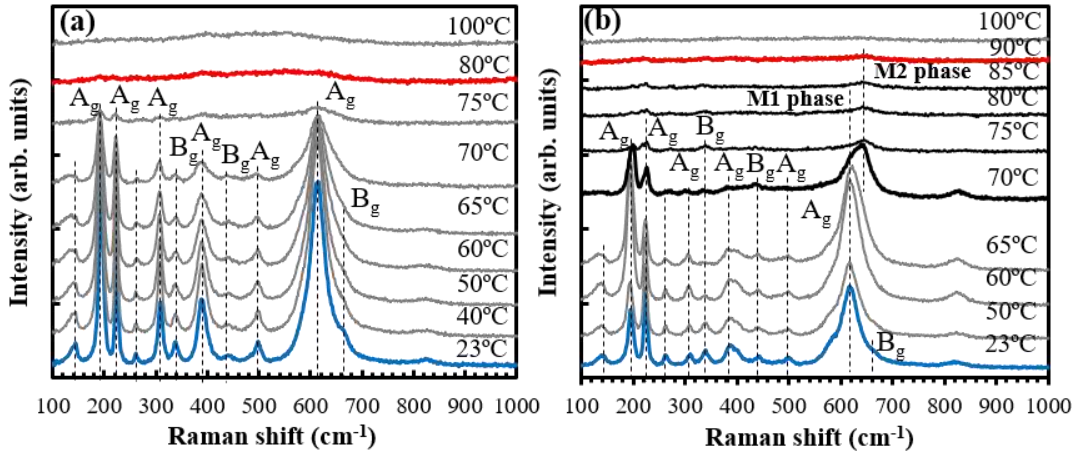

Fig. 4-10 Temperature-dependent Raman spectra of (a) nanograins and (b) μm-sized grains regions. Reproduced from [ref. 117 of J. Appl. Phys. **117**, 245314 (2015)], with the permission of AIP Publishing.

Figure 4-10 shows the temperature-dependent Raman spectra taken at both nanograins and the μm-sized grains regions, whereas the profile for nanograins was once shown in Fig. 2-18. Regarding the nanograins region as explained before, in comparison to other films of 20, 30, and 40 W, M1 phase on this nanograins region of film deposited at 10 W was observed to remain existed until rather high temperature over 75ºC. This suggests strong in-plane tensile stress in the film of 10 W that correspondingly results in the high transition temperature. As for the μm-sized grains region, at a temperature of 70ºC, peak at 619 cm^{-1} that resemble the VO_2 M1 phase shifted to slight higher position of around 645 cm^{-1} indicating the appearance of the VO_2 M2 phase in this μm-sized grains region. The M2 phase was observed to retain until high temperature of around 85ºC before then completing the SPT at 90ºC.

From these results, one could proposed that the appearance of the intermediate phase of M2 phase in the μm-sized grains crystal will be responsible for the late transition completion in the VO_2 film with nanograins and the μm-sized grains of film deposited at 10 W. The appearance of the VO_2 M2 phase in the μm-sized grains was a thing that should be remarked. In comparison to the nanograins region, where SPT was observed to occur from M1→R phase, the μm-sized grains shows the occurrence of SPT from M1→M2→R phase, respectively.

4.4 Conclusions

Large crystalline grains of several μm-sized was first observed, where non-epitaxial $(011)_{M1}$ phase orientation is dominating the growth in VO_2 films deposited on Al_2O_3 (001) substrates deposited under adequate substrate biasing of 10 W (in this work).

XRD 2θ-θ scan profile revealed four diffraction peaks corresponding to VO_2 $(010)_{M1}$ orientation on film deposited at 10 W, with diffractions from (020) and (040) planes at 2θ = 39.83º and 85.88º, and VO_2 $(011)_{M1}$ orientation with those from (011) and (022) planes at 2θ = 27.85º and 57.54º. Corresponding to the two-orientation growth on film of 10 W, FE-SEM revealed two different regions growth of the conventional nanograins and the unusual μm-sized grains regions. Cross-sectional profiling of AFM measurements revealed the step and terrace structure of the μm-sized grains. , where most of the large crystalline grains were observed to show the same order of step height and terrace width; several tens nm for each. The cross-sectional profiles with the step and terrace structures satisfied the single crystalline growth behavior of the large crystalline grains. Agreeing that AFM cross-sectional profiles, TEM observations revealed the single crystalline growth of the μm-sized grains.

Micro-sized grains growth mechanism and applications of the μm-sized grains were discussed. The appearance of broad peak at around 2θ = 20º in XRD profiles of 2θ-θ scan suggested the appearance of amorphous V_nO_{2n+1} in film with μm-sized grains growth. Also, EPMA revealed the coexistence of highly distributed oxygen (nanograins) on film with μm-sized grains growth. The above results support the co-existence of V_nO_{2n+1}, which thus significantly contribute to the growth of the μm-sized grains. The existence of high-oxidation phase (V_nO_{2n+1}) results in the increasing of homologous temperature (T_S/T_M) value to around 0.77. Considering this matter, recrystallization occurs due to an effective atomic diffusion, thus introduce the energetically favorable VO_2 $(011)_{M1}$ plane. In order to keep the thermodynamic equilibrium of the film, shrinkage of the $(020)_{M1}$ occur simultaneously with the continuing growth of the energetically favorable VO_2 $(011)_{M1}$ plane, resulting in the growth of rather large crystalline grains; μm-sized grains.

Since this growth of μm-sized grains only appeared on films deposited under certain biasing condition, one could expect the effect of the ion bombardment in assisting and preventing the recrystallization in the present work. Appropriate ion bombardment conditions proposed to help in introducing active occurrence of atoms diffusion and providing high defects concentrations that work as a driving force for the recrystallization. However, further increasing in the ion

bombardment results in the selective sputtering that decreases the existence of oxygen in films and the occurrence of ion peening prevent the occurrence of recrystallization.

Temperature-dependent XRD measurements revealed the appearance of M2 phase as an intermediate phase of the transition from the M1 to R phase of film with mixed nanograins and μm-sized growth. The appearance of M2 phase as intermediate phase supported the in-plane tensile stress behavior of film 10 W with T_t higher than 68ºC. Temperature-dependent micro-Raman measurements were performed to clarify the origin of the M2 phase, as the measurement on the selected area could be performed. Accordingly, in comparison to the nanograins region, where SPT was observed to occur from M1→R phase, the μm-sized grains shows the occurrence of SPT from M1→M2→R phase, respectively. Also, the appearance of the intermediate phase of M2 phase in the μm-sized grains crystal was undersood to be responsible for the late transition completion in the VO_2 film with nanograins and the μm-sized grains of film deposited at 10 W.

Chapter 5

Summary and Future Works

Chapter 5 Summary and Future Works

5.1 Summary

In this work, with the main objective to control the transition temperature (T_t) in VO_2, rf substrate biasing was introduced to study the effect of high-energy ion irradiation on the crystalline and transition properties of VO_2 thin films.

In Chapter 1, an overview of VO_2, including crystalline structure, electronic behavior, and, fabrication techniques will be reviewed. A brief outline regarding works on the modifications of the T_t in VO_2 thin films will then be given. Later, problem statements and the objective of the present work will firstly be introduced. Finally, a roadmap for the rest of the dissertation will be proposed.

In Chapter 2, rf magnetron reactive sputtering with the rf substrate biasing method and its effect on the sputtered VO_2 films on Al_2O_3 (001) substrates were introduced. This method was observed to succeed in enabling control of the ion irradiation energy during sputtering. By varying the substrate biasing power at 0, 10, 20, 30, and 40 W, $-V_{dc}$ with values of 0, 110, 170, 200, and 270 V is introduced at the substrate. As results, increasing of the ion irradiation energy to 30, 140, 200, 230, and 300 eV were achieved, correspondingly. VO_2 grains size decreased with the increasing substrate biasing power. Also, as the results of increasing the ion irradiation energy during sputtering, the film thickness significantly decreases with the increasing of substrate biasing power, suggesting the decreasing and increasing of the deposition rate and sputter rate, respectively.

By introducing rf substrate biasing, high energy ion irradiation during deposition was achieved and results in the modifications of the transition temperature (T_{IMT}). T_{IMT} was observed to once increased to the higher side, then turned to shift towards lower side, recording lowest T_{IMT} of 36ºC at the high biasing power of 40 W. SPT's transition temperature (T_{SPT}) was determined and observed to have a similar modifications pattern with the T_{IMT}, thus evidenced the lowering of the transition temperature (T_t) in the sputtered VO_2 films due to the high-energy ion irradiation. The same T_t modifications pattern was also observed to occur in the IR transmittance properties, which expected to broaden VO_2 for optical applications, such as smart windows. Signifying an extensive decrease of the T_t in the films of 30 and 40 W, the increasing of the TCR values to be at around -3.5 %ºC^{-1} was observed in both films of 30 and 40 W, correspondingly.

In Chapter 3, the mechanism behind the transition temperature (T_t) modifications in films deposited by reactive sputtering with substrate biasing was discussed. In-plane stress state of the sputtered VO_2 films was estimated by considering the shift of the VO_2 $(020)_{M1}$ peak that corresponds to the out-of-plane b_M-axis length. The in-plane stress was of tensile state in the film deposited at ion energy of 140 eV (10W), then turned into the compressive state by increasing the ion energy to a value larger than 200 eV ($\geq$ 20 W). In agreement with the in-plane tensile stress observed in the film of 10 W, rather longer in-plane $a_M/2$ lattice length was observed. Later increasing in substrate biasing power to 20 to 40 W, in-plane $a_M/2$ lattice length was shortened. Film deposited at 40 W (300 eV) revealed to have the shortest $a_M/2$ lattice length, signifying the lowest T_t value observed in this work.

Continuous strikes of the high-energy ions during the deposition are responsible for inducing the in-plane compressive stress that results in the shortening of the in-plane a_M-axis length and the V–V pair distance. This thus led to the decreasing of the T_t in films deposited with a substrate biasing power larger than 20 W ($E_{ion} \geq 200$ eV). Continuous strikes of high-energy ions are also expected to introduce the oxygen defects in films. The introduction of the oxygen vacancies in high-energy irradiated films introduce free electrons near the octahedral sites and give rise to an early metallic-like state that results in rather an early onset of the IMT. Characterization of the strain along c_R ($a_M/2$)-axis *vs*. transition temperature characteristics revealed that the T_t modifications in films deposited by reactive sputtering with substrate biasing were understood to be mainly triggered by the compression of the in-plane $a_M/2$ (c_R)-axis for films deposited with ion energy up to around 230 eV ($\leq$30 W). However, T_t modifications for films deposited with ion energy larger than 230 eV (> 30 W) are resulted by a collaboration of strain compression along the a_M-axis and oxygen vacancies. Also, the substrate biasing method was revealed to be an efficient method to control the T_t, as the T_t modifications in films with a thickness larger than 100 nm were also achieved.

In Chapter 4, details properties of the unusual growth behavior of films deposited at an adequate substrate biasing power with the growth of large crystalline grains in the size of several μm was given. Large crystalline grains of several μm-sized was first observed, where non-epitaxial $(011)_{M1}$ phase orientation is dominating the growth in VO_2 films deposited on Al_2O_3 (001) substrates deposited under adequate substrate biasing of 10 W (in this work). Smooth step and terrace structures, suggesting single crystalline properties of the μm-sized crystalline grains. The existence of high-oxidation phase (V_nO_{2n+1}) results in the increasing of homologous temperature (T_S/T_M) value to around 0.77. Considering this matter, recrystallization occurs due to an effective atomic diffusion, thus introduce the energetically favorable VO_2 $(011)_{M1}$ plane. In

order to keep the thermodynamic equilibrium of the film, shrinkage of the $(020)_{M1}$ occur simultaneously with the continuing growth of the energetically favorable VO_2 $(011)_{M1}$ plane, resulting in the growth of rather large crystalline grains; μm-sized grains. Temperature-dependent micro-Raman measurements were performed to clarify the origin of the M2 phase. Accordingly, in comparison to the nanograins region, where SPT was observed to occur from M1→R phase, the μm-sized grains shows the occurrence of SPT from M1→M2→R phase, respectively.

From the above results, one can realize that the T_t of the VO_2 films on Al_2O_3 (001) substrates was succesfully achieved by utilizing the rf magnetron sputtering with rf substrate biasing. The systematic control of the T_t with large T_t shift is achieved in the present work of substrate bias sputtering, where no changes in the deposition conditions needed are proposed to be advantageous for widening the applicability of the VO_2 films. Also, the growth of the μm-sized crystalline grains of VO_2 films on Al_2O_3 (001) substrates under particular substrate biasing conditions is expected to improve the transition properties and open new vistas of the VO_2 film

5.2 Future Works

This work revealed that the rf substrate biasing method succeeds in modifying the crystal growth properties, thus significantly modifying the T_t in VO_2 films on Al_2O_3 (001) substrates. However, as one can observe, the introduction of the oxygen vacancies in high-energy ion irradiated films whereas significantly broadened transition properties were observed in the film of 40 W. Considering this matter, in order to further improve this transition properties, varying the O_2 flow rate might be needed.

Also, since the substrate biasing succeeded in lowering the T_t near to room temperature while maintaining its transition ratio and hysteresis behavior in the IMT properties, work towards applications of this VO_2 films is needed.

Bibliography

Bibliography

1. Lee, M. J. *et al.*, Two Series Oxide Resistors Applicable to High Speed and High Density Nonvolatile Memory. *Adv. Mater.* **19,** 3919–3923 (2007).
2. Bae, S. H. *et al.*, The Memristive Properties of a Single VO_2 Nanowire with Switching Controlled by Self-Heating. *Adv. Mater.* **25,** 5098–5103 (2013).
3. Seo, G., Kim, B.-J., Kim, H.-T. and Lee, Y. W., Thermally- or optically-biased memristive switching in two-terminal VO_2 devices. *Curr. Appl. Phys.* **14,** 1251–1256 (2014).
4. Han, Y.-H., Kim, K.-T., -Joon Shin, H., Moon, S. and Choi, I.-H., Enhanced Characteristics of an Uncooled Microbolometer using Vanadium–Tungsten Oxide as a Thermometric Material. *Appl. Phys. Lett.* **86,** 254101 (2005).
5. Chen, C., Yi, X., Zhang, J. and Zhao, X., Linear uncooled microbolometer array based on VOx thin films. *Infrared Phys. Technol.* **42,** 87–90 (2001).
6. Han, Y.-H. *et al.*, Fabrication and Characterization of Bolometric Oxide Thin Film Based on Vanadium-Tungsten Alloy. *Sensors Actuators A* **123–124,** 660–664 (2005).
7. Zhou, J. *et al.*, VO_2 Thermochromic Smart Window for Energy Savings and Generation. *Sci. Rep.* **3,** 3029 (2013).
8. Li, S. Y., Niklasson, G. A. and Granqvist, C. G., Thermochromic fenestration with VO_2-based materials: Three challenges and how they can be met. *Thin Solid Films* **520,** 3823–3828 (2012).
9. Driscoll, T., Kim, H.-T., Chae, B.-G., Ventra, M. Di and Basov, D. N., Phase-Transition Driven Memristive System. *Appl. Phys. Lett.* **95,** 43503 (2009).
10. Pellegrino, L. *et al.*, Multistate Memory Devices Based on Free-Standing VO_2/TiO_2 Microstructures Driven by Joule Self-Heating. *Adv. Mater.* **24,** 2929–2934 (2012).
11. Zhang, W. *et al.*, Hole Carriers Doping Effect on the Metal- Insulator Transition of N-Incorporated Vanadium Dioxide Thin Films. *J. Phys. Chem. C* **118,** 12837–12844 (2014).
12. A. Londos, C., N. Sgourou, E. and Chroneos, A., Defect Engineering of the Oxygen-Vacancy Clusters Formation in Electron Irradiated Silicon by Isovalent Doping: An Infrared Perspective. *J. Appl. Phys.* **112,** 123517 (2012).
13. Jiang, M., Cao, X., Bao, S., Zhou, H. and Jin, P., Regulation of the Phase Transition Temperature of VO_2 Thin Films Deposited by Reactive Magnetron Sputtering Without Doping. *Thin Solid Films* **562,** 314–318 (2014).
14. Jiazhen, Y., Yue, Z., Wanxia, H. and Mingjin, T., Effect of Mo-W Co-Doping on Semiconductor-Metal Phase Transition Temperature of Vanadium Dioxide Film. *Thin Solid Films* **516,** 8554–8558 (2008).
15. Wu, Z. P. *et al.*, Molybdenum Substitutional Doping and Its Effects on Phase Transition Properties in Single Crystalline Vanadium Dioxide Thin Film. *J. Appl. Phys.* **86,** 5311 (1999).

16. Muraoka, Y. and Hiroi, Z., Metal-Insulator Transition of VO_2 Thin Films Grown on TiO_2(001) and (110) substrates. *Appl. Phys. Lett.* **80,** 583 (2002).
17. Nagashima, K., Yanagida, T., Tanaka, H. and Kawai, T., Stress Relaxation Effect on Transport Properties of Strained Vanadium Dioxide Epitaxial Thin Films. *Phys. Rev. B* **74,** 172106 (2006).
18. Nishikawa, M., Nakajima, T., Kumagai, T., Okutani, T. and Tsuchiya, T., Adjustment of Thermal Hysteresis in Epitaxial VO_2 Films by Doping Metal Ions. *J. Ceram. Soc. Japan* **119,** 577–580 (2011).
19. Kakiuchida, H., Jin, P., Nakao, S. and Tazawa, M., Optical Properties of Vanadium Dioxide Film during Semiconductive–Metallic Phase Transition. *Jpn. J. Appl. Phys.* **46,** L113–L116 (2007).
20. Kosuge, K., The Phase Diagram and Phase Transition of the V_2O_3−V_2O_5 System. *J. Phys. Chem. Solids* **28,** 1613–1621 (1967).
21. Müller, C. *et al.*, Early Stages of the Metal-to-insulator Transition of a Thin V_2O_3 Film. *J. Appl. Phys.* **103,** 063705 (2008).
22. Yun, S. J., Lim, J. W., Noh, J. S., Kim, B. J. and Kim, H. T., Vanadium Dioxide and Vanadium Sesquioxide Thin Films Fabricated on (0001) or (1010) Al_2O_3 by Reactive RF-Magnetron Sputter Deposition and Subsequent Annealing Processes. *Jpn. J. Appl. Phys.* **48,** 04C139 (2009).
23. Shin, S. *et al.*, Vacuum-Ultraviolet Reflectance and Photoemission Study of the Metal-Insulator Phase Transitions in VO_2, V_6O_{13}, and V_2O_3. *Phys. Rev. B* **41,** 4993–5009 (1990).
24. Beke, S., A Review of the Growth of V_2O_5 Films from 1885 to 2010. *Thin Solid Films* **519,** 1761–1771 (2011).
25. Kusano, E. and Theil, J. A., Effects of Microstructure and Nonstoichiometry on Electrical Properties of Vanadium Dioxide Films. *J. Vac. Sci. Technol. A Vacuum, Surfaces, Film.* **7,** 1314 (1989).
26. Makarevich, A. M. *et al.*, Chemical Synthesis of High Quality Epitaxial Vanadium Dioxide Films with Sharp Electrical and Optical Switch Properties. *J. Mater. Chem. C* **3,** 9197–9205 (2015).
27. Silversmit, G., Depla, D., Poelman, H., Marin, G. B. and Gryse, R. De., Determination of the V2p XPS Binding Energies for Different Vanadium Oxidation States (V^{5+} to V^{0+}). *J. Electron Spectros. Relat. Phenomena* **135,** 167–175 (2004).
28. Fan, S., Fan, L., Li, Q., Liu, J. and Ye, B., The Identification of Defect Structures for Oxygen Pressure Dependent VO_2 Crystal Films. *Appl. Surf. Sci.* **321,** 464–468 (2014).
29. Luo, Z. *et al.*, Comparison of the Optical Responses of O-poor and O-rich Thermochromic VO_X Films During Semiconductor-to-metal Transition. *J. Phys. Chem. Solids* **73,** 1122–1126 (2012).
30. Wang, Y. L. *et al.*, Phase Composition and Valence of Pulsed Laser Deposited Vanadium Oxide Thin Films at Different Oxygen Pressures. *Surf. Coatings Technol.* **201,** 5344–5347 (2007).
31. Andersson, G., Studies on Vanadium Oxides II. The Crystal Structure of Vanadium Dioxide. *Acta Chem. Scand.* **10,** 623–628 (1956).

32. M. Longo, J. and Kierkegaard, P. A., Refinement of the Structure of VO_2. *Acta Chem. Scand.* **24,** 420–426 (1970).

33. Marezio, M., McWhan, D. B., Remeika, J. P. and Dernier, P. D., Structural Aspects of the Metal-Insulator Transitions in Cr-Doped VO_2. *Phys. Rev. B* **5,** 2541–2551 (1972).

34. Guo, H. *et al.*, Mechanics and Dynamics of the Strain-Induced M1-M2 Structural Phase Transition in Individual VO_2 Nanowires. *Nano Lett.* **11,** 3207–3213 (2011).

35. Rúa, A. *et al.*, Phase Transition Behavior in Microcantilevers Coated with M1-phase VO_2 and M2-phase VO_2:Cr Thin Films. *J. Appl. Phys.* **111,** 104502 (2012).

36. Strelcov, E. *et al.*, Doping-Based Stabilization of the M2 phase in Free-Standing VO_2 Nanostructures at Room Temperature. *Nano Lett.* **12,** 6198–6205 (2012).

37. Okimura, K., Watanabe, T. and Sakai, J., Stress-Induced VO_2 Films with M2 Monoclinic Phase Stable at Room Temperature Grown by Inductively Coupled Plasma-Assisted Reactive Sputtering. *J. Appl. Phys.* **111,** 73514 (2012).

38. Zhang, S., Li, Y., Wu, C., Zheng, F. and Xie, Y., Novel Flowerlike Metastable Vanadium Dioxide (B) Micronanostructures: Facile Synthesis and Application in Aqueous Lithium Ion Batteries. *J. Phys. Chem. C* **113,** 15058–15067 (2009).

39. Liu, H., Wang, Y., Wang, K., Hosono, E. and Zhou, H., Design and Synthesis of a Novel Nanothorn VO_2(B) Hollow Microsphere and Their Application in Lithium-ion Batteries. *J. Mater. Chem.* **19,** 2835 (2009).

40. Oka, Y., Ohtani, T., Yamamoto, N. and Takada, T., Phase Transition and Electrical Properties of VO_2 (A). *J. Ceram. Soc. Jpn* **97,** 1134–1137 (1989).

41. Popuri, S. R. *et al.*, VO_2 (A): Reinvestigation of Crystal Structure, Phase Transition and Crystal Growth Mechanisms. *J. Solid State Chem.* **213,** 79–86 (2014).

42. Goodenough, J. B., The Two Components of the Crystallographic Transition in VO_2. *J. Solid State Chem.* **3,** 490–500 (1971).

43. Zylbersztejn, A. and F. Mott, N., Metal-Insulator Transition in Vanadium Dioxide. *Phys. Rev. B* **11,** 4383–4395 (1975).

44. Sommers, C. and Doniach, S., First Principles Calculation of the Intra-Atomic Correlation Energy in VO_2. *Solid State Commun.* **28,** 133–135 (1978).

45. Rice, T. M., Launois, H. and Pouget, J. P., Comment on 'VO_2: Peierls or Mott-Hubbard A View from Band Theory'. *Phys. Rev. Lett.* **73,** 3042 (1994).

46. Eyert, V., The Metal-Insulator Transitions of VO_2: A Band Theoretical Approach. *Ann. der Phys.* **11,** 650–7024 (2002).

47. Biermann, S., Poteryaev, A., Lichtenstein, A. I. and Georges, A., Dynamical Singlets and Correlation-Assisted Peierls Transition in VO_2. *Phys. Rev. Lett.* **94,** 26404 (2005).

48. Tak Kim, H. *et al.*, Mechanism and Observation of Mott Transition in VO_2-based Two- and Three-Terminal Devices. *New J. Phys.* **6,** 52 (2004).

49. Chen, S., Liu, J., Luo, H. and Gao, Y., Calculation Evidence of Staged Mott and Peierls Transitions in VO_2 Revealed by Mapping Reduced-Dimension Potential Energy Surface. *J. Phys. Chem. Lett.* **6,** 3650–3656 (2015).

50. J. Morin, F., Oxides Which Show a Metal-to-Insulator Transition at the Neel Temperature. *Phys. Rev. Lett.* **3,** 34–36 (1959).

51. Verleur, H. W., Barker, A. S. and Berglund, C. N., Optical properties of VO_2 between 0.25 and 5 eV. *Phys. Rev.* **172,** 788–798 (1968).

52. Paone, A. *et al.*, Influence of Doping in Thermochromic $V_{1-x}W_xO_2$ and $V_{1-x}Al_xO_2$ Thin Films: Twice Improved Doping Efficiency in $V_{1-x}W_xO_2$. *J. Alloys Compd.* **621,** 206–211 (2015).

53. Chae, B. G., Kim, H. T. and Yun, S. J., Characteristics of W- and Ti-Doped VO_2 Thin Films Prepared by Sol-Gel Method. *Electrochem. Solid-State Lett.* **11,** D53–D55 (2008).

54. Sahana, M. B., Dharmaprakash, M. S. and Shivashankar, S. A., Microstructure and Properties of VO_2 Thin Films Deposited by MOCVD from Vanadyl Acetylacetonate. *Journal of Materials Chemistry* **12,** 333–338 (2002).

55. Zhang, H., Chang, H. L. M., Guo, J. and Zhang, T. J., Microstructure of Epitaxial VO_2 Thin Films Deposited on (1120) Sapphire by MOCVD. *J. Mater. Res.* **9,** 2264–2271 (1994).

56. Takahashi, Y. and Kanamori, M., Preparation of VO_2 Films by Organometallic Chemical Vapour Deposition and Dip-Coating. *J. Mater. Chem.* **24,** 2481–2486 (1989).

57. Sakai, J. *et al.*, Pulsed Laser-Deposited VO_2 Thin Films on Pt Layers. *J. Appl. Phys.* **113,** 123503 (2013).

58. Lysenko, S. *et al.*, Light-Induced Ultrafast Phase Transitions in VO_2 Thin Film. *Appl. Surf. Sci.* **252,** 5512–5515 (2006).

59. Li, J. and Dho, J., Characteristics of Phase Transition of VO_2 Films Grown on TiO_2 Substrates with Different Crystal Orientations. *J. Cryst. Growth* **404,** 84–88 (2014).

60. A. Rozgonyi, G. and H. Hensler, D., Structural and Electrical Properties of Vanadium Dioxide Thin Films. *J. Vac. Sci. Technol.* **5,** 194 (1968).

61. N. Fuls, E., H. Hensler, D. and R. Ross, A., Reactively Sputtered Vanadium Dioxide Thin Films. *Appl. Phys. Lett.* **10,** 199–201 (1967).

62. Kusano, E., Theil, J. A. and Thornton, J. A., Deposition of Vanadium Oxide Films by Direct-Current Magnetron Reactive Sputtering. *J. Vac. Sci. Technol. A* **6,** 1663 (1988).

63. Razavi, A., Hughes, T., Antinovitch, J. and Hoffman, J., Temperature Effects on Structure and Optical Properties of Radio-Frequency Sputtered VO_2. *J. Vac. Sci. Technol. A Vacuum, Surfaces, Film.* **7,** 1310–1313 (1989).

64. Shigesato, Y., Enomoto, M. and Odaka, H., Thermochromic VO_2 Films Deposited by RF Magnetron Sputtering Using V_2O_3 or V_2O_5 Targets. *Jpn. J. Appl. Phys.* **39,** 6016–6024 (2000).

65. Ruzmetov, D., Zawilski, K. T., Narayanamurti, V. and Ramanathan, S., Structure-Functional Property Relationships in Rf-Sputtered Vanadium Dioxide Thin Films. *J. Appl. Phys.* **102,** 113715 (2007).

66. Sakai, J., Zaghrioui, M., Matsushima, M., Funakubo, H. and Okimura, K., Impact of Thermal Expansion of Substrates on Phase Transition Temperature of VO_2 Films. *J. Appl. Phys.* **116,** 123510 (2014).

67. Okimura, K. and Sakai, J., Changes in Lattice Parameters of VO_2 Films Grown on c-Plane Al_2O_3 Substrates Across Metal-Insulator Transition. *Jpn. J. Appl. Phys.* **48,** 45504 (2009).

68. Fan, L. L. *et al.*, Strain Dynamics of Ultrathin VO_2 Film Grown on TiO_2 (001) and the Associated Phase Transition Modulation. *Nano Lett.* **14,** 4036–4043 (2014).

69. Shibuya, K., Tsutsumi, J., Hasegawa, T. and Sawa, A., Fabrication and Raman Scattering Study of Epitaxial VO_2 Films on MgF_2 (001) Substrates. *Appl. Phys. Lett.* **103,** 21604 (2013).

70. Miyazaki, K., Shibuya, K., Suzuki, M., Wado, H. and Sawa, A., Correlation Between Thermal Hysteresis Width and Broadening of Metal-Insulator Transition in Cr- and Nb-doped VO_2 Films. *J. Appl. Phys.* **53,** 71102 (2014).

71. Kosuge, K., The Phase Transition in VO_2. *Journal of the Physical Society of Japan* **22,** 551–557 (1967).

72. Du, J. *et al.*, Significant Changes in Phase-Transition Hysteresis for Ti-doped VO_2 Films Prepared by Polymer-Assisted Deposition. *Sol. Energy Mater. Sol. Cells* **95,** 469–475 (2011).

73. Chen, S., Liu, J., Wang, L., Luo, H., and Gao, Y., Unraveling Mechanism on Reducing Thermal Hysteresis Width of VO_2 by Ti Doping: A Joint Experimental and Theoretical Study. *J. Phys. Chem. C* **118,** 18938–18944 (2014).

74. Piccirillo, C., Binions, R. and P. Parkin, I., Nb-doped VO_2 Thin Films Prepared by Aerosol-Assisted Chemical Vapour Deposition. *Eur. J. Inorg. Chem.* **2007,** 4050–4055 (2007).

75. Xu, S. Q., Ma, H. P., Dai, S. X., and Jiang, Z. H., Study on Optical and Electrical Switching Properties and Phase Transition Mechanism of Mo^{6+}-doped Vanadium Dioxide Thin Films. *J. Mater. Sci.* **39,** 489–493 (2004).

76. Takami, H., Kawatani, K., Kanki, T., and Tanaka, H., High Temperature-Coefficient of Resistance at Room Temperature in W-Doped VO_2 Thin Films on Al_2O_3 Substrate and Their Thickness Dependence. *Jpn. J. Appl. Phys.* **50,** 55804 (2011).

77. Karaoglan-Bebek, G., Hoque, M. N. F., Holtz, M., Fan, Z., and Bernussi, A. A., Continuous Tuning of W-doped VO_2 Optical Properties for Terahertz Analog Applications. *Appl. Phys. Lett.* **105,** 201902 (2014).

78. Si, C. *et al.*, Metal–Insulator Transition in $V_{1-x}W_xO_2$: Structural and Electronic Origin. *Phys. Chem. Chem. Phys.* **14,** 15021 (2012).

79. Shibuya, K., Kawasaki, M. and Tokura, Y., Metal-Insulator Transition in Epitaxial $V_{1-x}W_xO_2$ ($0 \leq x \leq 0.33$) Thin Films. *Appl. Phys. Lett.* **96,** 22102 (2010).

80. Futaki, H. and Aoki, M., Effects of Various Doping Elements on the Transition Temperature of Vanadium Oxide Semiconductors. *Jpn. J. Appl. Phys.* **8,** 1008–1013 (1969).

81. Jorgenson, G. V. and Lee, J. C., Doped Vanadium Oxide for Optical Switching Films. *Sol. Energy Mater.* **14,** 205–214 (1986).

82. Ino, K., Toshikuni, S., Takeo, U., and Tadahiro, O., Ion Energy, Ion Flux, and Ion Species Effects on Crystallographic and Electrical Properties of Sputter-Deposited Ta Thin Films. *J. Vac. Sci. Technol. A* **15,** 2627 (1997).

83. Cuomo, J. J., Modification of Niobium Film Stress by Low-Energy Ion Bombardment during Deposition. *J. Vac. Sci. Technol.* **20,** 349 (1982).

84. Mian, M. S. and Okimura, K., Effects of Energetic Substrate-Incident Ions on the Growth of Crystalline Vanadium Dioxide Films in Inductively Coupled Plasma-Assisted Sputtering. *Jpn. J. Appl. Phys.* **53,** 35802 (2014).

85. Mian, M. S., Okimura, K., and Sakai, J., Self-Oscillation Up to 9 MHz Based on Voltage Triggered Switching in VO_2/TiN Point Contact Junctions. *J. Appl. Phys.* **117,** 215305 (2015).

86. Petrov, I., Hultman, L., Sundgren, J.-E., and Greene, J. E., Polycrystalline TiN Films Deposited by Reactive Bias Magnetron Sputtering: Effects of Ion Bombardment on Resputtering Rates, Film Composition, and Microstructure. *J. Vac. Sci. Technol. A* **10,** 265 (1992).

87. Bensaoula, A., Wolfe, J. C., Ignatiev, A., Fong, F.-O., and Leung, T.-S., Direct-Current-Magnetron Deposition of Molybdenum and Tungsten with Rf-Substrate Bias. *J. Vac. Sci. Technol. A Vacuum, Surfaces, Film.* **2,** 389 (1984).

88. Edelberg, E. A., Perry, A., Benjamin, N., and Aydil, E. S., Energy Distribution of Ions Bombarding Biased Electrodes in High Density Plasma Reactors. *J. Vac. Sci. Technol. A* **17,** 506 (1999).

89. Profijt, H. B., van de Sanden, M. C. M., and Kessels, W. M. M., Substrate-Biasing during Plasma-assisted Atomic Layer Deposition to Tailor Metal-Oxide Thin Film Growth. *J. Vac. Sci. Technol. A* **31,** 01A106 (2013).

90. Okimura, K., Sasakawa, Y., and Nihei, Y., X-ray Diffraction Study of Electric Field-Induced Metal–Insulator Transition of Vanadium Dioxide Film on Sapphire Substrate. *Jpn. J. Appl. Phys.* **45,** 9200–9202 (2006).

91. Anders, A., A Structure Zone Diagram including Plasma-based Deposition and Ion Etching. *Thin Solid Films* **518,** 4087–4090 (2010).

92. Azhan, N. H., Su, K., Okimura, K., and Sakai, J., Radio frequency substrate biasing effects on the insulator-metal transition behavior of reactively sputtered VO_2 films on sapphire (001). *J. Appl. Phys.* **117,** 185307 (2015).
93. Schilbe, P., Raman scattering in VO_2. in *Physica B* **316–317,** 600–602 (2002).
94. Chou, J. Y., Lensch-Falk, J. L., Hemesath, E. R. and Lauhon, L. J., Vanadium Oxide Nanowire Phase and Orientation Analyzed by Raman Spectroscopy. *J. Appl. Phys.* **105,** 34310 (2009).
95. Wu, C., Feng, F. and Xie, Y., Design of vanadium oxide structures with controllable electrical properties for energy applications. *Chem. Soc. Rev.* **42,** 5157–83 (2013).
96. Azhan, N. H., Okimura, K., Ohtsubo, Y., Kimura, S., Zaghrioui, M., and Sakai, J., Large modification in insulator-metal transition of VO_2 films grown on Al_2O_3 (001) by high energy ion irradiation in biased reactive sputtering. *J. Appl. Phys.* **119,** 55308 (2016).
97. Rajendra Kumar, R. T. *et al.*, Pulsed Laser Deposited Vanadium Oxide Thin Films for Uncooled Infrared Detectors. *Sensors Actuators A* **107,** 62–67 (2003).
98. Wang, Y. L., Li, M. C. and Zhao, L. C., Phase Transformation and R–T Characteristics of Vacuum Annealed Vanadium Oxide Thin Films. *Surf. Rev. Lett.* **15,** 59–64 (2008).
99. Koch, R., Stress in Evaporated and Sputtered Thin Films - A Comparison. *Surf. Coatings Technol.* **204,** 1973–1982 (2010).
100. Case, F. C., Modifications in the Phase Transition Properties of Predeposited VO_2 Films. *J. Vac. Sci. Technol. A Vacuum, Surfaces, Film.* **2,** 1509 (1984).
101. Tsai, K.-Y., Chin, T.-S. and Shieh, H.-P. D., Effect of Grain Curvature on Nano-Indentation Measurements of Thin Films. *Jpn. J. Appl. Phys.* **43,** 6268–6273 (2004).
102. Jin, P. *et al.*, Characterization of Mechanical Properties of VO_2 Thin Films on Sapphire and Silicon by Ultra-Microindentation. *Thin Solid Films* **343–344,** 134–137 (1999).
103. Boulle, A. *et al.*, Role of Thermal Strain in the Metal-Insulator and Structural Phase Transition of Epitaxial VO_2 Films. *Phys. Rev. B* **93,** 184106 (2016).
104. Kittiwatanakul, S., Wolf, S. A. and Lu, J., Large Epitaxial Bi-axial Strain Induces a Mott-like Phase Transition in VO_2. *Appl. Phys. Lett.* **105,** 2012–2017 (2014).
105. Cui, Y. and Ramanathan, S., Substrate Effects on Metal-Insulator Transition Characteristics of Rf-Sputtered Epitaxial VO_2 Thin Films. *J. Vac. Sci. Technol. A* **29,** 41502–41507 (2011).
106. Hoffman, D. W. and Thornton, J. A., Compressive Stress and Inert Gas in Mo Films Sputtered from a Cylindrical-Post Magnetron with Ne, Ar, Kr, and Xe. *J. Vac. Sci. Technol.* **17,** 380 (1980).
107. Yuan, X., Zhang, W. and Zhang, P., Hole-lattice Coupling and Photoinduced Insulator-Metal Transition in VO_2. *Phys. Rev. B* **88,** 35119 (2013).
108. Zaghrioui, M., Sakai, J., Azhan, N. H., Su, K. and Okimura, K., Polarized Raman Scattering of Large Crystalline Domains in VO_2 Films on Sapphire. *Vib. Spectrosc.* **80,** 79–85 (2015).

109. Chen, C. *et al.*, Influence of Defects on Structural and Electrical Properties of VO_2 Thin Films. *J. Appl. Phys.* **110,** 23707 (2011).

110. Guinneton, F., Sauques, L., Valmalette, J.-C., Cros, F. and Gavarri, J.-R., Role of Surface Defects and Microstructure in Infrared Optical Properties of Thermochromic VO_2 Materials. *J. Phys. Chem. Solids* **66,** 63–73 (2005).

111. Sawatzky, G. A. and Post, D., X-ray Photoelectron and Auger Spectroscopy Study of Some Vanadium Oxides. *Phys. Rev. B* **20,** 1546 (1979).

112. Kurmaev, E. Z. *et al.*, Electronic Structure of VO_2 Studied by X-ray Photoelectron and X-ray Emission Spectroscopies. *J. Phys. Condens. Matter* **10,** 18 (1998).

113. Blaauw, C., Leenhouts, F., Woude, F. van der and Sawatzky, G. A., The Metal-non-metal Transition in VO_2 : X-ray Photoemission and Resistivity Measurements. *J. Phys. C Solid State Phys.* **8,** 459–468 (1975).

114. Hush, N. S., Inequivalent XPS binding Energies in Symmetrical Delocalized Mixed-valence Complexes. *Chem. Phys.* **10,** 361–366 (1975).

115. Rosevear, W. H. and Paul, W., Hall Effect in VO_2 Near the Semiconductor-to-Metal Transition. *Phys. Rev. B* **7,** 2109–2111 (1973).

116. Ruzmetov, D., Heiman, D., Claflin, B. B., Narayanamurti, V. and Ramanathan, S., Hall Carrier Density and Magnetoresistance Measurements in Thin-Film Vanadium Dioxide Across the Metal-Insulator Transition. *Phys. Rev. B - Condens. Matter Mater. Phys.* **79,** 10–13 (2009).

117. Azhan, N. H., Su, K., Okimura, K., Zaghrioui, M. and Sakai, J., Appearance of large crystalline domains in VO_2 films grown on sapphire (001) and their phase transition characteristics. *J. Appl. Phys.* **117,** 245314 (2015).

118. Humphreys, F. J. and Hatherly, M., *Recrystallization and Related Annealing Phenomena*. *Pergamon* **2,** (2015).

119. Koch, R., The Intrinsic Stress of Polycrystalline and Epitaxial Thin Metal Films. *J. Phys. Condens. Matter* **6,** 9519–9550 (1994).

120. Gupta, V. and Mansingh, A., Influence of Postdeposition Annealing on the Structural and Optical Properties of Sputtered Zinc Oxide Film. *J. Appl. Phys.* **80,** 1063 (1996).

121. Okimura, K., Azhan, N. H., Hajiri, T., Kimura, S., Zaghrioui, M. and Sakai, J., Temperature-dependent Raman and Ultraviolet Photoelectron Spectroscopy Studies on Phase Transition Behavior of VO_2 films with M1 and M2 Phases. *J. Appl. Phys.* **115,** 153501 (2014).

Achievements

Achievements

A. Peer-reviewed Journals

1. Kui Su, Takuya Naka, Nurul Hanis Azhan, Kunio Okimura, and Masashi Higuchi, "Oriented Growth of VO_2 (B) Thin Films on Mo Foils by Reactive Sputtering for Lithium Ion Batteries", Thin Solid Films **616**, 95-100 (2016).

2. Nurul Hanis Azhan, Kunio Okimura, Yoshiyuki Ohtsubo, Shin-ichi Kimura, Mustapha Zaghrioui, and Joe Sakai, "Large modification in insulator-metal transition of VO_2 films grown on Al_2O_3 (001) by high energy ion irradiation in biased reactive sputtering", J. Appl. Phys. **119**, 055308 (2016).

3. Mustapha Zaghrioui, Joe Sakai, Nurul Hanis Azhan, Kui Su, and Kunio Okimura, "Polarized Raman scattering of Large crystalline domains in VO2 films on sapphire", Vibrational Spectroscopy 80, 79-85 (2015).

4. Nurul Hanis Azhan, Ku Sui, Kunio Okimura, Mustapha Zaghrioui, and Joe Sakai, Appearance of large crystalline domains in VO_2 films grown on sapphire (001) and their phase transition characteristics", J. Appl. Phys. **117**, 245314 (2015).

5. Nurul Hanis Azhan, Ku Sui, Kunio Okimura, and Joe Sakai, "Radio frequency substrate biasing effects on the insulator-metal transition behavior of reactively sputtered VO_2 films on sapphire (001)", J. Appl. Phys. **117**, 185307 (2015).

6. Kunio Okimura, Nurul Hanis Azhan, Tetsuya Hajiri, Shin-ichi Kimura, Mustapha Zaghrioui, and Joe Sakai, "Temperature-dependent Raman and UPS studies on phase transition behavior of VO_2 films with M1 and M2 phases", J. Appl. Phys, **115**, (2014) 153501.

B. Proceedings

1. Nurul Hanis Azhan, Kui Su, Kunio Okimura, Mustapha Zaghrioui, and Joe Sakai, "Appearance of large crystalline domains in VO_2 films on Al_2O_3 (001) substrates by rf biased sputtering and its effect on the phase transition properties", 13th International Symposium on Sputtering & Plasma Process, Kyoto, Japan, July 2015.

2. Ku Sui, Nurul Hanis Azhan, and Kunio Okimura, "Oriented growth of VO_2(B) thin films on Mo foil by reactive sputtering for lithium ion batteries", 13th International Symposium on Sputtering & Plasma Process, Kyoto, Japan, July 2015.

3. Nurul Hanis Azhan and Kunio Okimura, "Electrical Properties of VO_2 and Post-Annealing Effect on the Growth of Non-Stoichiometric VO_X Thin Films on Silicon Substrates with Metal-Insulator Transition", MJIT-JUC Joint Symposium MJJIS2013, Tokai University, Japan, November 2013.

4. Nurul Hanis Azhan and Kunio Okimura, "Electrical Properties of Post-Annealed VO_2 Thin Films on Silicon Substrates with Metal-Insulator Transition", 12th International Symposium on Sputtering & Plasma Process, Kyoto, Japan, July 2013.

5. Nurul Hanis Azhan, Md. Suruz Mian and Kunio Okimura, "Electrical Properties of Vanadium Dioxide Thin Films on Silicon Substrate with Metal-Insulator Transition", MJIT-JUC Joint Symposium, Kuala Lumpur, Malaysia, November 2012.

C. International Conferences

1. Nurul Hanis Azhan, Kunio Okimura, Mustapha Zaghrioui, and Joe Sakai, "Characteristic μm-sized VO_2 domains grown on Al_2O_3 (001) deposited under particular substrate biasing conditions", The 18th International Conference on Crystal Growth and Epitaxy (ICCGE18), Nagoya, Japan, August 2016.

2. Nurul Hanis Azhan, Kunio Okimura, Mustapha Zaghrioui, and Joe Sakai, "Crystalline growth and transition characteristics of sputtered VO_2 on Al_2O_3 (001) substrates via rf substrate biasing", 14th International Union of Materials Research Societies – International Conference on Advanced Materials, Jeju, Korea, October 2015.

3. Kunio Okimura, Nurul Hanis Azhan, Kui Su, and Joe Sakai, "Effects of rf substrate biasing on insulator-metal transition properties of oriented VO_2 films on Al_2O_3 (001) in reactive sputtering", 14th International Union of Materials Research Societies – International Conference on Advanced Materials, Jeju, Korea, October 2015.

4. Ku Sui, Nurul Hanis Azhan**,** and Kunio Okimura, "Selective Growth of VO_2 (B) and VO_2 (M) Films in Reactive Magnetron Sputtering with Substrate Biasing", 14th International Union of Materials Research Societies – International Conference on Advanced Materials, Jeju, Korea, October 2015.

5. Nurul Hanis Azhan**,** Kui Su, Kunio Okimura, Mustapha Zaghrioui, and Joe Sakai, "Appearance of large crystalline domains in VO_2 films on Al_2O_3 (001) substrates by rf biased sputtering and its effect on the phase transition properties", 13th International Symposium on Sputtering & Plasma Process, Kyoto, Japan, July 2015.

6. Ku Sui, Nurul Hanis Azhan**,** and Kunio Okimura, "Oriented growth of VO_2(B) thin films on Mo foil by reactive sputtering for lithium ion batteries", 13th International Symposium on Sputtering & Plasma Process, Kyoto, Japan, July 2015.

7. Nurul Hanis Azhan**,** Kui Su, Kunio Okimura, "Controlling the Insulator-Metal Transition Temperature of Stoichiometric VO_2 Films on Sapphire by RF Biased Reactive Sputtering", 1st E-MRS/MRS-J Joint Symposium, Yokohama, Japan, December, 2014.

8. Nurul Hanis Azhan and Kunio Okimura, "The Orientation Growth and the Electrical Properties of VO_2 Thin Films on Si (100) Substrate via Post-Annealing", International Union of Materials Research Societies-International Conference on Electronic Materials (IUMRS-ICEM 2014), Taiwan, June 2014.

D. Awards

1. **Best Poster Award First Place**

   "Crystalline growth and transition characteristics of sputtered VO_2 on Al_2O_3 (001) substrates via rf substrate biasing", 14th International Union of Materials Research Societies – International Conference on Advanced Materials, Jeju, Korea, October 2015.

Acknowledgements

In the name of Allah S.W.T, the Most Gracious and Merciful.

First and foremost, deepest appreciation and sincere gratitude go to my supervisor Prof. Dr. Eng. Kunio Okimura for the continuous supports, and for his patience, motivation, enthusiasm, and immense knowledge towards the completion of my doctoral course. I have been extremely lucky to have a supervisor who cared so much about my work, and who responded to my questions and queries so promptly.

Special appreciations to the members of the committee, Prof. Dr. Yoshihito Matsumura, Prof. Dr. Kiyoteru Kobayashi, Prof. Dr. Masaki Asobe, and Prof. Dr. Satoru Iwamori, for serving as my committee members even at hardship. I also want to thank you for letting my defense be an enjoyable moment, and for your brilliant comments and suggestions, thanks to you.

My special thanks to the member of Okimura Laboratory, Department of Electrical and Electronic Engineering, Tokai University; and to the department as a whole, the year of 2012 to 2016, for their valuable encouragement and continuous supports. Completing this work would have been all the more difficult were it not for their support and friendship provided.

Towards completing this doctoral course, writing a peer-reviewed journal is a must. My warm thanks to fellow co-researchers and papers' co-authors involved in this work. Without their cooperation, publishing those journals are something that could not be done. Their suggestive comments and those valuable thoughts mean a lot.

In my attempted measurements, I thank the following people for their corporations:
Raman measurement
Dr. Mustapha Zaghrioui and Dr. Joe Sakai from GREMAN, University of Tours
UPS measurement
Prof. Shin-ichi Kimura and Dr. Yoshiyuki Ohtsubo from Graduate School of Frontier Biosciences, Osaka University.
FE-SEM, AFM and EPMA measurements
Staffs of the Future Scientific Technology Joint Research Center, Tokai University.
They were always there for a helpful discussion, and their never-ending inspiration has helped me and my research in various ways. I am indebted to them for their help.

Not to forget, biggest thanks to University of Kuala Lumpur (UniKL) and Majlis Amanah Rakyat (MARA) for the opportunity for to further my study in Tokai University in order to gain more knowledge and experience that will soon be used in my career.

Last but not least, my deepest gratitude goes to my beloved parents and also to my friends for their endless love, prayers, and encouragement. Well, this work may not have been completed without their thoughtful prayers and blessings. Thank you very much.

For every one of you who directly and indirectly contributed to this work, I can only pray that God will bestow upon you a blessed life.

Dedication

To my parents,
Mr. Azhan Abdul Hamid and Mrs. Noraeshah Ishak

To my one and only younger brother,
Fakhrul Helmie Azhan

This humble work is a sign of my love to you!